Study on new mechanisms for improving performance of two-photon excitation fluorescence microscopy using temporal focusing

October 2018

SONG, QIYUAN

Study on new mechanisms for improving performance of two-photon excitation fluorescence microscopy using temporal focusing	October 2018	SONG, QIYUAN

Keio University

Graduate School of Science and Technology
School of Integrated Design Engineering

Study on new mechanisms for improving performance of two-photon excitation fluorescence microscopy using temporal focusing

by

SONG, QIYUAN

A THESIS SUBMITTED
IN PARTIAL FULFILLMENT OF
THE REQUIREMENTS FOR THE DEGREE
Doctor of Philosophy

APPROVED, THESIS COMMITTEE:

Kannari, Fumihiko

Saiki, Toshiharu

Tanabe, Takasumi

Watanabe, Shinichi

A Thesis for the Degree of Ph.D. in Engineering

Study on new mechanisms for improving performance of two-photon excitation fluorescence microscopy using temporal focusing

October 2018

Graduate School of Science and Technology
Keio University

SONG, QIYUAN

Abstract

Temporal focusing (TF) microscopy is a wide-field optically sectioned multi-photon microscopy. It has the potential to realize three-dimensional (3D) volumetric in-vivo imaging with fast speed and large penetration depth. But TF has two fundamental limitations. The sectioning ability of TF is worse than confocal and two-photon excitation fluorescence (TPEF) microscopy. Meanwhile, the scattered background fluorescence reduces the signal-to-background ratio (SBR) in deep and dense sample imaging. This research aims to solve these problems through two original techniques, two-dimensional (2D) TF and 3D interferometric temporal focusing (ITF) microscopy. In addition, 3D-ITF microscopy can achieve 3D super-resolution function. Also we find that 3D-ITF imaging is robust in distorted optics.

Chapter 1 reviews the wide-field optical microscopy with sectioning ability. Among them, TF microscopy is the best candidate to realize 3D volumetric in-vivo imaging. Then the problems of TF and the objective in this research are described.

Chapter 2 describes the proposal and demonstrate 2D-TF to improve the sectioning ability of TF to be the same as that of a point scanning TPEF microscopy as well as to keep the wide-field feature. The experimental demonstration of the virtually imaged phased array (VIPA) based 2D-TF to verify the theory is described. Then a 2D-TF TPEF microscopy to evaluate the sectioning resolution is built up and the improvement in imaging depth is shown. At last, the fast 3D volumetric imaging in 2D-TF by imaging 3D Brownian motion is achieved.

Chapter 3 describes combination 3D structured illumination microscopy (3D-SIM) and TF, named 3D-ITF microscopy, to both remove background fluorescence and improve spatial resolution and sectioning resolution. A digital micromirror device (DMD) is used to build up 3D-ITF in experiment. The super sectioning resolution and the super-resolution in 3D-ITF microscopy are evaluated, and the ability to remove background fluoresce in 3D-ITF imaging is proved.

Chapter 4 describes the extension of the study described in Chapter 3 to investigate the performance of 3D-ITF imaging in distorted optics. The theoretical study shows that there is redundancy in spatial spectrum domain for 3D-ITF imaging. Through the numerical simulation, it is shown how the redundancy supports the resistance of spatial resolution and sectioning resolution in deep and dense sample imaging where wavefront distortions and background fluoresce exist.

Chapter 5 summarizes the achievements in theoretical and experimental works and gives a prospect such as to combine the works in 2D-TF and 3D-ITF.

Table of Contents

Chapter 1

Introduction

Light as a media for information and carrier of energy becomes indispensable in our life. For example, everyone relies on fiber optics to access internet. With the reduction of the cost of the laser, there is a tendency to increase the use of advanced light technology in daily life. We can see this tendency in optical sensors such as the application in autopilot system. The major merit to utilize optics is to increase the throughput. The throughput in general includes the amount of the information, the quality such as signal to noise ratio (SNR) of the information and the varieties of the information. In this thesis, it is an example of how to invent new optical technology to increase the throughput in a special optical sensor, two photon excitation fluorescence (TPEF) microscopy. The approach in this technology invention is carried out in two aspects. First, we can utilize the physical principles to invent new optical devices. Secondly, we can utilize the algorithm which applies mathematical and engineering method. So, the innovation is an integrated study of physics, mathematics, engineering, chemistry, biology and so on. Through the research and the innovation in this thesis, the technology itself is not limited to TPEF microscopy. These methods could be adjusted and implemented in the general optical sensor field in the information age. For example, the structured illumination microscopy (SIM) technology, which will be introduced in the thesis is not limited to microscopy. The general structured illumination idea is already applied in every one's cell phone camera to capture depth information.

In this chapter, I first give a review on wide-field optical sectioning microscopy in section 1.1. In section 1.2, I review the temporal focusing (TF) technique which realize wide-field TPEF microscopy. In section 1.3, I discuss the limitations in TF and the objectives of the thesis.

1.1 Wide-field optical microscopy with sectioning ability

Optical microscopy has been widely used in nowadays daily life work and research. For example, optical microscopy acts an important role in discovering new findings in biology, especially in brain science research[1] such as the mechanism of Alzheimer disease[2], mental disorder[3] and the fundamental questions like how does memory work and what is intention[4–6]. As the neuron cells are usually dense, the sectioning ability to only select a thin layer of target plane is necessary and important to build up a three-dimensional (3D) volumetric image with acceptable signal-to-background ratio (SBR). The classical wide-field microscopy which is constructed by objective lens, tube lens and array detectors such as charge-coupled device (CCD) or complementary metal–oxide–semiconductor (CMOS) camera do not have sectioning ability. Therefore, huge amount of out-of-focus light forms blurred image as background which make it useless for 3D volumetric image. On the other hand, we also need acceptable temporal resolution to observe dynamic phenomena such as the action potentials of neuron cells via calcium imaging. This requires temporal resolution of volumetric imaging at millisecond level. The third challenge is imaging depth. Brain science research need penetration depth from several ten micrometers to several millimeters in order to observe the neuron actions at different function layers. The scattering of light dramatically limits the imaging depth. In this section, I first review the optical method for sectioning ability. Then I introduce the way to improve the imaging speed for optical sectioned microscopy via parallel detection. At last, I discuss the importance to use longer wavelength of illumination light with multi-photon excitation for deep imaging.

1.1.1 Sectioning ability

Sectioning ability can be vividly understood as the ability to read a page inside a thick book. Suppose the object is a point or a monolayer of points, the wide-field microcopy can build up the 3D view of it with good SBR. However, if we have a lot of points and they distribute in the whole 3D space, the situation is quite different. For the two-dimensional (2D) image at each observing layer, the out-of-focus point object's image which diffracts as large circle

adds together as a background. Since the background is not uniform and varies randomly, we won't be able to discriminate any point at the observing layer although the distance between any points are not beyond diffraction limitation. For this 3D volumetric imaging, we have to have sectioning ability to reduce or remove the out-of-focus images.

Sectioning ability can be mathematically defined by the integrated intensity distribution[7,8], $I(z)$ of point spread function (PSF) at each observing layer as

$$I(z) = \int\int h(x, y, z)dxdy \quad (1.1).$$

Here x and y is the coordinate within the observing layer, z is the axial scanning direction to form 3D image, $h(x, y, z)$ is the PSF of the imaging system. If the imaging system has no sectioning ability, the distribution, $I(z)$ is constant value. Once the imaging system has sectioning ability, the distribution is a peak function. The full-width at half-maximum (FWHM) of the distribution, $I(z)$ is defined as the sectioning resolution. The decay speed of the out-of-focus intensity in the distribution, $I(z)$ is another factor to evaluate the sectioning ability. This can be evaluated mathematically by the slope of the log-log plot of the distribution, $I(z)$ for out-of-focus region. In other words, it is the power, n of the power function z^{-n} for out-of-focus fitting of the distribution, $I(z)$. Ideally, we want the distribution, $I(z)$ as a delta function then there is no out-of-focus intensity spreading into the observing plane. But in reality, there is always out-of-focus intensity remained in the observing plane. Note that the axial resolution of an imaging system means the axial spreading of a point object in its image. Axial resolution is evaluated by the FWHM of PSF in axial direction and it is different to sectioning resolution.

The diffraction limitation of the imaging system could be understood as a 3D low-pass filter then PSF is the impulse response of the imaging system. The 3D low-pass filter is called optical transfer function (OTF) and it is the Fourier Transform of PSF. Physically this low-pass filter origins form the finite size of the objective lens. The finite size of the objective lens only allows limited solid angle of the optical wavevectors pass into it. This effective low pass filter for the optical wavevector is described as pupil function. The autocorrelation of pupil function gives the low pass filter of the imaging system. In 3D space, it is the autocorrelation of a 3D spherical surface of the pupil function to form the 3D OTF.

In the point of view of frequency analysis, the sectioning resolution is determined by the axial spatial bandwidth of planar DC spatial frequency in 3D OTF. The Fourier transform of the distribution, $I(z)$ is

$$FT\{I(z)\} = \iiint h(x,y,z)\exp[i(0\cdot x + 0\cdot y + k_z z)]dxdydz = OTF(k_x = 0, k_y = 0, k_z) \quad (1.2),$$

here k_x, k_y, k_z is the spatial freqeuncy coordinate in *x, y, z* direction respectively. The higher the aixal bandwidth, $OTF(0,0,k_z)$ is, the smaller the FWHM of the sectioing ablity is. In other words, if the axial bandwidth, $OTF(0,0,k_z)$ is 0, it means that there is no sectionig ability. Therefore, we can easily estimate the sectioning ability by evaluating 3D OTF of the imaging system. For wide-field microscopy, 3D OTF looks like a 3D ball with missing cone at the center, which means the axial bandwidth, $OTF(0,0,k_z)$ is 0. So in order to have the sectioning abilty, we need to fill the missing cone in OTF.

Confocal microscopy

The classical sectioning optical microsocpy is confocal microsocpy[9–11]. As Fig. 1.1 shows, Confocal microscopy utilize a pinhole which is conjugate to the observing point as well as the illumination focal point[8]. The pinhole functions as a spatial filter to remove any out-of-focus emission light so that only the central part of the out-of-focus blurred image is recored at a certain observing plane. The size of the pinhole determine how much out-of-focus light is rejected[8]. If the pinhole size is infinite small, then all the out-of-focus image is rejectted. However, if so, the in-focus image will be also attenuated. In imaging practice, we need compromise between the sectioning ablity and the intensity of the image. Mathematically, the PSF of confocal microsocpy is a product of the PSF of illuminaiton light and emission light. For epi-fluorescence microscopy, the exciation wavelenth is close to the emission wavelength thus the PSF can be simplified as a square of the PSF of wide-field microscopy. Therefore in spatial frequency domain, the OTF of confocal microsocpy is the auto-correlation of the OTF of wide-field microscopy. Throung convolution, the missing cone is filled. From this we can prove that there is sectioning ability in confocal microsocpy. With increased pinhole size, we will lose the high spatial freqeuncy in OTF and thus both the spatial resolution and the seicitoning resoltion will reduce.

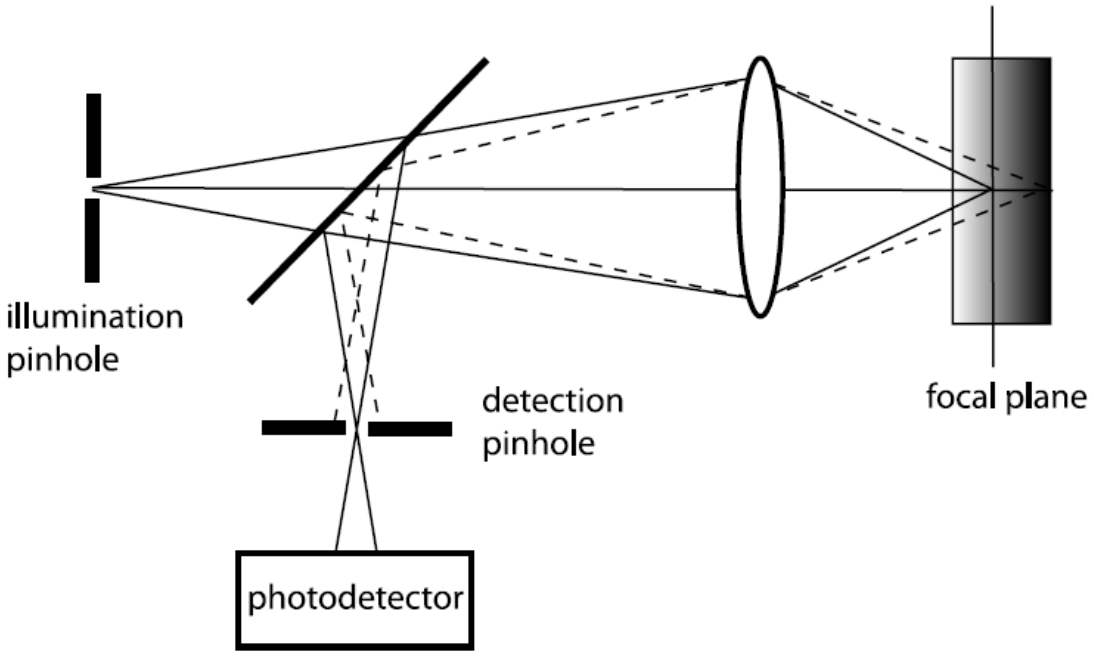

Fig. 1.1 Schematic of confocal microscopy[8]

Two-photon excitation fluorescence (TPEF) microscopy

Another method to have sectioning ability is to utilize nonlinear excitation process[12–15]. Two low energy photons simultanouly excite the object within the solid angle accepted by the objective lens and then high energy photon emits and is collected in TPEF microscopy[15]. Due to the nonlinearity, the PSF of TPEF microsocpy is squared, which has the same mathematical form compared to confocal microsocpy[14]. There are two major difference between confocal microscopy and TPEF microsocpy. First, there is no pinhole in TPEF microscopy so that there is no trade-off between sectioning ability and image intensity. Secondly, TPEF use longer wavelenfth, approximately double the wavelength of emission light. Thus the sectioning resolution of TPEF microsocpy is worse than confocal microsopy as the bandwidth which is inversely propotional to the wavelength in OTF is reduced. However, longer wavelength has less scattering in biological samples and thus the penetration depth in TPEF microscopy is deeper than confocal microsocpy[14,16].

1.1.2 Wide-field optical sectioned microscopy via parallel detection

Although confocal and TPEF microscopy has the sectioning ability, they need a scanner to form a planar image at the observing plane. It takes time to finish the 2D scanning, especially for large field of view and high spatial resolution. A typical resonant scanner operates up to several kHz for single sectioned image scanning and it will take several ten milliseconds to finish a volume scan. Another issue is the repetition rate of the excitation laser. With increased pixels in a volume imaging, the required pulse number also increase. A typical ~100 MHz femtosecond laser need ~1 second to scan a volume image of 1,000 $\times$ 1,000 $\times$ 100 pixels. This is far below the temporal resolution demand to observe neuron actions.

Multifocal microscopy

In order to improve the temporal resolution of volume image, people use parallel detection method. CCD and CMOS camera are the typical parallel detection devices. Photomultiplier array is another example of parallel detection device. For confocal microscopy, instead to scan point by point, people use spinning disk to illuminate and detect multiple points simultaneously and the image is recorded by a parallel detection device. The similar multifocal method is also used in TPEF microscopy[17–25]. The first issue for multifocal microscopy is that there is interference between neighboring focal points out-of-focus[23]. This interference acts similar to Talbot effect which will limit the decay speed of out-of-focus intensity. In order to solve this problem, people set delays between neighboring focal points as time-multiplexing (TMX) method. Another issue is the cross-talk of the scattered emission light[26]. Once the focal points are closer, there is a bigger chance to receive scattered light from neighboring focal points. Thus, to solve this problem we can only use sparse multifocal points which means we still need to scan the focal points in order to get the planar image.

Structured illumination microscopy (SIM)

In order to capture sectioned planar image without scanning, people developed SIM at first time[27–30]. This technique utilize a fringe pattern with three different initial shifts. By setting the phase difference between three patterns equally as $2\pi/3$, we can use homodyne detection to reconstruct the image without any remaining fringe pattern. This method not only achieves sectioning ability for reconstructed image but also remove the static backgrounds. The reconstructed image only selects the modulated image by the spatial modulation frequency of the fringe pattern. Therefore, the distribution, $I(z)$ is effectively the axial behavior of the spatial modulation frequency rather than the planar DC frequency. Since in 3D OTF only at the planar cut-off frequency and DC frequency, their axial distributions are constant, as long as the modulation frequency is not chosen close to the planar cut-off frequency or DC frequency, the reconstructed image will have a good sectioning resolution[28]. The optimized sectioning ability is achieved by a modulation frequency of half the cut-off frequency where it owns the maximum bandwidth in axial direction[28]. On the other hand, in time domain, the shift of the fringe pattern equally gives a temporal modulation at each pixel. By homodyne detection, it effectively chose the signal only at the temporal modulation frequency. Thus, the background which is static is removed in the reconstructed image.

3D-SIM

SIM is extended for super-resolution microscopy later[31–45]. The fundamental difference between the sectioning SIM and super-resolution SIM is that sectioning SIM use variance of the raw images to reconstruct the image which is a nonlinear system in the point of view of signal processing while super-resolution SIM is a linear system which demodulate each sub band image and linearly add them together, although both of them use homodyne detection method to separate the modulated image from DC image[31]. So, with multiple modulation frequencies which is the case of nonlinear SIM, variance image in sectioning SIM can only subtract one image containing all the AC modulations while super-resolution SIM can subtract each sub band image one by one and post-process them separately to enhance the resolution. Super-resolution SIM also combines the idea of standing wave fluorescence microscopy[46] to add modulation in axial direction, which is so called 3D-

SIM[43] (and the super-resolution SIM which use only laterally modulated pattern is so called 2D-SIM.). By this method, the reconstructed image contains sub band with the axial frequency beyond diffraction limitation. Therefore, both the axial resolution and the sectioning resolution is improved two times in 3D-SIM compared to either sectioning SIM or 2D-SIM. However, there is a drawback of SIM, although it can remove the out-of-focus and background signals, the corresponding shot noise remained in reconstructed image. As the illumination light alone in SIM do not support any sectioning ability, SIM will easily fail in deep imaging[47].

Other techniques

Before the development of SIM, there is a popular technique using two opposite objective lenses for coherent emission combination and/or coherent illumination combination to realize wide-field optical sectioning microscopy. The method to use coherent emission combination method is called image interference microscopy or 4Pi microscopy as it is trying to use the whole solid angle of the emission optical wavevectors[48,49]. Although it is not possible to reach 4Pi solid angle, it can increase the solid angle by using two objective lenses. Importantly, the autocorrelation of the 3D pupil function of the two objective lenses solve the problem of missing cone in its 3D OTF, thus it has the sectioning ability. Then people use the illumination interference by two opposite objective lenses via Köhler-illumination mode and combine this with 4Pi microscopy, which is called I^5 microcopy[50,51]. I^5 microscopy can extend the axial frequency support 7 times than wide-field microscopy in its 3D OTF and also fills the missing cone with this amount of frequency support. Although 4Pi microscopy and I^5 microcopy have the sectioning resolution, the need to use two opposite objective lenses to form interference is a big challenging issue in practical imaging. As the sample is thick or dense, it will easily destroy the interference so as to make the microscopy not useful.

In order to overcome this issue, people use two orthogonal posed microscopy instead of two opposite microscopy which is called light-sheet microscopy or plane illumination microscopy[48]. Light-sheet microscopy don't require interference and the sectioning ability is determined by the thickness of the illumination light-sheet. In order to achieve a large

field of view, Light-sheet use small numerical aperture (NA) lens for illumination or use Bessel beam[49]. The objective lens to collect emission light is the same setting as wide-field microscopy. However, the orthogonal setting of two objective lenses physically limits the setup for in-vivo image as limited space and angle is allowed to set the objective lenses.

1.1.3 The advantage to use longer wavelength of excitation

From the diffraction limitation, we know in order to achieve better resolution, we need to use shorter wavelength. However, the scattering, especially Rayleigh scattering increase if we reduce the wavelength. On the other hand, once the wavelength is above 1 μm, there is strong water absorption. So the optimized wavelength of illumination is around 1 μm for deep penetration in tissue imaging[50–53]. In order to excite the fluorescence protein which usually has absorption peak in visible band, we need to utilize two-photon or multiphoton excitation. The advantage of utilizing nonlinear excitation also offers the sectioning ability to remove out-of-focus image as well surface excitation. The higher the nonlinearity the better the SBR is possible. The use of 1,700 nm wavelength three-photon microscopy is reported to be able to get in-vivo mouse hippocampus image which is up to 1,700 μm depth[54].

By this point of view, it is better to build up a microscopy which use longer excitation wavelength for multiphoton excitation and at the same time it does not need any scanning to achieve sectioned planar image via parallel detector. For 3D-SIM, it is able to simply use longer excitation wavelength with multiphoton excitation, but still the nonlinear excitation itself is wide-field and there is little excitation intensity change along axial direction thus no sectioning ability is achieved by nonlinear process. So there will be lots of shot noise of the out-of-focus image remained in 3D-SIM image.

1.2 Temporal focusing (TF) technique

With the motivation to build up a wide-field multi-photon microscopy, people invent TF technique[55,56]. TF[55–75] is also called simultaneous spatial and temporal focusing (SSTF)[56,57] or spatiotemporal focusing (STF)[62]. This idea is realized by spatially separating spectral

components of pulses into a “rainbow beam” and recombining these components only at the spatial focus of the objective lens (Fig. 1.2 (a)). Thus, temporal pulse width becomes a function of distance with the Fourier transform limited (FTL) pulse width confined to the spatial focus (Fig. 1.2 (b)). As this happens only in one lateral direction and axial direction, the out-of-focus excitation intensity distribution is similar to a spatial line focusing case. The significance of TF is that it offers us a wide-field illumination with sectioning ability. This realizes optical sectioned scanningless TPEF microscopy and the sectioning ability origins from the illumination confinement.

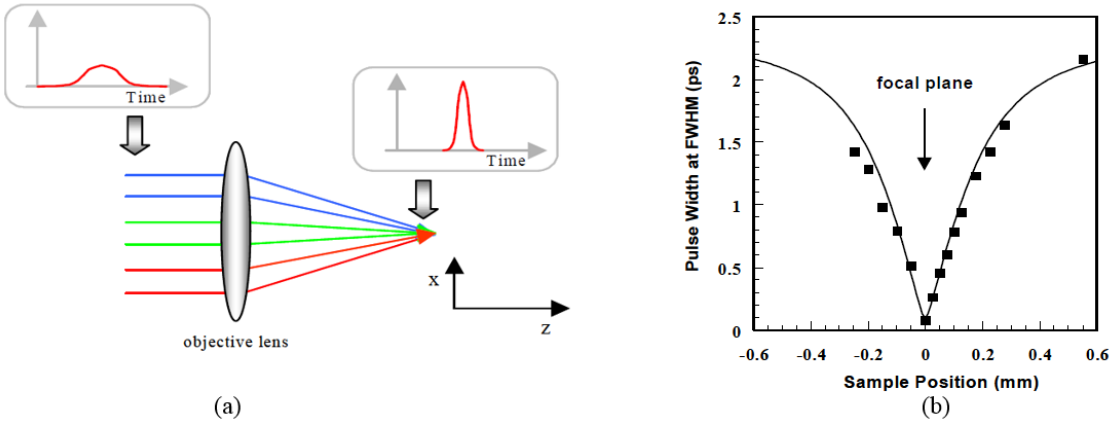

Fig. 1.2 (a) schematics of TF (b) pulse duration around focal plane[56]

1.2.1 Mechanism of TF

Figure. 1.3 (a) shows the typical wide-field TF setup. The pulse laser is first spatially dispersed by a grating and then recombined by a high NA objective lens. The whole system can be understood as an asymmetric 4f system. There are several groups giving the theoretical analysis for TF[61,64,76,77]. Here we simply give an intuitive introduction based on the change of the pulse amplitude distribution at time and lateral spatial domain. For this asymmetric 4f system, the focal plane is actually a magnified image of the pulse at grating surface and grating makes the pulse front tilted with propagation direction. So the pulse is laterally self-scanning at every axial plane with a repetition rate that equals the laser source. The scanning period is the same as the repetition rate of the laser pulse. As Fig. 1.2 (a) shows, due to the tilted pulse front at the focal plane and each axial plane, the size of the transient beam, which is the beam at every fixed time point in Figs. 1.2 (b) and (c), is much

smaller than the wide-field illumination region. Along the axial direction (z), this transient beam stretches and broadens similarly to a tightly focusing beam that is used for line-scanning microscopy. When we check the amplitude distribution in the lateral spatiotemporal domain (x,t), a slash denotes the linear relationship between space and time. This linear relationship originates from the grating where a pulse front starts to tilt with the axial direction. The slash's thickness in the time domain means the pulse duration, and in the lateral space domain (x), it means the size of the transient beam. The range of the slash in the time domain means the total self-scanning time, and in the space domain, it denotes the illumination region. Due to the diffraction effect, the transient beam broadens when the light propagates away from the focal plane. To maintain the linear relationship between time and space, the pulse duration stretches and broadens at the same pace as the size of the transient beam. Of course, the entire self-scanning time and the illumination region also changes but only slightly change around the focal plane. We can simply assume the self-scanning time and the illumination region are constant along the axial position as long as the illumination region is large enough. We ignore the dependence of the beam profile on another lateral coordinate *y*, since the spatial coupling only happens between the *x* and *z* directions. As we know, two-photon excitation (TPE) intensity is inversely proportional to the product of time and space at every axial plane. Thus broadening in the spatial temporal domain confines the TPE intensity at the focal plane. Mathematically, we can consider the integrated TPE intensity distribution, $I_{TPE}(z) = \iint |E(x,t,z,)|^4 dxdt$ in the lateral spatiotemporal domain for every axial plane to get the sectioning ability of TF.

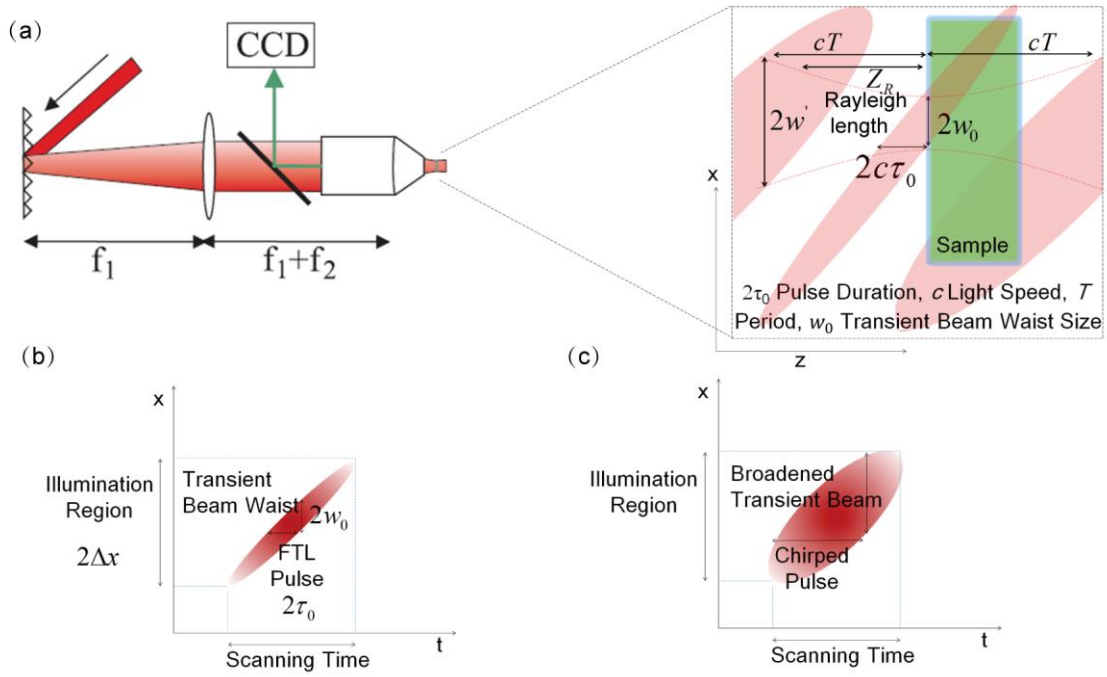

Fig. 1.3 (a) setup of TF microscopy and zoomed in view of tilted pulse front around focal plane[55], (b) spatiotemporal amplitude distribution of pulse front at focal plane, (c) spatiotemporal amplitude distribution of pulse front outside focal plane.

In details, if we investigate the angular dispersion at the focal region, using the Abbe sine condition for objective lens, we can approximately write it as

$$\theta(\omega) = \gamma_{grating}(\omega - \omega_c), \quad (1.3)$$

where $\theta(\omega)$ is the angle of the angular dispersion, ω is the angular frequency of the input light, and ω_c is the central angular frequency. $\gamma_{grating}$ is the spatial chirping rate, which is determined by the groove density of grating and magnified by the ratio between the focal length of the collimating lens and objective lens. In short, due to the asymmetric 4f setup in TF, the angular dispersion at the focal plane is magnified from that at the grating plane. The lateral spatial spectrum amplitude of the illumination light at the focal plane becomes

$$E(x, \omega) = a(x, \omega)e^{ikx\theta(\omega)}, \quad (1.4)$$

where x is the lateral coordinate in which light is dispersed by grating. Assuming that wave vector $k = 2\pi/\lambda_c$ is constant due to the limited spectral bandwidth of the input light, by a Fourier transform in the time domain, the linear relationship in Eq. (1.3) becomes a delay term that is linear to the lateral position:

$$E(x,t) \propto A(x, t - Delay),\ \ Delay = k\gamma_{grating} x. \quad (1.5)$$

From the delay term, we know that the slope in Fig. 1.2 (b) is $1/k\gamma_{grating}$, and thus the transient beam waist size is $\tau_0/k\gamma_{grating}$, where $\sqrt{2In2}\tau_0$ is the Fourier transform limited FWHM pulse width. We assume that the temporal distribution is a Gaussian distribution that mathematically means $A(x,t) = A(x) \times exp[-(t/\tau_0)^2]$. $A(x)$ is the spatial amplitude distribution of the wide illumination region other than the transient beam. To make the analysis simple, we assume that the shape of $A(x)$ is rectangular and its size is constant and much bigger than the transient beam size. In the spectrum domain, we also have $\alpha(x,\omega) = A(x) \times exp[-(\omega/\Omega)^2]$. Here, $\sqrt{2In2}\Omega$ is the FWHM bandwidth of the input light and $\tau_0\Omega = 2$. Then we get the following transient beam waist (Gaussian beam) size at the focal plane:

$$w_0 = \lambda_c / \pi\theta_0 ,\ \ \theta_0 = \gamma_{grating}\Omega. \quad (1.6)$$

θ_0 is around half of the total dispersing angle and we regard it as effective NA of TF. On the other hand, it is also the diverging angle of the transient beam. The shape of the transient beam in lateral space is the same as the shape of the pulse in the time domain (Eq. (1.5)). The Gaussian transient beam has a Rayleigh length:

$$Z_R = \lambda_c / \pi\theta_0^2 . \quad (1.7)$$

The propagation of the transient beam along the axial position can be regarded as the propagation of the Gaussian beam. Therefore, the TPE intensity distribution of TF can be obtained by an illumination model from the line focusing Gaussian beam:

$$I_{TPE\text{-}TF}(z) = I_0 / \sqrt{1 + (z / z_R)^2} . \quad (1.8)$$

This equation implies that wide-field TF has the similar sectioning ability to a spatial line focusing TPEF microscopy in terms of sectioning resolution and decay speed of out-of-focus TPE intensity. In order to achieve better sectioning ability as typical point scanning TPEF microscopy, people can spatially focus the beam in another lateral spatial domain (*y*). This is called line scanning TF microscopy where we need to scan the pulse in y direction. On the other hand, for the field of view of TF, it is independent with the

sectioning ability and in practical limited by the optical design of the objective lens which is the same situation for point scanning TPEF microscopy and confocal microscopy.

1.2.2 Applications of TF

People first demonstrate a line scanning TF microcopy to make video rate TPEF microscopy available as the excitation intensity is not enough for the wide-field. To realize a practical wide-field TF microscopy, we need have enough peak power to excite a large field of view and also a fast and sensitive camera to acquire the emission signal. Cheng et al. integrate a 10 kHz repetition rate chirped pulse amplification (CPA) laser featuring high instantaneous peak power (maximum 400 μJ/pulse at a 90 fs pulse width) and a Thermoelectric-cooled, ultra-sensitive photon detecting, electron multiplying charge-coupled camera into a spatiotemporal focusing microscope. This configuration can produce multiphoton images with an excitation area larger than 200 × 100 μm^2 at a frame rate greater than 100 Hz. Brownian motions of fluorescent microbeads as small as 0.5 μm were observed in real-time with a lateral spatial resolution of less than 0.5 μm and a sectioning resolution of approximately 3.5 μm.

Wide-field excitation also offers us a way for spatially selected excitation. For optogenetic control of neuronal activity, single cell excitation is another important application of TF. In order to achieve a single cell excitation, a volume precise of ~ ten μm^3 is necessary. For point scanning method, it cannot excite every point at the same time. For wide-field illumination, it does not have the accuracy in axial direction. Since TF has both wide-field and sectioning ability, it opens a new toolbox. People use generalized phase contrast or computer generalized holography method to create spatial pattern at TF focal plane. TPE patterns generated large photocurrents in Channelrhodopsin-2-expressing cultured cells and neurons in mouse acute cortical slices. The amplitudes of the photocurrents can be precisely modulated by controlling the size and shape of the excitation volume and, thereby, be used to trigger single action potentials or trains of action potentials. In addition, TF illumination is robust in scattering media. TF performs an ultrafast self line scanning at the image plane, while for non-TF case the entire image is illuminated simultaneously. Without TF, scattered photons interfere with the ballistic ones throughout

the entire illuminated region. In contrast, with TF, only a thin line is illuminated at each moment, and in order to interfere with the ballistic photons, scattered photons have to scatter onto it, which is an event with a much lower probability. This makes the illumination field less affected by scattering.

Another important application of TF is to achieve super-resolution for 3D volumetric imaging. 3D photoactivated localization microscopy (PALM) is achieved by TF. PALM or stochastic optical reconstruction microscopy (STORM) usually use thin biological samples in combination with total internal reflection, thus limiting the imaging depth to a fraction of an optical wavelength. However, to study whole cells or organelles that are typically up to 15 μm deep into the cell, the extension of these methods to a 3D super resolution technique is required. TF PALM realized an advance in optical microscopy that enables imaging of protein distributions in cells with a lateral localization precision better than 50 nm at multiple imaging planes deep in biological samples.

There are many other applications of TF[78–90]. For example, by tuning the dispersion of input laser pulse, we have the ability to move the focal plane. This opens a way to use fiber delivery system to do remote axial scanning. And although TF was developed for TPEF microscopy at first, people also use this technique for laser processing. Similar to fast 3D imaging, TF can achieve high throughput 3D fabrication. People also use TF to realize backside processing in order to achieve high aspect ratio inside transparent material. Another group use TF to independently control the lateral and axial size in laser fabrication. TF is also investigated to have less ablation for 3D laser processing. These developments of TF realize precise laser fabrication which is not available by traditional spatial or temporal manipulation of laser pulse.

1.3 Objective of this research

This research focus on the problem of current TF and find out solutions for it. In addition, I add additional functions for TF in order to improve the performance of TF imaging. In this section, I start from the problems of TF and then the general issues in deep and dense

sample imaging as the object of this research. Then I introduce the arrangement of this thesis.

1.3.1 Problems of TF and objective of this research

The first problem of TF is that the sectioning ability of TF is worse than either confocal microscopy or point scanning TPEF microscopy in terms of both sectioning resolution and decay speed of out-of-focus TPEF intensity. This problem arises from the fact that the spatiotemporal coupling only occurs at one-dimensional (1-D) lateral direction. Although we can use spatial focusing at another 1-D lateral direction to improve the sectioning ability, this lose the wide-field feature of TF. It not only lose the ability of single shot wide-field TPEF image but also lose the ability for patterned TPE. This drive us a question: can we achieve 2-D spatiotemporal coupling so as to improve the sectioning ability as well as retain the wide-field feature in TF?

The second problem of TF is more specific to TPEF microscopy. As we use parallel detector such as CCD and CMOS to collect the emission light. In deep and dense sample imaging, the scattering of emission light is strong. This cause huge amount of background fluorescence remained in the image, which significantly reduce the SBR of the image and limits the imaging depth. This problem is the same problem in multi-focal microscopy. In multi-focal microscopy, we can reduce the degree of parallelization to solve this problem. However, in TF, it is not able to reduce the degree of parallelization and even we can do it, we will lose the feature of wide-field. How to remove the background fluorescence for wide-field TPEF microscopy is another challenging object in this research.

In addition to these two problems, I seek to solve another two general problems in optical microscopy. The first one is diffraction limitation. The best spatial resolution for a typical wide-field microscopy with visible light emission is ~200 nm in lateral direction, ~500 nm in axial direction respectively. And the best sectioning resolution for a point TPEF microscopy is ~1 μm. This resolution is enough for cell imaging (~ 10 μm) but limited to observe dendritic spines (< 2 μm), axons (0.1 μm – 10 μm), synapse (20-200 nm). So it is necessary to improve the spatial resolution (the FWHM of PSF) beyond diffraction limitation in wide-field TPEF microscopy for deep and dense sample imaging. Although it

is simple to combine PALM with TF TPEF microscopy, it fails in deep and dense sample imaging due to limited sectioning ability and background fluorescence. In addition, PALM require lots of raw images to reconstruct the super-resolution image, this is conflict to the aim for fast imaging. How to achieve super-resolution wide-field imaging in deep and dense sample as well as maintain the fast imaging speed is the third object of this research.

In imaging practice, the sample and environment differs from the ideal condition. The substantial distortions arise from the mismatch of refractive index among sample, immersion media and mounting media or the inhomogeneous refractive index distribution of sample itself. These distort the wavefront so that the phase of the spatial frequency is modulated. This will reduce the bandwidth in OTF and distort the shape of OTF. As a result, it degrades the spatial resolution and sectioning ability. In general, the magnitude of distortion increases with imaging depth, thus it is important to find a solution to overcome the degradation of spatial resolution and axial resolution in deep and dense sample imaging due to optical distortions. This is the fourth object of this research.

1.3.2 The arrangement of this thesis

In chapter 2, I aim to solve the first problem in TF. The focus is on the issue of excitation path in TF. I propose and demonstrate 2D-TF to improve the sectioning ability of TF the same as a point scanning TPEF microscopy as well as keep the wide-field feature. I start from the theoretical analysis and proof. Then I discuss the factor which affects the out-of-focus TPE intensity decay due to spatiotemporal interference. Upon this I decide to choose virtually imaged phased array (VIPA) to realize 2D-TF in experiment. In the first experiment, I use surface second harmonic generation (SHG) to verify our theory on TPE characteristic of 2D-TF. Upon this, I build up 2D-TF TPEF microscopy with optimized sectioning resolution. I evaluate the sectioning resolution and the improvement in imaging depth. At last, I demonstrate the fast 3D volumetric imaging in 2D-TF by imaging 3D Brownian motion.

In chapter 3, I aim to solve the second problem, the scattered emission background in TF microscopy. Moreover, I aim to solve the first general problem in optical microscopy, diffraction limitation. The focus is on the issue of emission path in TF. Both the objective

and approach are different in chapter 2 and chapter 3. In chapter 3, I combine 3D-SIM and TF, which I call 3D interferometric temporal focusing (ITF) microscopy to both remove background fluorescence and improve spatial resolution and sectioning resolution beyond diffraction limitation. This method relies on post-processing of multiple raw images and the reconstructed image can achieve background free image and super-resolution. The raw images have the same imaging qualities (spatial resolution, sectioning ability and SBR) compared to TF. I start from the principle of 3D-ITF to not only give a proof of these abilities but also introduce the method in its imaging reconstruction. Then I use digital micromirror device (DMD) to build up 3D-ITF in experiment. Next, I evaluate the super sectioning resolution and the super-resolution in 3D-ITF microscopy via 3D volumetric imaging of biological phantom. Last, I prove the ability to remove background fluoresce in 3D-ITF imaging by imaging a dense sample.

In chapter 4, I extend the study in chapter 3 to investigate the performance of 3D-ITF imaging in distorted optics which is the second general problem in optical microscopy. I theoretically study this by considering the influence in both illumination and emission then I conclude the distorted PSF and OTF. Upon this, I show that there is redundancy in spatial spectrum domain for 3D-ITF imaging. Then through simulation, I first show the resistance of spatial resolution in 3D-ITF imaging when the measureable cut-off frequency in emission OTF is reduced. Then I show how the redundancy supports the resistance of spatial resolution and sectioning resolution in deep and dense sample imaging where wavefront distortion and background fluoresce exist.

In chapter 5, I summarize the achievements in theoretical and experimental work and give a prospect such as to combine the work in 2D-TF and 3D-ITF in order to solve all four problems in one technique.

References

1. Tsai, P. S. *et al.* Correlations of Neuronal and Microvascular Densities in Murine Cortex Revealed by Direct Counting and Colocalization of Nuclei and Vessels. *J. Neurosci.* **29,** 14553–14570 (2009).
2. Saido, T. C. Metabolism of amyloid β peptide and pathogenesis of Alzheimer's disease. *Proc. Jpn. Acad. Ser. B. Phys. Biol. Sci.* **89,** 321–39 (2013).
3. Benazzi, F. Various forms of depression. *Dialogues Clin. Neurosci.* **8,** 151–61 (2006).
4. Romo, R. & Salinas, E. Flutter Discrimination: neural codes, perception, memory and decision making. *Nat. Rev. Neurosci.* **4,** 203–218 (2003).
5. Kandel, E. R. The Molecular Biology of Memory Storage: A Dialogue Between Genes and Synapses. *Science.* **294,** 1030–1038 (2001).
6. Liu, C. *et al.* A subset of dopamine neurons signals reward for odour memory in Drosophila. *Nature* **488,** 512–516 (2012).
7. Wilson, T. Optical sectioning in fluorescence microscopy. *J. Microsc.* **242,** 111–116 (2011).
8. Wilson, T. Resolution and optical sectioning in the confocal microscope. *J. Microsc.* **244,** 113–121 (2011).
9. Pawley, J. B. *Handbook of biological confocal microscopy*. (Plenum Press, 1995).
10. Wilson, T. (Professor) & Sheppard, C. *Theory and practice of scanning optical microscopy*. (Academic Press, 1984).
11. Wilson, T. Confocal Light Microscopy. **483,** 416–427 (1986).
12. Theer, P., Hasan, M. T. & Denk, W. Two-photon imaging to a depth of 1000 μm in living brains by use of a Ti:Al_2O_3 regenerative amplifier. *Opt. Lett.* **28,** 1022 (2003).
13. Helmchen, F. & Denk, W. Deep tissue two-photon microscopy. *Nat. Methods* **2,** 932–940 (2005).
14. Denk, W., Strickler, J. H. & Webb, W. W. Two-photon laser scanning fluorescence microscopy. *Science* **248,** 73–6 (1990).
15. Rumi, M. & Perry, J. W. Two-photon absorption: an overview of measurements

and principles. *Adv. Opt. Photonics* **2,** 451 (2010).

16. Centonze, V. E. & White, J. G. Multiphoton excitation provides optical sections from deeper within scattering specimens than confocal imaging. *Biophys. J.* **75,** 2015–2024 (1998).
17. Brewersdorf, J., Pick, R. & Hell, S. W. Multifocal multiphoton microscopy J org. *Opt. Lett.* **23,** 655–657 (1998).
18. Bahlmann, K. *et al.* Multifocal multiphoton microscopy (MMM) at a frame rate beyond 600 Hz. *Opt. Express* **15,** 10991 (2007).
19. Sacconi, L. *et al.* Multiphoton multifocal microscopy exploiting a diffractive optical element. *Opt. Lett.* **28,** 1918–1920 (2003).
20. Fittinghoff, D., Wiseman, P. & Squier, J. Widefield multiphoton and temporally decorrelated multifocal multiphoton microscopy. *Opt. Express* **7,** 273–9 (2000).
21. Fittinghoff, D. N. & Squier, J. a. Time-decorrelated multifocal array for multiphoton microscopy and micromachining. *Opt. Lett.* **25,** 1213–1215 (2000).
22. Egner, A., Andresen, V. & Hell, S. W. Comparison of the axial resolution of practical Nipkow-disk confocal fluorescence microscopy with that of multifocal multiphoton microscopy: Theory and experiment. *J. Microsc.* **206,** 24–32 (2002).
23. Egner, A. & Hell, S. W. Time multiplexing and parallelization in multifocal multiphoton microscopy. *J. Opt. Soc. Am. A* **17,** 1192 (2000).
24. Semwogerere, D. & Weeks, E. R. Confocal Microscopy. *Encycl. Biomater. Biomed. Eng.* 1–10 (2005).
25. Egger, M. D. & Petrăn, M. New reflected-light microscope for viewing unstained brain and ganglion cells. *Science* **157,** 305–7 (1967).
26. Kim, K. H. *et al.* Multifocal multiphoton microscopy based on multianode photomultiplier tubes. *Opt. Express* **15,** 11658–11678 (2007).
27. Neil, M. A. A., Juškaitis, R. & Wilson, T. Method of obtaining optical sectioning by using structured light in a conventional microscope. *Opt. Lett.* **22,** 1905 (1997).
28. Karadaglić, D. & Wilson, T. Image formation in structured illumination wide-field fluorescence microscopy. *Micron* **39,** 808–818 (2008).
29. Neil, M. A. A., Juškaitis, R. & Wilson, T. Real time 3D fluorescence microscopy by two beam interference illumination. *Opt. Commun.* **153,** 1–4 (1998).

30. Lim, D., Chu, K. K. & Mertz, J. Wide-field fluorescence sectioning with hybrid speckle and uniform-illumination microscopy. *Opt. Lett.* **33,** 1819–1821 (2008).
31. Heintzmann, R. & Gustafsson, M. G. L. Subdiffraction resolution in continuous samples. *Nat. Photonics* **3,** 362–364 (2009).
32. Heintzmann, R. & Cremer, C. G. Laterally modulated excitation microscopy: improvement of resolution by using a diffraction grating. (1999) doi:10.1117/12.336833
33. Wang, M. *et al.* Gigapixel surface imaging of radical prostatectomy specimens for comprehensive detection of cancer-positive surgical margins using structured illumination microscopy. *Sci. Rep.* **6,** 1–16 (2016).
34. Thomas, B., Momany, M. & Kner, P. Optical sectioning structured illumination microscopy with enhanced sensitivity. *J. Opt.* **15,** 094004 (2013).
35. Shao, L., Kner, P., Rego, E. H. & Gustafsson, M. G. L. Super-resolution 3D microscopy of live whole cells using structured illumination. *Nat. Methods* **8,** 1044–1048 (2011).
36. Schermelleh, L. *et al.* Subdiffraction mulicolor imaging of the nuclear periphery with 3D structure illumination microscopy. *Science (80-.).* **320,** 1332–1336 (2008).
37. Dan, D. *et al.* DMD-based LED-illumination Super-resolution and optical sectioning microscopy. *Sci. Rep.* **3,** 1–7 (2013).
38. Gustafsson, M. G. L., Agard, D. A. & Sedat, J. W. Doubling the lateral resolution of wide-field fluorescence microscopy using structured illumination. (2000). doi:10.1117/12.384189
39. Frohn, J. T., Knapp, H. F. & Stemmer, A. True optical resolution beyond the Rayleigh limit achieved by standing wave illumination. *Proc. Natl. Acad. Sci.* **97,** 7232–7236 (2000).
40. Heintzmann, R. Saturated patterned excitation microscopy with two-dimensional excitation patterns. *Micron* **34,** 283–291 (2003).
41. Heintzmann, R., Jovin, T. M. & Cremer, C. Saturated patterned excitation microscopy—a concept for optical resolution improvement. *J. Opt. Soc. Am. A* **19,** 1599 (2002).

42. Gustafsson, M. G. L. Nonlinear structured-illumination microscopy: Wide-field fluorescence imaging with theoretically unlimited resolution. *Proc. Natl. Acad. Sci.* **102,** 13081–13086 (2005).
43. Gustafsson, M. G. L. *et al.* Three-dimensional resolution doubling in wide-field fluorescence microscopy by structured illumination. *Biophys. J.* **94,** 4957–4970 (2008).
44. Kner, P., Chhun, B. B., Griffis, E. R., Winoto, L. & Gustafsson, M. G. L. Super-resolution video microscopy of live cells by structured illumination. *Nat. Methods* **6,** 339–342 (2009).
45. Shaw, M., Zajiczek, L. & O'Holleran, K. High speed structured illumination microscopy in optically thick samples. *Methods* **88,** 11–19 (2015).
46. Bailey, B., Farkas, D. L., Taylor, D. L. & Lanni, F. Enhancement of axial resolution in fluorescence microscopy by standing-wave excitation. *Nature* **366,** 44–48 (1993).
47. Mandula, O. *et al.* Line scan - structured illumination microscopy super-resolution imaging in thick fluorescent samples. *Opt. Express* **20,** 24167 (2012).
48. Keller, P. J., Ahrens, M. B. & Freeman, J. Light-sheet imaging for systems neuroscience. *Nat. Methods* **12,** 27–29 (2014).
49. Planchon, T. A. *et al.* Rapid three-dimensional isotropic imaging of living cells using Bessel beam plane illumination. *Nat. Methods* **8,** 417–423 (2011).
50. Horton, N. G. *et al.* In vivo three-photon microscopy of subcortical structures within an intact mouse brain. *Nat. Photonics* **7,** 205–209 (2013).
51. Theer, P. & Denk, W. On the fundamental imaging-depth limit in two-photon microscopy. *J. Opt. Soc. Am. A* **23,** 3139 (2006).
52. Zipfel, W. R., Williams, R. M. & Webb, W. W. Nonlinear magic: multiphoton microscopy in the biosciences. *Nat. Biotechnol.* **21,** 1369–77 (2003).
53. Duck, F. A. *Physical Properties of Tissues : a comprehensive reference book*. (Elsevier Science, 1990).
54. Horton, N. G. *et al.* In vivo three-photon microscopy of subcortical structures within an intact mouse brain. *Nat. Photonics* **7,** 205–209 (2013).
55. Oron, D., Tal, E. & Silberberg, Y. Scanningless depth-resolved microscopy. *Opt.*

Express **13,** 1468 (2005).

56. Zhu, G., van Howe, J., Durst, M., Zipfel, W. & Xu, C. Simultaneous spatial and temporal focusing of femtosecond pulses. *Opt. Express* **13,** 2153 (2005).
57. Durst, M. E., Zhu, G. & Xu, C. Simultaneous Spatial and Temporal Focusing in Nonlinear Microscopy. *Opt. Commun.* **281,** 1796–1805 (2008).
58. Dana, H. & Shoham, S. Remotely scanned multiphoton temporal focusing by axial grism scanning. *Opt. Lett.* **37,** 2913–5 (2012).
59. Dana, H., Kruger, N., Ellman, A. & Shoham, S. Line temporal focusing characteristics in transparent and scattering media. *Opt. Express* **21,** 5677–87 (2013).
60. Dana, H. & Shoham, S. Numerical evaluation of temporal focusing characteristics in transparent and scattering media. *Opt. Express* **19,** 4937–4948 (2011).
61. Yew, E. Y. S., Sheppard, C. J. R. & So, P. T. C. Temporally focused wide-field two-photon microscopy: Paraxial to vectorial. *Opt. Express* **21,** 12951 (2013).
62. Sun, B. *et al.* Four-dimensional light shaping: Manipulating ultrafast spatiotemporal foci in space and time. *Light Sci. Appl.* **7,** 17117 (2018).
63. Hernandez, O. *et al.* Three-dimensional spatiotemporal focusing of holographic patterns. *Nat. Commun.* **7,** 1–10 (2016).
64. Durst, M. E., Zhu, G. & Xu, C. Simultaneous spatial and temporal focusing for axial scanning. *Opt. Express* **14,** 12243 (2006).
65. Yu, J.-Y. *et al.* Wide-field optical sectioning for live-tissue imaging by plane-projection multiphoton microscopy. *J. Biomed. Opt.* **16,** 116009 (2011).
66. Yu, J.-Y., Holland, D. B., Blake, G. A. & Guo, C.-L. The wide-field optical sectioning of microlens array and structured illumination-based plane-projection multiphoton microscopy. *Opt. Express* **21,** 2097 (2013).
67. Therrien, O. D., Aubé, B., Pagès, S., Koninck, P. De & Côté, D. Wide-field multiphoton imaging of cellular dynamics in thick tissue by temporal focusing and patterned illumination. *Biomed. Opt. Express* **2,** 696 (2011).
68. Vaziri, A. & Shank, C. V. Ultrafast widefield optical sectioning microscopy by multifocal temporal focusing. *Opt. Express* **18,** 19645 (2010).
69. Cheng, L.-C. *et al.* Spatiotemporal focusing-based widefield multiphoton

microscopy for fast optical sectioning. *Opt. Express* **20,** 8939 (2012).

70. Papagiakoumou, E., de Sars, V., Oron, D. & Emiliani, V. Patterned two-photon illumination by spatiotemporal shaping of ultrashort pulses. *Opt. Express* **16,** 22039 (2008).
71. Papagiakoumou, E. *et al.* Functional patterned multiphoton excitation deep inside scattering tissue. *Nat. Photonics* **7,** 274–278 (2013).
72. Papagiakoumou, E. *et al.* Scanless two-photon excitation of channelrhodopsin-2. *Nat. Methods* **7,** 848–54 (2010).
73. Vaziri, A., Tang, J., Shroff, H. & Shank, C. V. Multilayer three-dimensional super resolution imaging of thick biological samples. *Proc. Natl. Acad. Sci. U. S. A.* **105,** 20221–6 (2008).
74. Vaziri, A. & Emiliani, V. Reshaping the optical dimension in optogenetics. *Curr. Opin. Neurobiol.* **22,** 128–37 (2012).
75. Bègue, A. *et al.* Two-photon excitation in scattering media by spatiotemporally shaped beams and their application in optogenetic stimulation. *Biomed. Opt. Express* **4,** 2869–79 (2013).
76. Durfee, C. G., Greco, M., Block, E., Vitek, D. & Squier, J. a. Intuitive analysis of space-time focusing with double-ABCD calculation. *Opt. Express* **20,** 14244–59 (2012).
77. He, F. *et al.* Independent control of aspect ratios in the axial and lateral cross sections of a focal spot for three-dimensional femtosecond laser micromachining. *New J. Phys.* **13,** 083014 (2011).
78. He, F. *et al.* Fabrication of microfluidic channels with a circular cross section using spatiotemporally focused femtosecond laser pulses. *Opt. Lett.* **35,** 1106 (2010).
79. Kim, D. & So, P. T. C. High-throughput three-dimensional lithographic microfabrication. *Opt. Lett.* **35,** 1602 (2010).
80. Lien, C.-H., Abrigo, G., Chen, P.-H. & Chien, F.-C. Two-color temporal focusing multiphoton excitation imaging with tunable-wavelength excitation. *J. Biomed. Opt.* **22,** 026008 (2017).
81. Straub, A., Durst, M. E. & Xu, C. High speed multiphoton axial scanning through

an optical fiber in a remotely scanned temporal focusing setup. *Biomed. Opt. Express* **2,** 80–8 (2010).

82. Jiang, J. *et al.* Fast 3-D temporal focusing microscopy using an electrically tunable lens. *Opt. Express* **23,** 24362 (2015).
83. Li, Y.-C. *et al.* Fast multiphoton microfabrication of freeform polymer microstructures by spatiotemporal focusing and patterned excitation. *Opt. Express* **20,** 19030–8 (2012).
84. Vitek, D. N. *et al.* Temporally focused femtosecond laser pulses for low numerical aperture micromachining through optically transparent materials. *Opt. Express* **18,** 18086–94 (2010).
85. Zeng, B. *et al.* Enhancement of peak intensity in a filament core with spatiotemporally focused femtosecond laser pulses. *Phys. Rev. A - At. Mol. Opt. Phys.* **84,** 1–7 (2011).
86. Kammel, R. *et al.* Enhancing precision in fs-laser material processing by simultaneous spatial and temporal focusing. *Light Sci. Appl.* **3,** 1–8 (2014).
87. He, F. *et al.* Independent control of aspect ratios in the axial and lateral cross sections of a focal spot for three-dimensional femtosecond laser micromachining. *New J. Phys.* **13,** 083014 (2011).
88. Vitek, D. N. *et al.* Spatio-temporally focused femtosecond laser pulses for nonreciprocal writing in optically transparent materials. *Opt. Express* **18,** 24673–24678 (2010).
89. He, F. *et al.* Characterization and control of peak intensity distribution at the focus of a spatiotemporally focused femtosecond laser beam. *Opt. Express* **22,** 9734 (2014).
90. Zhang, S., Asoubar, D., Kammel, R., Nolte, S. & Wyrowski, F. Analysis of pulse front tilt in simultaneous spatial and temporal focusing. *J. Opt. Soc. Am. A. Opt. Image Sci. Vis.* **31,** 2437–46 (2014).

Chapter 2

Two-dimensional temporal focusing microscopy

In order to improve the sectioning ability by TPE in TF up to that in point-scanning TPEF microscopy, the fundamental issue is to fully use the aperture of the objective lens. In a general rule, for any types of microscopy, it is the solid angle of the aperture of the objective lens which determines spatial resolution and sectioning ability. TF (which I also call 1D-TF) only disperses the light into 1D space by grating, it has so far limited the axial resolution to a line focusing system. Moreover, the relatively high out-of-focus TPE intensity compared to point-scanning TPEF limits its imaging depth. Here, I use a cross-disperser setup to extend 1D-TF to a 2D-TF[1]. The same cross-disperser setup was previously used for wavelength de-multiplexing in optical communication, wavelength-parallel polarization sensing, and frequency-comb spectroscopy[2–5]. This results in a 2D matrix of dispersed light as shown in Fig. 2.1. In 2D-TF, I set the back aperture of the objective lens after this 2D matrix of dispersed light. I call this 2D-TF because at the out-of-focus plane of the objective lens, all of the spectrum components are spatially dispersed into the entire plane rather than a line. Using this setting, at the out-of-focus plane, the pulse is further stretched in the time domain compared to 1D-TF so that the axial excitation confinement ability equals a point-scanning system while I retain the wide-field illumination feature. Also we can understand by using the point of view of transient beam. Due to the 2D spatiotemporal coupling, pulse front is tilted in a 2D fashion as the insert in Fig. 2.1 shows. A discrete pulse front tilt in *y* direction combined with continuous pulse front tilt in *x* direction generate a transient beam the same as the focused beam in point scanning TPEF microscopy. Thus with diffraction, the transient beam intensity spreads out-of-focus to support the sectioning ability the same way as point scanning TPEF microscopy. By using this method, such advantages of 1D-TF as its fast illumination and its ability to combine with a technique that requires wide-field illumination are maintained for 2D-TF. In addition, it has recently been found that TF has relative scattering-resistance

of axial sectioning and arbitrary patterns using a wide-field approach. Since in both dimensions I use TF rather than spatial focusing, 2D-TF must inherit this characteristic with improved axial resolution and reduced out-of-focus background to become a promising illumination tool for processing in transparent material and deep multi-photon excitation when the fluorescent material is optically dense.

In this chapter, I describe the theoretical analysis and experimental verification for improved sectioning ability and reduced out-of-focus background in 2D-TF microscopy as well as a demonstration of fast 3D volumetric imaging. In section 2.1, I developed an analytical approach to evaluate the spatiotemporal profile evolution of 2D-TF along the axial direction and prove the improvement of sectioning ability in theory. In section 2.2, I show that the free spectral range (FSR) of the 2D spectral disperser is an important factor to determine the out-of-focus excitation level. An extremely small FSR is necessary to reduce the out-of-focus excitation by several orders of magnitude compared with a grating-based TF. In section 2.3, I choose VIPA based 2D spectral disperser to build up the 2D-TF setup. I utilize surface SHG to experimentally verify both the sectioning resolution and the decay speed of out-of-focus TPE intensity following the theoretical conclusions. In section 2.4, I build up a 2D-TF microscope with a high NA objective lens. I evaluated the sectioning resolution and confirm that the 2D-TF microscopy can achieve the same sectioning resolution as point scanning TPEF microscopy. In section 2.5, I demonstrate the ability of 2D-TF for fast 3D volumetric imaging through 3D Brownian motion imaging.

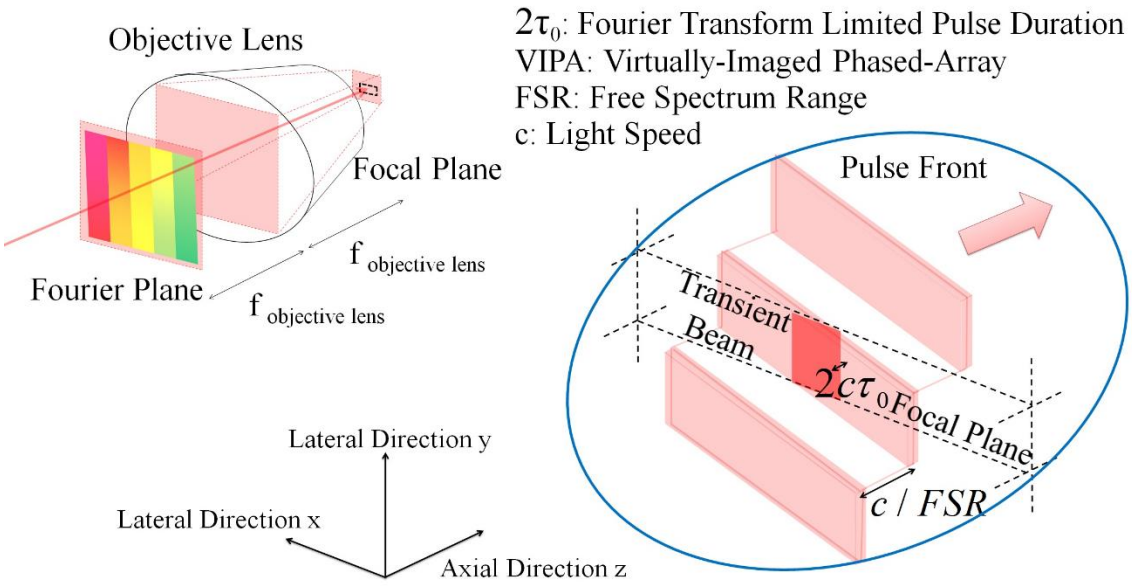

Fig. 2.1 Idea of 2D-TF. The insert shows the magnified pulse front at focal plane for intuitive understanding.

2.1 Principle

In this part, I aim to give an analytical approach for the temporal profile and axial confinement ability of proposed 2D-TF. The idea of 2D-TF is illustrated in Fig. 2.2, same as a 2D pulse shaper, at the Fourier plane of a 2D spectral disperser, each spectrum component is focused while the whole spectrum is collimated. At the focal plane, light field is optically Fourier transformed by the objective lens. If the pulse is chirp free at focal plane, there is only liner spectrum phase remained. Along slow chirping direction (x), linear phase is the same as 1D-TF case. However, along fast chirping direction (y), linear phase from different diffraction orders exists periodically with a period of FSR. Thus I can write the spatiotemporal profile at focal plane $(z=0)$ as,

$$E(x,y,\omega,z=0)=\left\{A_x(x)E(\omega)\exp\left[ikx\theta_x(\omega)\right]\otimes\delta\left(\omega-\omega_c\right)\right\}\times\left\{A_y(y)S(\omega)\exp\left[iky\theta_y(\omega)\right]\otimes\sum_{n=-\infty}^{+\infty}\delta\left(\omega-\omega_n\right)\right\}, \quad (2.1)$$

where $A_x(x)=\exp[-(x/\Delta x)^2]$ and $A_y(y)=\exp[-(y/\Delta y)^2]$ is the beam profile, $E(\omega)=\exp[-(\omega/\Omega)^2]$ is the spectrum profile of the pulse with a FWHM of $\sqrt{2In2}\Omega$, ω_c is the central angular frequency, along x direction $\theta_x(\omega)=\gamma_x\omega$ describes the linear spectrum phase; along y direction $S(\omega)=\exp[-(\omega/\Omega_s)^2]$ is the diffraction efficiency profile of each diffraction order with a FWHM of $\sqrt{2In2}\Omega_s$, ω_n is the central angular frequency for each diffraction order with ω_{n+1}-ω_n=2πFSR, and $\theta_y(\omega)=\gamma_y\omega$ describes the linear spectrum phase. To simplify calculation, I assume that the wavevector of each frequency is approximately same as $k=2\pi/\lambda_c$, the wavevector of the center wavelength of the pulse.

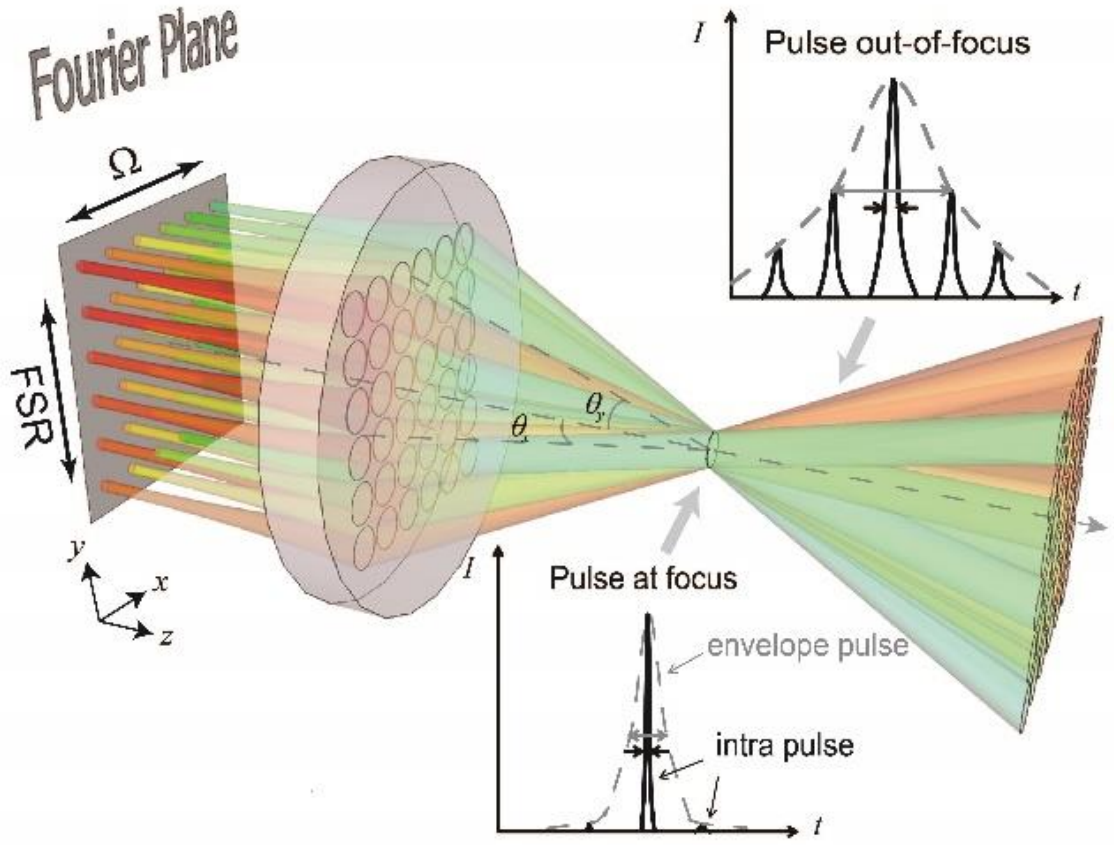

Fig. 2.2 The schematic of 2D-TF[1].

In order to know the spatiotemporal profile away the focal plane, by using the paraxial approximation, I can first do Fourier transform in spatial domain and add the quadratic phase due to diffraction, the field becomes

$$\begin{aligned}\tilde{E}(k_x,k_y,\omega,z) \propto & \left\{\tilde{A}_x\left[k_x-k\theta_x(\omega)\right]E(\omega)\exp(-i\frac{zk_x^2}{2k})\otimes\delta\left(\omega-\omega_c\right)\right\} \\ & \times\left\{\tilde{A}_y\left[k_y-k\theta_y(\omega)\right]S(\omega)\exp(-i\frac{zk_y^2}{2k})\otimes\sum_{n=-\infty}^{+\infty}\delta\left(\omega-\omega_n\right)\right\}\end{aligned}, \quad (2.2)$$

where $\tilde{A}_x\left(k_x\right)=\exp[-\left(k_x\Delta x/2\right)^2]$ and $\tilde{A}_y\left(k_y\right)=\exp[-\left(k_y\Delta y/2\right)^2]$. In Eq. (2.2), I ignore all the constant phase terms that have no relationship with either the lateral position or the frequency. In order to do inverse Fourier transform back to the spatial domain, I consider the spatial change of each frequency along its own propagation direction, $k_x^{'}=k_x-k\theta_x(\omega)$ and $k_y^{'}=k_y-k\theta_y(\omega)$. By this view, Eq. (2.2) becomes

$$\begin{aligned}\tilde{E}(k_x^{'},k_y^{'},\omega,z) \propto & \left\{\tilde{A}_x(k_x^{'})\exp\left[-i\frac{zk_x^{'2}}{2k}-iz\theta_x(\omega)k_x^{'}-i\frac{zk\theta_x^2(\omega)}{2}\right]E(\omega)\otimes\delta\left(\omega-\omega_c\right)\right\} \\ & ...\times\left\{\tilde{A}_y(k_y^{'})\exp\left[-i\frac{zk_y^{'2}}{2k}-iz\theta_y(\omega)k_y^{'}-i\frac{zk\theta_y^2(\omega)}{2}\right]S(\omega)\otimes\sum_{n=-\infty}^{+\infty}\delta\left(\omega-\omega_n\right)\right\}.\end{aligned}$$

(2.3)

In Eq. (2.3), I find out the dispersion terms $\exp[-izk\theta_x^2(\omega)/2]$ and $\exp[-izk\theta_y^2(\omega)/2]$ which are generated from the diffraction due to the spatiotemporal coupling. By inverse Fourier transform of Eq. (2.3) in the spatial domain, I get

$$\begin{aligned}E(x,y,\omega,z) \propto & \left\{A_x^{'}(x^{'})\exp\left[\frac{ikx^{'2}}{2R_x(z)}+ikx\theta_x(\omega)\right]E(\omega)\exp\left[-i\frac{zk\theta_x^2(\omega)}{2}\right]\otimes\delta\left(\omega-\omega_c\right)\right\} \\ & \times\left\{A_y^{'}(y^{'})\exp\left[\frac{iky^{'2}}{2R_y(z)}+iky\theta_y(\omega)\right]S(\omega)\exp\left[-i\frac{zk\theta_y^2(\omega)}{2}\right]\otimes\sum_{n=-\infty}^{+\infty}\delta\left(\omega-\omega_n\right)\right\}\end{aligned},$$

(2.4)

where $x^{'}=x-z\theta_x(\omega)$, $y^{'}=y-z\theta_y(\omega)$, $A_x^{'}(x^{'})=\exp[-\left(x^{'}/\Delta x^{'}\right)^2]$, $A_y^{'}(y^{'})=\exp[-\left(y^{'}/\Delta y^{'}\right)^2]$, $R_x(z)=z\left[1+(z_{mx}/z)^2\right]$ and $R_y(z)=z\left[1+(z_{my}/z)^2\right]$ with

$\Delta x^{'} = \Delta x\sqrt{1+(z/z_{mx})^2}$, $\Delta y^{'} = \Delta y\sqrt{1+(z/z_{my})^2}$, $z_{mx} = \lambda_c / \pi\theta_{mx}^2$, $z_{my} = \lambda_c / \pi\theta_{my}^2$, $\theta_{mx} = \lambda_c / \pi\Delta x$ and $\theta_{my} = \lambda_c / \pi\Delta y$.

For each frequency outside the focal plane, $x^{'}$ and $y^{'}$ describe the 2D spatial chirp, $\Delta x^{'}$ and $\Delta y^{'}$ describe its spatial broadening with Rayleigh length of z_{mx} and z_{my}, beam divergence of θ_{mx} and θ_{my}, and radiuses of curvature of $R_x(z)$ and $R_y(z)$. In order to do inverse Fourier transform in temporal domain, I consider local spectrum and local dispersion of each spatial point. Then I rewrite Eq. (2.4) as:

$$E(x,y,\omega,z) \propto \left\{ A_x^{''}(x)E^{'}(\omega)\exp\left[-i\frac{zk\theta_x^2(\omega)}{2}(1-\frac{z}{R_x(z)}) + i\varphi_x(x,\omega,z) \right] \otimes \delta\left(\omega-\omega_c-\alpha_x x\right) \right\}$$
$$\times \left\{ A_y^{''}(y)S^{'}(\omega)\exp\left[-i\frac{zk\theta_y^2(\omega)}{2}(1-\frac{z}{R_y(z)}) + i\varphi_y(y,\omega,z) \right] \otimes \sum_{n=-\infty}^{+\infty}\delta\left(\omega-\omega_n-\alpha_y y\right) \right\},$$

(2.5)

where $A_x^{''}(x) = \exp[-\left(x/\Delta x^{''}\right)^2]$, $A_y^{''}(y) = \exp[-\left(y/\Delta y^{''}\right)^2]$, $E^{'}(\omega) = \exp\left[-\left(\omega/\Omega^{'}\right)^2\right]$, $S^{'}(\omega) = \exp\left[-\left(\omega/\Omega_s^{'}\right)^2\right]$, $\varphi_x(x,\omega,z) = kx\theta_x(\omega)\frac{\Delta x^2}{\Delta x^{''2}}$, $\varphi_y(y,\omega,z) = ky\theta_y(\omega)\frac{\Delta y^2}{\Delta y^{''2}}$, $\alpha_x = \frac{z\theta_x\Omega}{\Delta x^{''2}}$ and $\alpha_y = \frac{z\theta_y\Omega_s}{\Delta y^{''2}}$ with $\frac{\Delta x^{''2}}{\Delta x^{'2}} = \frac{\Omega^2}{\Omega^{'2}} = 1+\frac{z^2\theta_x^{\ 2}}{\Delta x^{'2}}$, $\frac{\Delta y^{''2}}{\Delta y^{'2}} = \frac{\Omega_s^2}{\Omega_s^{'2}} = 1+\frac{z^2\theta_y^{\ 2}}{\Delta y^{'2}}$, $\theta_x = \gamma_x\Omega$ and $\theta_y = \gamma_y\Omega_s$.

$E^{'}(\omega)$ and $S^{'}(\omega)$ describe the local spectrum profile. The local bandwidths are narrowed and local central wavelength shifts, $\alpha_x x$ and $\alpha_y y$ occur due to the 2D spatial chirp. $A_x^{''}(x)$ and $A_y^{''}(y)$ describe the pulse's entire illumination region, which is broadened also due to the 2D spatial chirp. In Eq. (2.5), I ignore the constant phase terms that have no relationship with the frequency. By inverse Fourier transform in temporal domain (for detailed calculations, see Eq. (2.7) - (2.10)), I get

$$\left|e(x,y,t,z)\right| \propto \left[A_x^{"}(x) e^{'}(t-\frac{x}{v_x}) \right] \otimes \left[A_y^{"}(y) s^{'}(t-\frac{y}{v_y}) \times \sum_{n=-\infty}^{+\infty} \delta(t-n/FSR) \right], \quad (2.6)$$

where $e^{'}(t) = \exp\left[-(t/\tau^{'})^2\right]$, $s^{'}(t) = \exp\left[-(t/\tau_s^{'})^2\right]$, $v_x = \frac{\Delta x^{"2}}{\Delta x^2 k \gamma_x}$ and $v_y = \frac{\Delta y^{"2}}{\Delta y^2 k \gamma_y}$ with $\tau^{'} = \frac{2\Delta x}{\Omega \Delta x^{"}} \sqrt{1+(z/z_{Rx})^2}$, $\tau_s^{'} = \frac{2\Delta y}{\Omega_s \Delta y^{"}} \sqrt{1+(z/z_{Ry})^2}$, $z_{Rx} = \lambda_c / \pi(\theta_x^{\,2} + \theta_{mx}^2)$ and $z_{Ry} = \lambda_c / \pi(\theta_y^{\,2} + \theta_{my}^2)$. The derivation of τ' and τ_s' will be shown later in Eq. (2.7).

As Fig. 2.2 shows, the temporal profile at a specified spatial point, e.g. (x=0, y=0, z), is periodically spaced pulses with a period of $1/FSR$. The intra pulse is determined by $e^{'}(t)$ and the entire envelope is determined by $s^{'}(t)$. The similar temporal profile was also shown in Lee's work. v_x and v_y describes the titled pulse front and v_x in 1D-TF has been measured by the interferometric method[6]. In order to achieve a uniform illumination along y direction without wasting input power, I set $2\tau_s^{'}(z=0) = 1/FSR$ in temporal domain which means $\Omega_s = 4FSR$ in spectral domain. Figure 2.3 shows the spatiotemporal profile around focal plane. In analogy to 1D-TF, the pulse front is tilted in both x and y lateral direction in 2D-TF. The slope, self-scanning speed in Figs. 2.3 (c) and (e) is determined by v_x and v_y respectively. Once the beam propagates away focal plane, the parabolic wavefront transfers to the dispersion in the laser pulse. The dispersion broadens the pulse width, τ' and the pulse train envelope, τ_s'. Thus the transient beam size also broadens away the focal plane in order to keep the linear relationship between time and space as Figs. 2.3 (d) and (f) show. $\Delta x''^2/\Delta x^2$ and $\Delta y''^2/\Delta y^2$ represent the beam size changing of the whole TF pulse. This change is much smaller than transient beam size changing as the huge difference between their Rayleigh lengths as mentioned later. So around focal plane, when I evaluate the sectioning resolution, I can regard the beam size as constant. However, when beam propagate away the monochromatic Rayleigh length, z_{mx} and z_{my} respectively. The beam size changing cannot be ignored. So the slope, v_x and v_y in Figs 2.3 (d) and (f) start

to increase, which means the tilting angles of the pulse front decrease. This tell us that at this condition, 2D-TF tend to become a conventional wide-field case. On the other hand, the pulse width, τ' and the pulse train envelope, τ_s' reach their maximum value which is determined by the spectral resolution of the 2D spatial disperser. So the decreasement of the TPE intensity relies on the spatial broadening of the beam size when pulse propagates away the Rayleigh length, z_{mx} and z_{my} respectively. Figure 2.3 gives us a rough idea of the sectioning ability, next I will give a mathematical proof of the sectioning ability of 2D-TF.

Along propagation direction, compared with 1D-TF, not only the intra pulse but also the envelope pulse are stretched so that the TPE intensity is further confined around focal plane. Figure 2.4 is a summary how I derivate this temporal profile by decomposing the Fourier transform in three parts. First, each train pulse, $e'(t)$ is the Fourier transform of $E'(\omega)\exp\left[-i\frac{zk\theta_x^2(\omega)}{2}(1-\frac{z}{R_x(z)})+i\varphi_x(x,\omega,z)\right]$. Then the pulse train envelope, $s'(t)$ is the Fourier transform of $S'(\omega)\exp\left[-i\frac{zk\theta_y^2(\omega)}{2}(1-\frac{z}{R_y(z)})+i\varphi_y(y,\omega,z)\right]$. Finally by convolving each train pulse with a series of delta function $\sum_{n=-\infty}^{+\infty}\delta(t-n/FSR)$ which is the Fourier transform of $\sum_{n=-\infty}^{+\infty}\delta\left(\omega-\omega_n-\alpha_y y+\omega_c+\alpha_x x\right)$, I get the temporal profile $\left|e(x,y,t,z)\right|$. Note that the linear phases, $\varphi_y(y,\omega,z)$ and $\varphi_y(y,\omega,z)$ only give temporal linear shift and have no influence on the pulse widths, τ' and τ_s'. And I ignore the relative phase difference between each delta function in $\sum_{n=-\infty}^{+\infty}\delta(t-n/FSR)$ because it has no influence on the amplitude, $\left|e(x,y,t,z)\right|$.

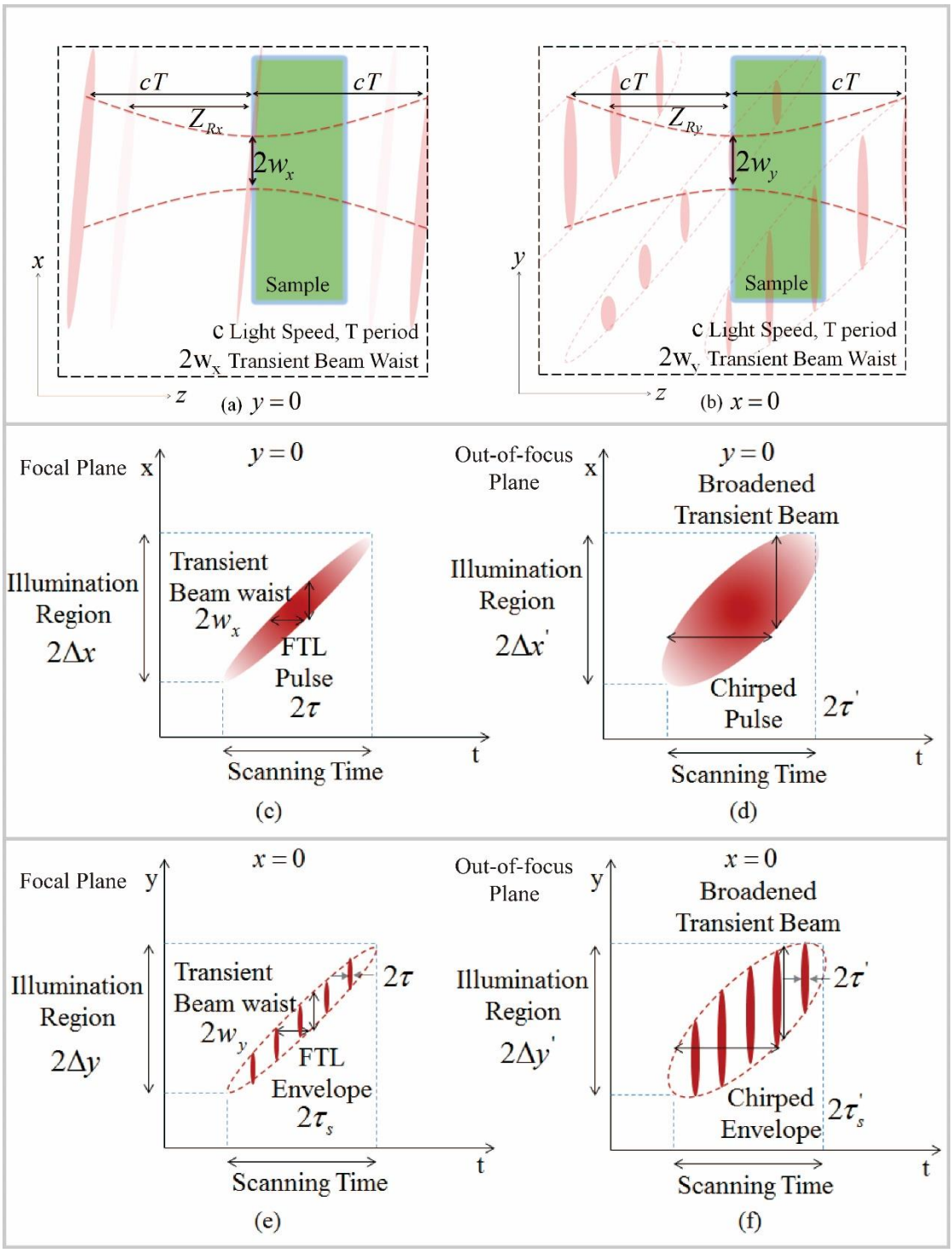

Fig. 2.3 Spatiotemporal profile of 2D-TF: (a) cross section of pulse around focal plane at y=0; (b) cross section of pule around focal plane at x=0; (c) spatiotemporal profile of single pulse in (a) at focal plane and (d) out-of-focus plane; (e) spatiotemporal profile of one-cycle envelope pulse in (b) at focal plane and (f) out-of-focus plane.

From Eq. (2.5), we know that the stretched pulse width in Eq. (2.6) is

$$\tau' = \frac{2}{\Omega'}\sqrt{1+\beta_x^2\Omega'^4}$$
$$\tau_s' = \frac{2}{\Omega_s'}\sqrt{1+\beta_y^2\Omega_s'^4}, \quad (2.7)$$

where $\beta_x = \frac{zk\gamma_x^2}{2}(1-\frac{z}{R_x(z)})$ and $\beta_y = \frac{zk\gamma_y^2}{2}(1-\frac{z}{R_y(z)})$ are the dispersion terms in Eq. (2.5). By substituting the relationships in Eqs. (2.4) and (2.5), Eq. (2.7) becomes

$$\tau' = \frac{2\Delta x}{\Omega\Delta x''}\sqrt{1+(z/z_{Rx})^2}$$
$$\tau_s' = \frac{2\Delta y}{\Omega_s\Delta y''}\sqrt{1+(z/z_{Ry})^2}, \quad (2.8)$$

where $z_{Rx} = \lambda_c / \pi(\theta_{x0}{}^2 + \theta_{mx}^2)$ and $z_{Ry} = \lambda_c / \pi(\theta_{y0}{}^2 + \theta_{my}^2)$. Since the TPE intensity is inversely proportional to the product of the pulse duration and the illumination region, I can write it as

$$I_{TPE}(z) = \int_{-\infty}^{\infty}\int_{-\infty}^{\infty}\int_{-\infty}^{\infty}|e(x,y,t,z)|^4 dxdydt$$
$$= I_0 \frac{\Delta x}{\Delta x''}\frac{\tau}{\tau'}\frac{\Delta y}{\Delta y''}\frac{\tau_s}{\tau_s'} \quad . (2.9)$$

By substituting $\tau = \frac{2}{\Omega}$, $\tau_s = \frac{2}{\Omega_s}$ and Eq. (2.8) into Eq. (2.9), Eq. (2.8) becomes

$$I_{TPE}(z) = \int_{-\infty}^{\infty}\int_{-\infty}^{\infty}\int_{-\infty}^{\infty}|e(x,y,t,z)|^4 dxdydt = I_0 / \left[\sqrt{1+(z/z_{Rx})^2}\sqrt{1+(z/z_{Ry})^2}\right], \quad (2.10)$$

where I_0 is the TPE intensity at focal plane. The FWHM of $I_{TPE}(z)$ is $\sqrt{3}$ times narrower than 1D-TF whose TPE intensity distribution is $1/\sqrt{1+(z/z_{Rx})^2}$ if I set z_{Rx}=z_{Ry}. As Eq. (2.6) shows, the effective beam divergence for the Rayleigh length of 2D-TF is a convolution between the dispersion angle, θ_x and θ_y in Eq. (2.5) and the beam divergence

of each frequency, θ_{mx} and θ_{my} in Eq. (2.4). For the microscopy application with a wide-field, the dispersion angle is much bigger than the beam divergence of each frequency. I can simply use the dispersion angle as the effective NA to evaluate the sectioning ability. For the fs-laser processing application with a spot, I can rewrite Eq. (2.10) as,

$$I_{TPE}(z) = \Big/ \left[\sqrt{1+\beta_{BAx}^4 (z / z_{mx})^2} \sqrt{1+\beta_{BAy}^4 (z / z_{my})^2} \right], \quad (2.11)$$

where $\beta_{BAx}^2 = \dfrac{\theta_x^{\,2} + \theta_{mx}^2}{\theta_{mx}^2}$ and $\beta_{BAy}^2 = \dfrac{\theta_y^{\,2} + \theta_{my}^2}{\theta_{my}^2}$.

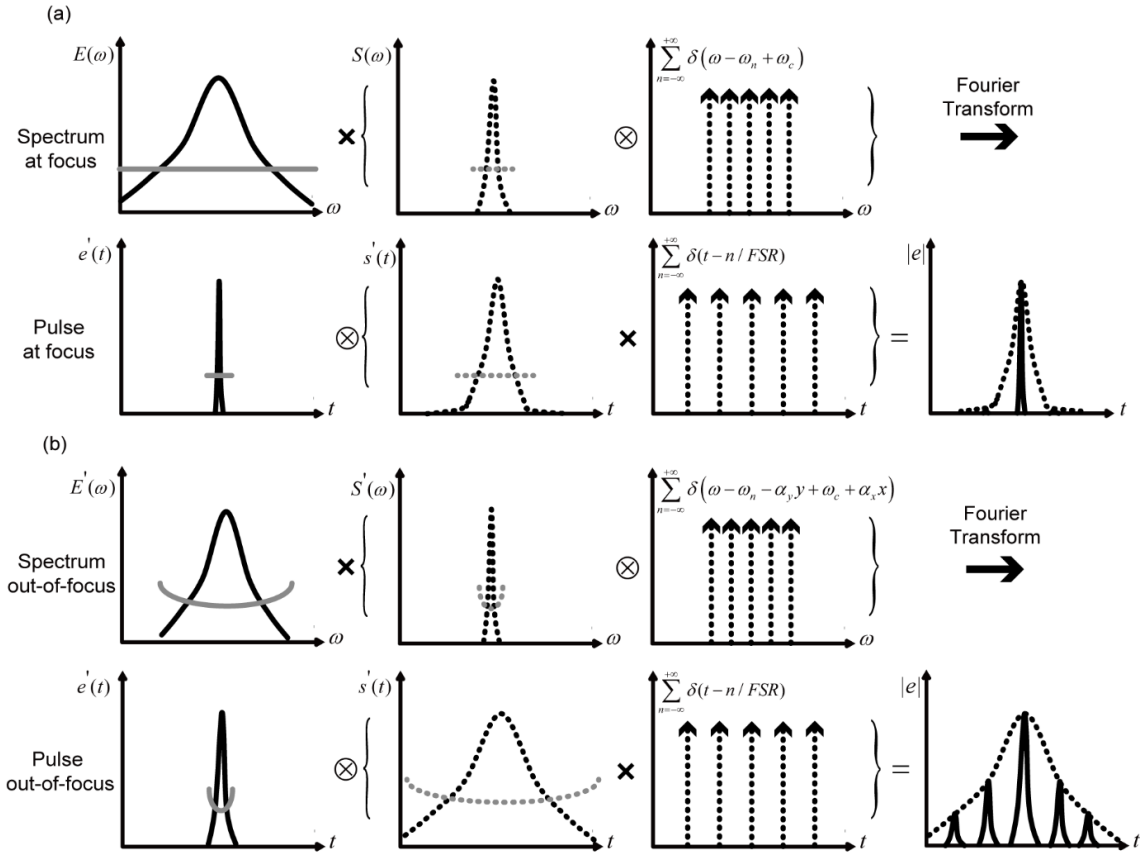

Fig. 2.4 Schematic derivation of the local pulse profile from the local spectrum and local spectrum phase at focus (a) and out-of-focus (b). Solid black line represents the amplitudes of the train pulse and its spectrum, solid gray line represents the phase of the train pulse, dotted black line represents the amplitudes of the pulse train envelope and its spectrum, dotted gray line represents the phases of the pulse train envelope.[1]

In Eq. (2.11), I find out the improvement of the axial confinement ability compared with the spatial focusing by factors of β_{BAx} and β_{BAy} in *x* and *y* directions. β_{BAx} and β_{BAy} are the spatial chirp beam aspect ratios. Compared with 1D-TF case, the improvement effect occurs in two dimensions and further enhances the axial confinement ability. Spatial chirp bream aspect ratios $\beta_{BAx} \approx \theta_{x0} / \theta_{mx} |_{\theta_{x0} >> \theta_{mx}}$ and $\beta_{BAy} \approx \theta_{y0} / \theta_{my} |_{\theta_{y0} >> \theta_{my}}$ are also the ratio between the bandwidth and the spectrum resolution in angle for the grating and the VIPA, respectively. Therefore, these aspect ratios determine the maximum stretching ratio of the train pulse and the pulse train envelope. Once the pulse approaches its maximum pulse duration, broadening of entire illumination region $\Delta x''$ and $\Delta y''$ mainly contributes to the axial excitation confinement ability.

2.2 VIPA-based 2D-TF

In this part, I further discuss the influence of FSR on temporal profile and then out-of-focus excitation level of 2D-TF. In analogy to multiline TF technique which parallelly implant multiple line focused TF, the out-of-focus temporal interference has the problem to prevent the spreading of TPE intensity. In order to reduce this effect, I find small FSR in 2D disperser is better. Thus, I choose VIPA whose FSR is 50 GHz to build up the 2D-TF setup.

2.2.1 Influence of free spectral range

In Eq. (2.6), I ignore the interference among intra pulses in order to get a closed-form solution. However, for a pulse train, this interference may generate temporal self-imaging effect so that it limits the intra pulses stretching and increases the out-of-focus multiphoton excitation. Approximately the FTL intra pulse will be recovered along z position when the dispersion term with a sampling frequency of $2\pi \mathrm{FSR}$ in Eq. (2.5) becomes a flat phase as

$$\frac{zk\theta_x^2(2\pi FSR)}{2}\left(1-\frac{z}{R_x(z)}\right)=2m\pi,\ m=\pm1,\pm2,\pm3... \quad (2.12)$$

In order to reduce this effect, I have to increase the temporal period, $1/FSR$ between intra pulses. For a practical microscopy application, I evaluate the influence of FSR by a numerical calculation. The calculation follows the analytical approach described in section 2.1. In this calculation, illumination field is 45 μm by 45 μm, pulse duration is 90 fs at focal plane and central wavelength is 805 nm. The 2D matrix of dispersed light is slightly truncated by the objective lens in order to tradeoff between input power and axial resolution. The dispersion angle is maintained same for cases of different FSR.

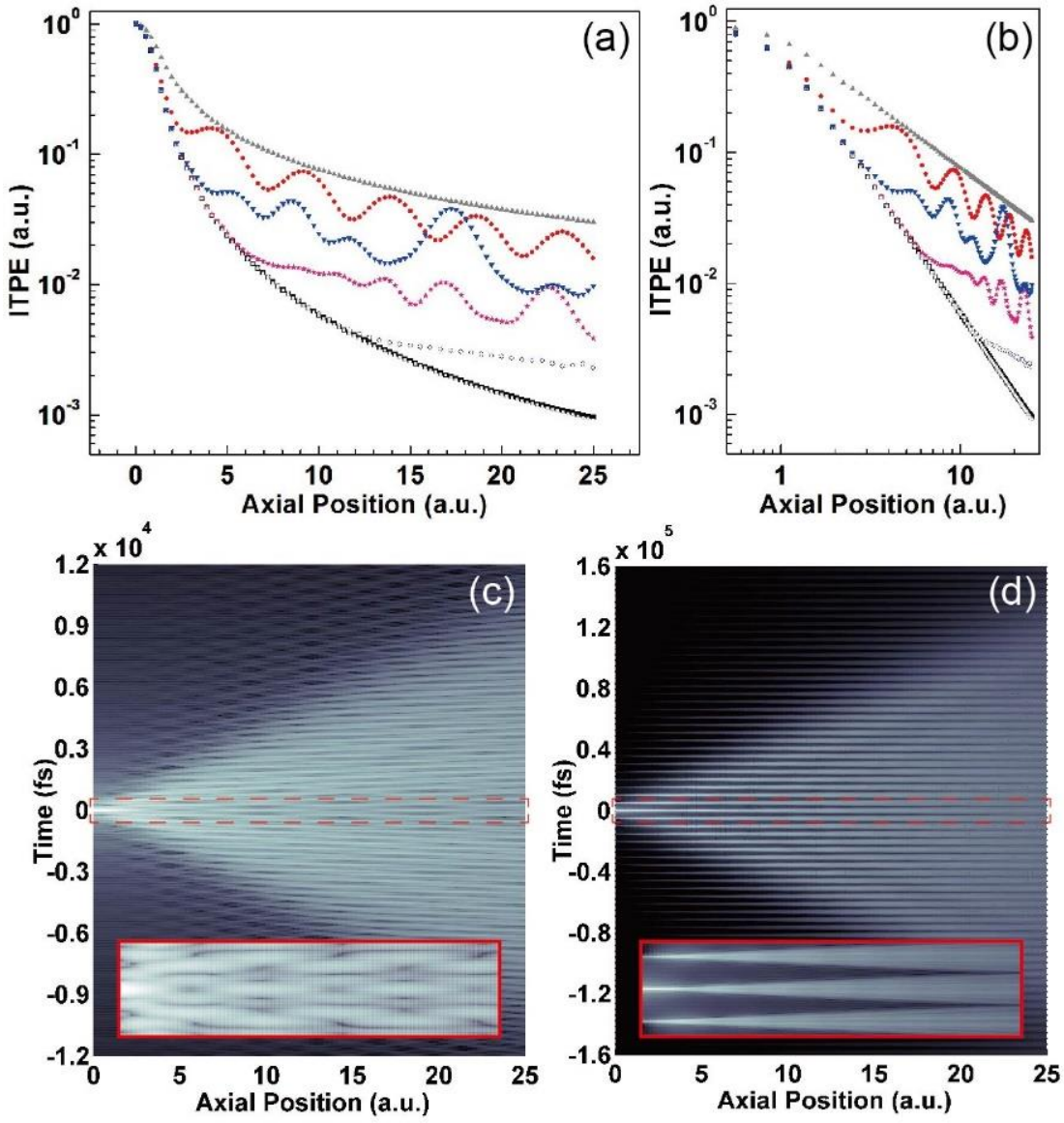

Fig. 2.5 (a): The TPE intensity along axial direction for 1D-TF (gray up triangle), 2D-TF with FSR of 3140 GHz (red solid round), 1570 GHz (blue down triangle), 785 GHz (pink star), 393 GHz (royal hollow round), 196 GHz (black solid square) and Eq. (2.7) (light gray

hollow square); (b): The log-log plot of (a); (c)-(d): The temporal profile along axial direction for FSR of 3140 GHz (c) and 196 GHz (d), color bar is in log unit, the inset figure shows the details of the central part.[1]

The results are shown in Fig. 2.5. For these results, the axial position value is scalable by the axial resolution. Therefore, we normalized it by the half width at the 2D STF's TPE intensity for making a general discussion. The axial position is divided by the sectioning resolution for a general discussion. In Fig. 2.5(a), I find out that for a usual Echelle grating with a FSR of 3140 GHz, the out-of-focus TPE intensity increase periodically. Once I decrease FSR down to 196 GHz, the background intensity is reduced more than 1 order of magnitude and is close to Eq. (2.10). In Fig. 2.5(c), we see the periodical temporal profile with FSR of 3140 GHz which illustrate the temporal self-focusing effect of 2D-TF. The period is the same as the period of TPE intensity fluctuation. However, in Fig. 2.5(d), the stretched intra pulses have no interference with FSR of 196 GHz due to the large delay between them. In Fig. 2.5(b), it shows that for a certain FSR, from a certain axial position, the TPE intensity starts to be proportional to $1/z$ instead of $1/z^2$. And the certain axial position is roughly proportional to FSR. So in order to get the TPE intensity profile as Eq. (2.10) with the axial resolution ~ 1 μm and the excitation depth ~ 100 μm, this numerical calculation suggest us to use a device with FSR ~ 50 GHz. And by this setting, I will reduce the background intensity by 2 order of magnitude. So I choose the VIPA which has an extreme small FSR to design our TF setup.

2.2.2 VIPA based 2D disperser for 2D-TF

For the spectrometer using grating, it has limited spectrum resolution. In order to realize a high spectrum resolution, people invent 2D disperser[2–5,7,8]. The idea is to first use a device functioning as a high order grating to give a very large spatial dispersing angle. The spectrum resolution is highly increased however the FSR of the device is limited to a narrow bandwidth. In order to further separate the spectrum which spatially overlap, people further orthogonally disperse the light by a grating. For Astronomy applications, people choose Echelle grating as the high order grating[9]. Echelle grating has large grove pitch which is bigger than wavelength and operate at a big blaze angle which is good to make a

compact spectrometer. For the application to resolve fs frequency combs, people need even higher spectrum resolution and people use VIPA. For VIPA (Fig. 2.6 (a)), the laser beam is first focused with a cylindrical lens onto the entrance window of VIPA. Inside VIPA, the laser beam reflects multiple times back and forth and thus forms a multiple delayed beam array. The large delay between multiple beams increase the diffraction order. So it offers a very small FSR and a high spectral resolution. Both VIPA and Echelle grating can be analyzed by the spatial interference between multiple beams. Fig. 2.6 (b) shows a typical setup of 2D disperser to resolve frequency combs. In details, the VIPA is a tilted Fabry–Perot etalon with almost 100% reflectance in the front surface and 94% reflectance in the back surface. An input beam is focused at the transparent entrance window of the VIPA. There are multiple reflections back and forth inside the VIPA along y direction. The leaked light at the back surface of the VIPA diffract with extreme big angular dispersion, $\frac{d\theta_\lambda}{d\lambda} \approx \frac{n_r^{\,2}}{\lambda_c \theta_{airinput}}$. Here $\theta_{airinput}$ is the incident angle for the VIPA in air, and n_r is the refractive index of fused silica. After collimated by a cylindrical mirror in y direction, different diffraction orders overlap together in the Fourier plane, and the spatial amplitude envelope corresponds to an optical Fourier transform of the beam profile at the entrance. To form a 2D spectral disperser, I need to separate different diffraction orders generated by VIPA by another spectral disperser with a small angular dispersion in the orthogonal direction where the light is dispersed by a grating and then collimated by a cylindrical lens. I set the focal length of the two collimating lenses (mirror) so that the Fourier planes in two lateral direction share the same plane. In history this 2D disperser is widely used in optical communication and spectroscopy field. It has been used for wavelength de-multiplexing, 2D pulse shaper, and frequency-comb spectroscopy. People also use the spatial and spectrum mapping property of 2D disperser to make a fast camera. It encodes the spatial information into spectrum and then use chirped pulse to transform the spectrum information into time domain and finally measure the temporal profile with fast detector.

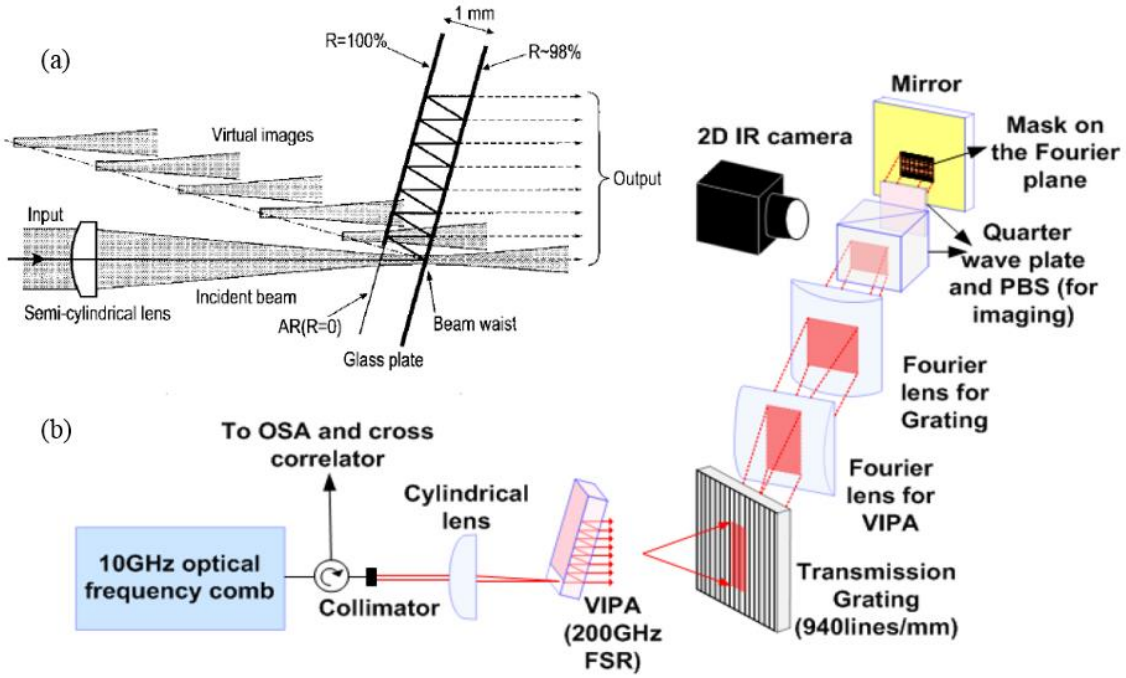

Fig. 2.6 (a) schematic of VIPA[7] (b) 2D disperser to resolve optical combs[3]

I use VIPA based 2D disperser to create 2D spectrum matrix first at Fourier plane and then spatially and temporally recombine this spectrum matrix at focal plane similar to a conventional TF. Fig 2.7 shows the proposed 2D-TF TPEF microscopy.

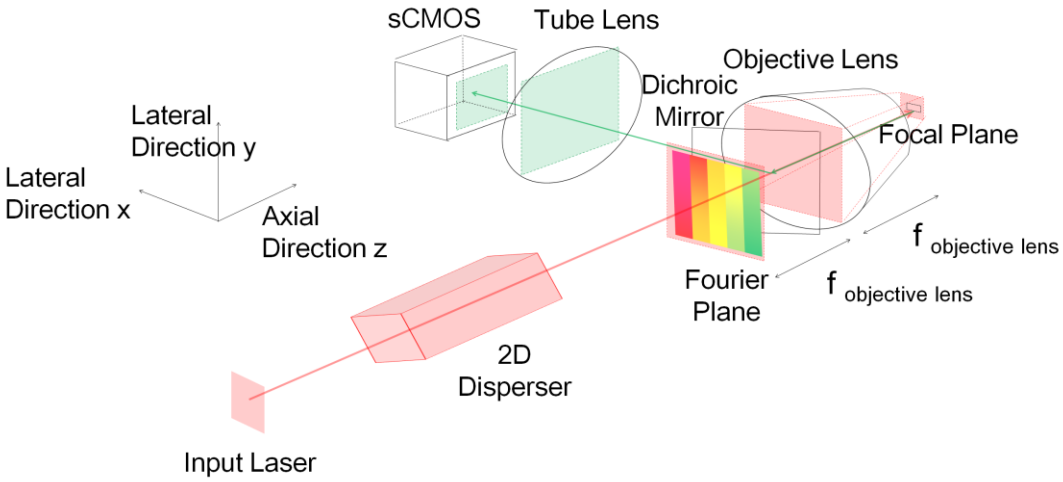

Fig 2.7 Proposed setup of 2D-TF microscopy

2.3 Experiment to verify the improvement of sectioning ability

2.3.1 Experimental setup

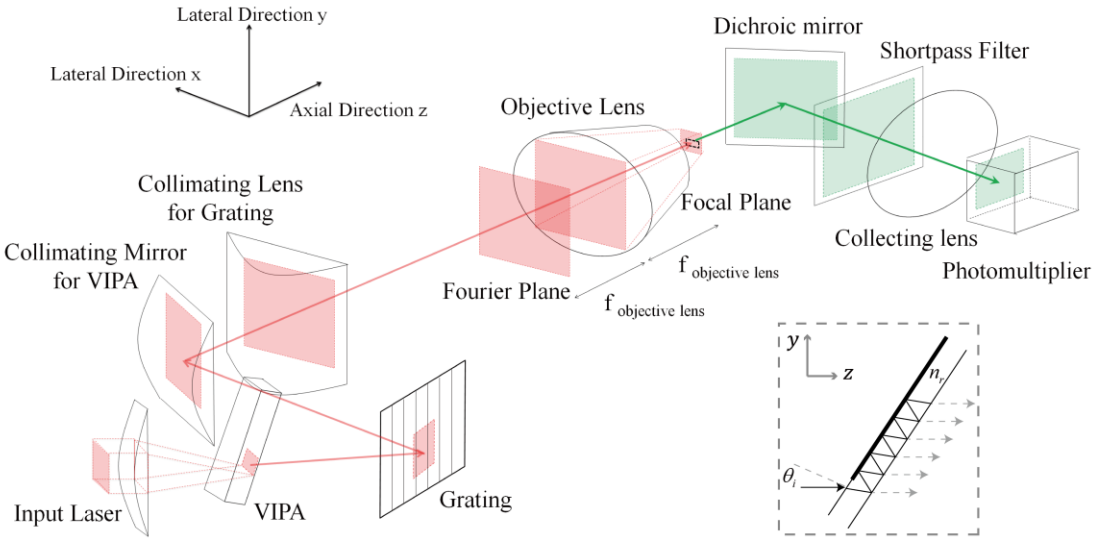

Fig. 2.8 The setup of 2D-TF for proof-of-principle experiment. The insert shows magnified VIPA device[10].

Fig. 2.8 shows the setup of 2D-TF in this section. The FSR of the VIPA is 50 GHz, which corresponds to a 2-mm thickness and a refractive index of 1.5. I put the dispersing directions of the grating and the VIPA orthogonal to each other as the cross-disperser. The groove number of the grating is 150 1/mm, the input angle for the VIPA in air is set as 0.1 rad and the input beam radius is 128 μm. The focal length of the collimating optics for the grating and the VIPA are 400 mm and 500 mm. With this design, the dispersion angles, θ_x and θ_y are 0.22 rad and 0.25 rad. In this experiment, the back aperture of the objective lens is under-filled because I want to produce a situation with a Gaussian distribution for spectrum and beam profile, as assumed in Eq. (2.1). I use a chirped pulse amplification (CPA) laser source with central wavelength of 803 nm, a pulse duration about 50 fs, and a repetition rate of 1 kHz.

For the measurements, I scan a KTA crystal surface around the focal plane by a piezo motor stage. The KTA crystal is mounted on the piezo stage and its front surface is perpendicular to the optical axis. During the measurements, I record the SHG intensity

generated by the KTA crystal at each axial position of the front surface of the KTA crystal. The step size of the movement of the KTA crystal is 1.2 μm in axial direction. Since the phase matching condition for the bulk SHG is not satisfied because SHG is not expected for bulk materials with centrosymmetric, only surface SHG signal, which is proportional to the TPE intensity at the crystal surface, is generated. I collect the SHG signal in the forward direction by a collimating lens with a dichromic mirror and a low-pass filter to remove the illumination light. The collected light is detected by a photon multiplier tube and measured with a lock-in detector. The frequency of the lock-in-detector is set the same as the repetition rate of the CPA laser to demodulate the signal and remove noise.

2.3.2 Sectioning resolution

I first separately measure the TPE intensity for 1D-TF with only the grating or the VIPA. For 1D-TF with the grating, I remove the VIPA and the cylindrical collimating lens in front of the VIPA. For 1D-TF with the VIPA, I tune the grating to the zero diffraction order. As Fig. 2.9 shows, by fitting the results with the square root of the Lorentz-Cauchy function, I measure the Rayleigh length z_{Rx} and z_{Ry} as 4.8 μm and 4.1 μm, which correspond to dispersion angles of 0.23 and 0.25 rad. It satisfies our design. Then I measure the axial confinement ability of 2D-TF. The results agree well with the prediction from Eq. (2.10).

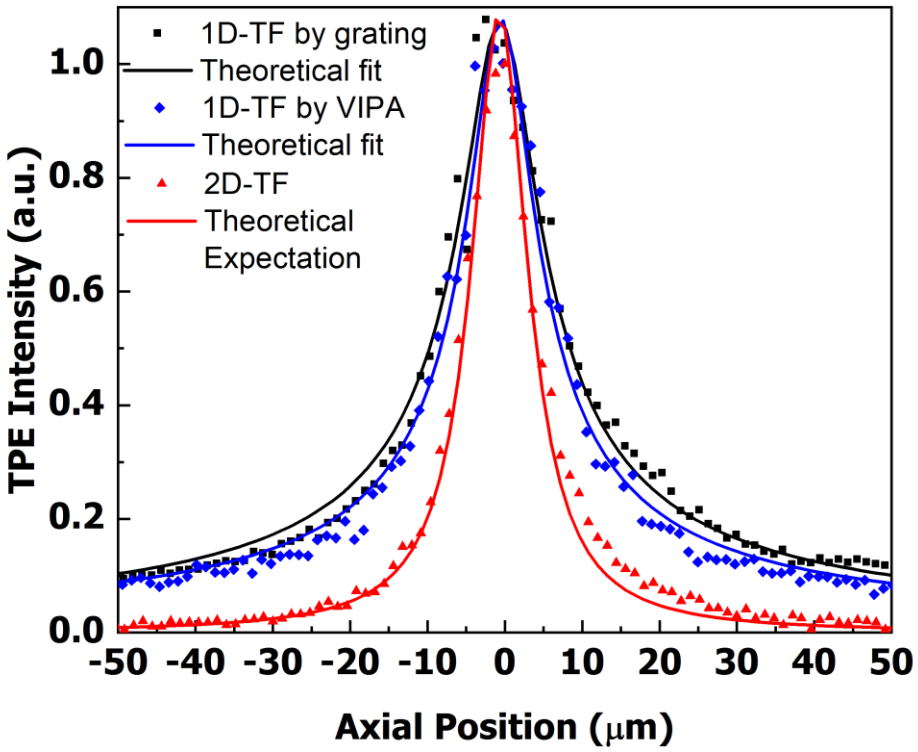

Fig. 2.9 The TPE intensity along axial direction for 2D-TF[1]

2.3.3 Decay speed of the out-of-focus excitation

I also checked the out-of-focus background, which is the TPE intensity in the out-of-focus region. This time, I looked at how it changed along the axial direction in the log unit shown in Fig. 2.10 by re-plotting the TPE intensity in the out-of-focus region shown in Fig. 2.9. By linear fitting, I obtained a slope of -1 for the 1D-TF by either grating or VIPA. For the 2D-TF, the slope was -2. This means that, for the 1D-TF case, the out-of-focus background is proportional to 1/z, but for the 2D-TF case, it is proportional to $(1/z)^2$. This verified the notion of the out-of-focus background expressed in Eqs. (2.10) by taking the limit for $z >> Z_{Rx}$, Z_{Ry} and, moreover, proved the fundamental difference between 1D-TF and 2D-TF. In 2D-TF, the VIPA not only generates a multiline pattern but also gives a different phase for each line and thus reduces the cross talk between neighboring lines as

well as disperses the light as high-order grating. I experimentally achieved around one order of magnitude improvement in the suppression of the out-of-focus background.

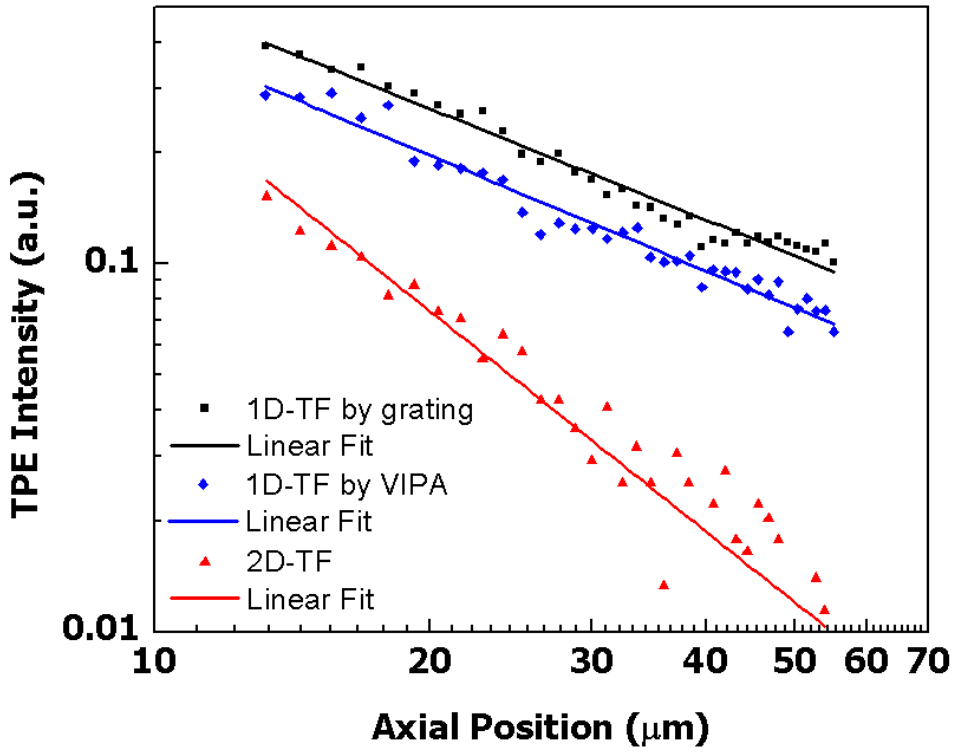

Fig. 2.10 log-log plot of out-of-focus TPE intensity, the axial position is divided by the 2D-TF's FWHM in Fig. 2.9[1]

2.4 Experiment to verify the improvement of imaging performance

2.4.1 Experimental setup

In order to further address the importance to reduce out-of-focus TPE intensity, I build up an epifluorescence microscope as Fig. 2.11 shows. The order of grating and VIPA is reversed in order to increase the input laser intensity without damaging the VIPA surface. The line focused beam in the front surface of VIPA is first spatially chirped by the grating thus the chance for multi-photon effect at the front surface of VIPA is reduced. The focal length of the collimating optics for the grating and the VIPA are 1000 mm and 400 mm to

fulfill the back aperture of the objective lens with the 2D matrix of dispersed light. I use an objective lens with NA of 1.2 (UPLSAPO 60XW, Olympus) to evaluate the sectioning ability. With this design, the dispersion angles, θ_x and θ_y are around 0.75 and the back aperture of the objective lens will cut the tail of the spectrum matrix. I use another objective lens with NA of 0.95 (UPLSAPO 40X2, Olympus) for the imaging experiment. I replace the photomultiplier by a camera in this section. To evaluate the sectioning ability, I use a scientific CMOS (sCMOS) camera (Zyla 5.5). For the imaging experiment, I use a cooled CCD camera (BS42).

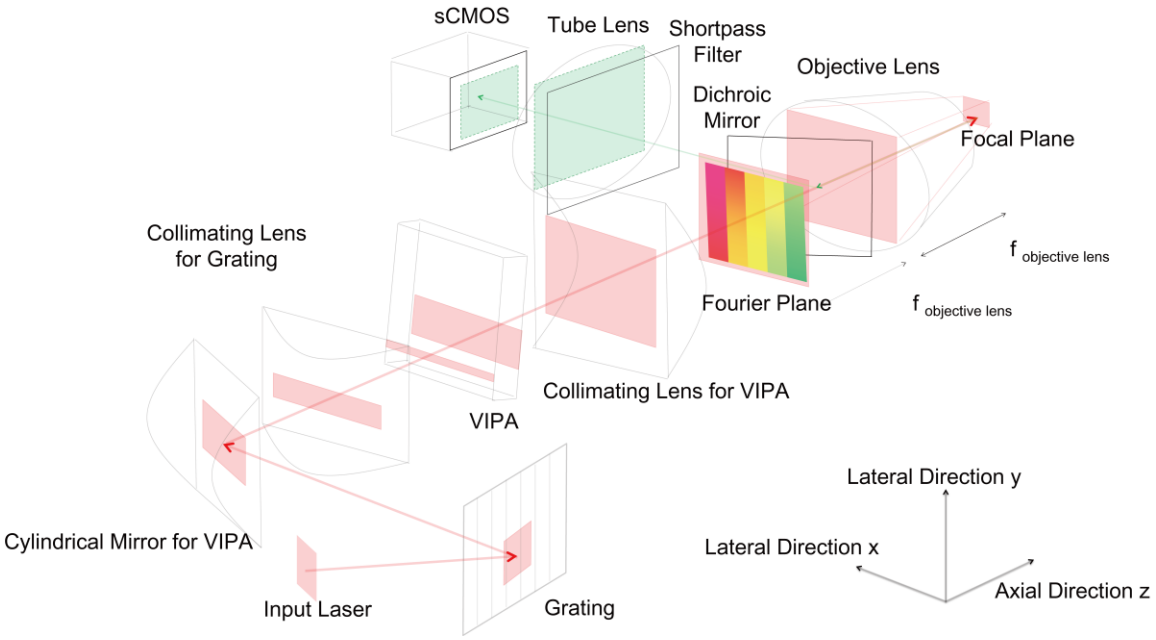

Fig 2.11 Setup of 2D-TF TPEF microscopy

2.4.2 Sectioning resolution in 2D-TF microscopy

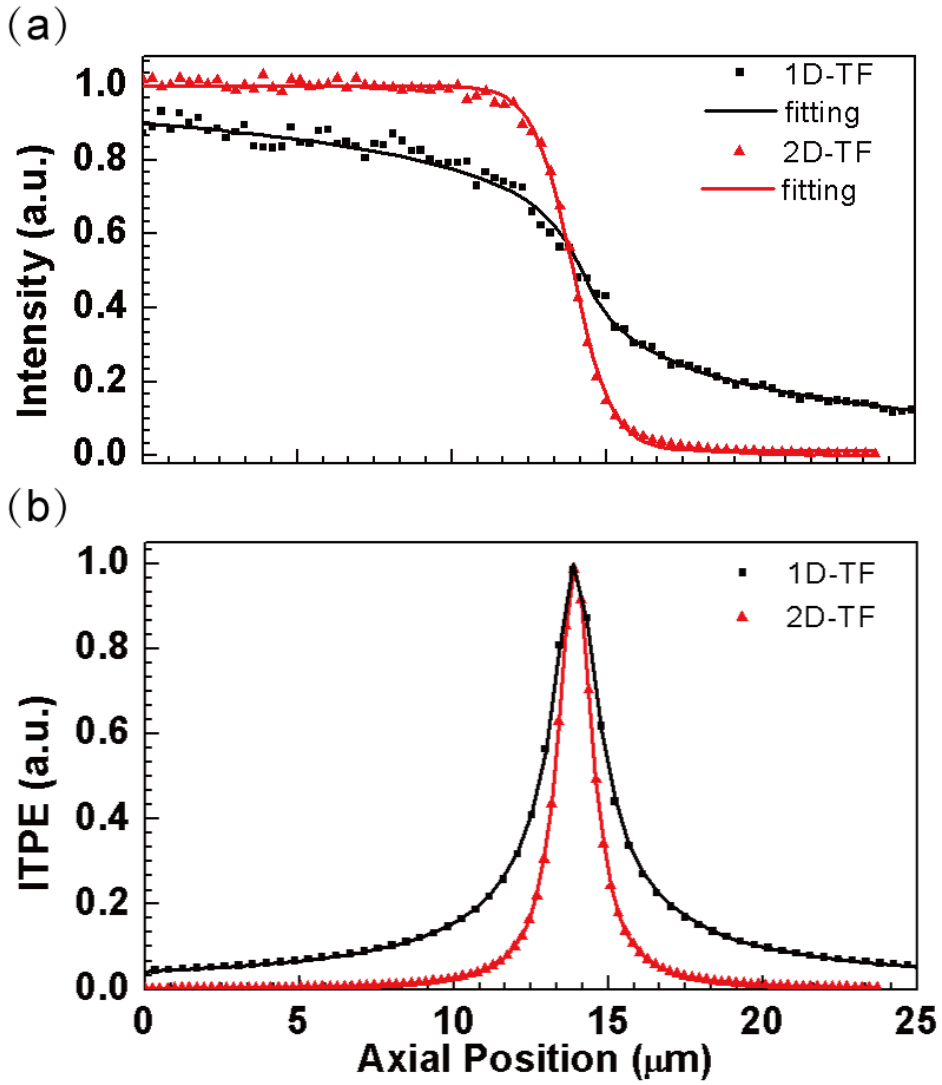

Fig. 2.12 (a): The fluorescence intensity for scanning; (b): The first derivatives of fitting results in (a).[1]

The sectioning resolution is measured by scanning Rhodamin B solution around the interface between the solution and the cover glass. The integration time of the camera is 0.1 sec. I sum up the fluorescence signal on the camera at each axial position and Fig. 2.12 shows the measured sectioning resolution of 1.3 μm and 2.2 μm for 2D-TF and 1D-TF with grating. I conclude that 2D-TF has 1.7 times improvement of sectioning resolution compared to 1D-TF.

2.4.3 Reduction of background fluorescence in 2D-TF microscopy

Then I prepare the tissue-like phantom with 2-μm-diameter yellow green (505/515) polystyrene fluorescent beads. The beads are fixed with agarose gel and the beads concentration is 4.5×10^{-4} spheres per cubic micron. The mean-free-path length is around 80 μm. I scan sample axially with a step of 0.6 μm by a motor to get the sectioned image with a 20-μm-by-15-μm field of view. The intensity of the illumination light decreases along the penetration depth. To compensate the loss at the focal plane, I increase the laser power gradually. Thus the out-of-focus excited fluorescence increases relatively so as to decrease the contrast of the image. Figure 2.13 shows the bright beads at their focal plane with different depth. Around the surface, at the depth of 18 μm, I have the similar contrast for 1D-TF and 2D-TF microscope. However, when I penetrate deeper, at the depth of 69 μm, 2D-TF microscope has higher contrast due to less background fluorescence.

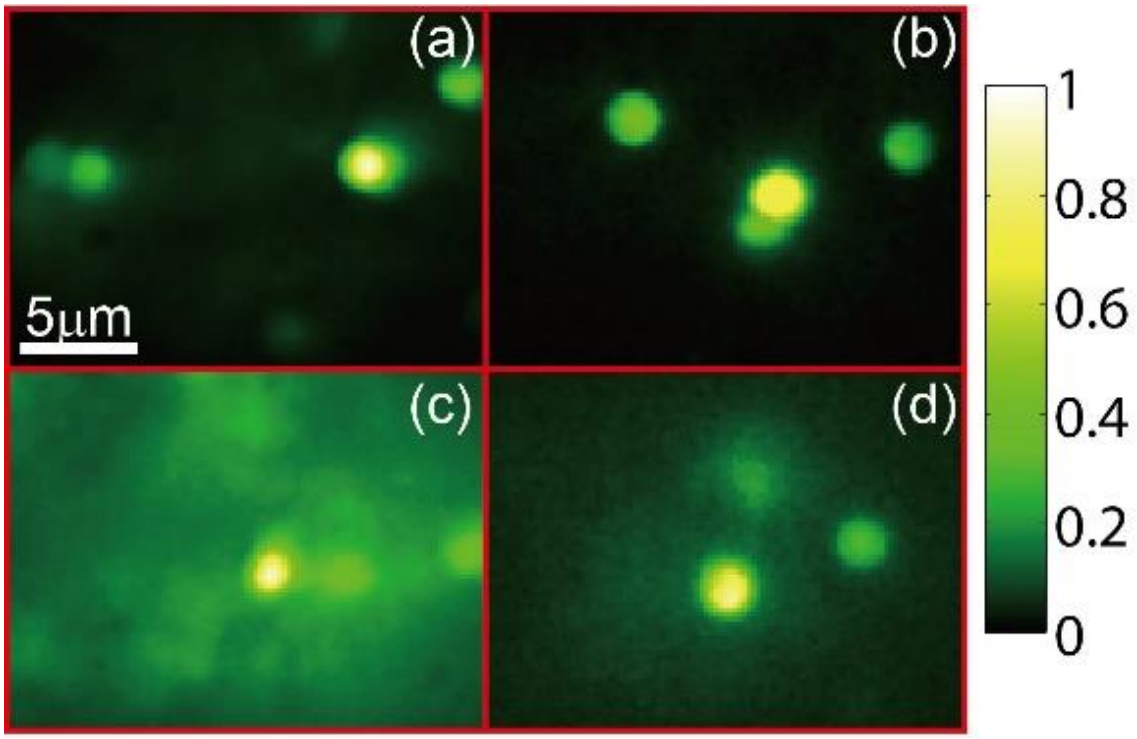

Fig. 2.13 (a)-(b): The fluorescence image of 1D-TF microscope (a) and 2D-TF microscope (b) at the depth of 18 μm; (c)-(d): The fluorescence image of 1D-TF microscope (c) and 2D-TF microscope (d) at the depth of 69 μm. [1]

2.5 Experiment to demonstrate high speed 3D volumetric imaging

2.5.1 Experimental condition

In this section, I will show the application of 2D-TF via fast 3D volumetric TPEF imaging. In the microscopy setup, it is same as Fig 2.11 shows. The objective lens is UPLSAPO 60XW (Olympus) with NA of 1.2. I also integrate a closed-loop piezo stage and a scientific CMOS (sCMOS) camera for the imaging system in order to achieve fast scanning in *z* direction and 2D single shot imaging. Limited by the acquisition time of sCMOS camera, the imaging region is set as 128 by 216 pixels for every single shot imaging with a frame rate of 1 kHz. By scanning in *z* direction with applied voltage to piezo stage, I capture a volume image of 17.8 μm by 10.6 μm by 5.4 μm (z) at 50 volumes per second. The applied voltage is 50-Hz asymmetric triangular signal. The image is continuously acquired in sCMOS at a frame rate of 1 kHz and saved after 3-sec recording. Then 10 planar images in each axial scanning cycle is selected to build up one 3D volumetric imaging. The relative axial position of the 10 planar image is calculated from the slope of the input triangular signal for piezo stage.

Regarding the imaging size, in principle, I assume that the dispersion free plane of 2D-TF is perpendicular to the propagation direction (z). In the practical case of VIPA, since the virtually imaged plane is tilted, I should choose a de-magnification ratio between the collimating optics and the objective lens to guarantee that the axial shift is less than the axial resolution. For example, to achieve a 100-μm by 100-μm field of view with a Rayleigh length of 0.35 μm, I should set the de-magnification ratio to around 1000. By integrating this setting with the CPA laser, a sCMOS, and a piezo stage, fast volume imaging around 100 μm by 100 μm is available.

2.5.2 Volumetric imaging of 3D Brownian motion

As a demonstration, I trace the Brownian motion of a 1 μm fluorescent bead. When there are lots of beads close to each other, a displacement less than the radius of bead is necessary to discriminate the target bead from neighbor beads during movement. Otherwise, I will

confuse with many possible trajectories. In order to realize this, the root mean square (RMS) displacement of movement between neighbor frames should be less than the radius of the bead. Since the RMS displacement is proportional to $\sqrt{\Delta t}$ where $1/\Delta t$ is the volumetric imaging rate, our system which has a volume rate of 50 Hz can offer a RMS displacement around 240 nm according to the calculation. It is roughly half of the radius of the bead and is able to trace the random path of Brownian motion. Fig. 2.15 shows the measured displacements during 3 seconds. I use weighted algorithm to determine centroid with sub-pixel resolution. The 3D displacement is measured at each lateral and axial direction and then I got the measured RMS displacement as 226 nm, which matches well with the numerical calculation.

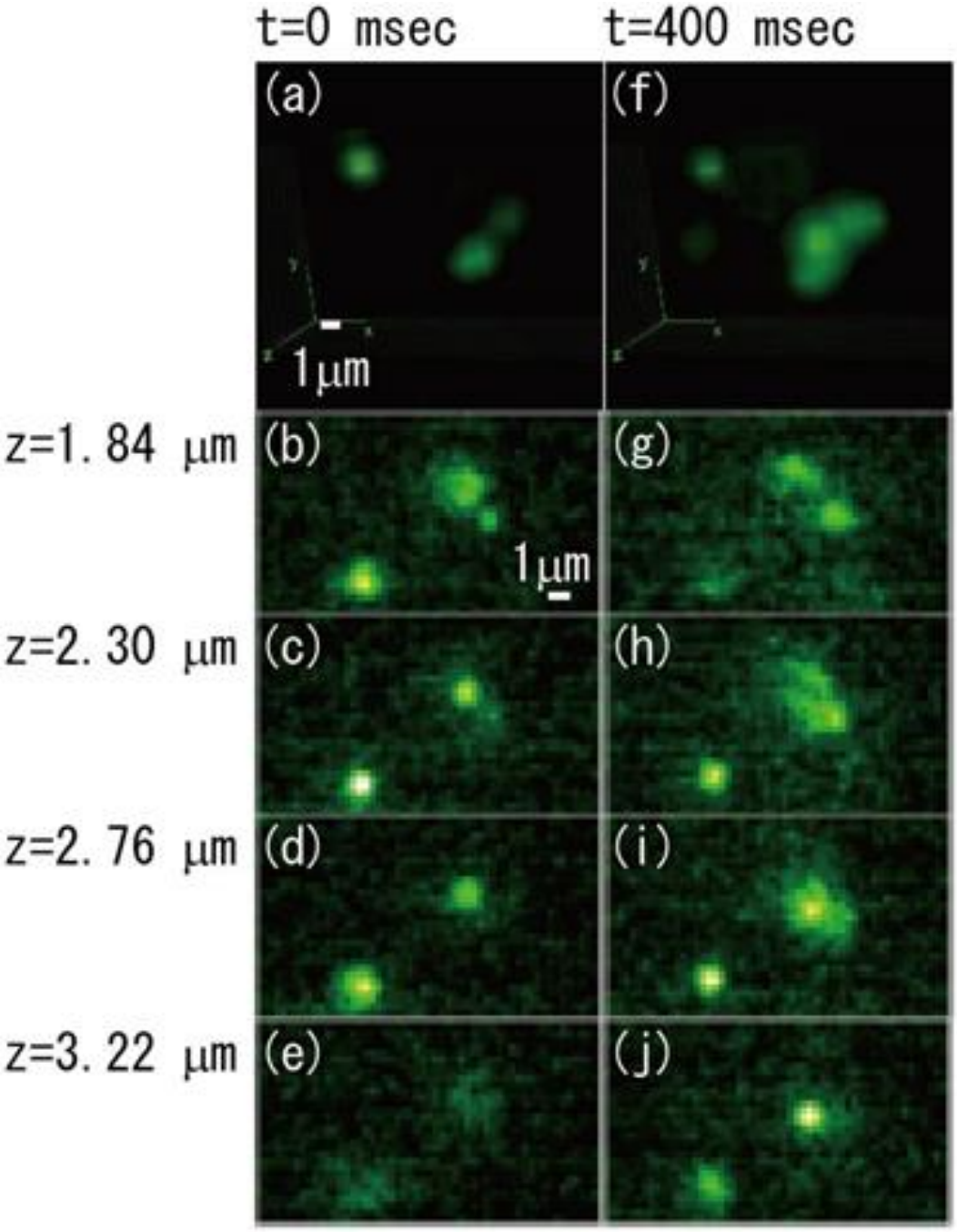

Fig. 2.14 Brownian motion: (a) volume imaging of 1μm beads at 0 msec, (b)-(e) lateral slices of volume imaging of (a) at selected axial positions, (f) volume imaging of 1μm beads at 400 msec, (g)-(j) lateral slices of (f) at selected axial positions, (k) measured 3D displacement of left upper bead in (a) over 3 sec.[11]

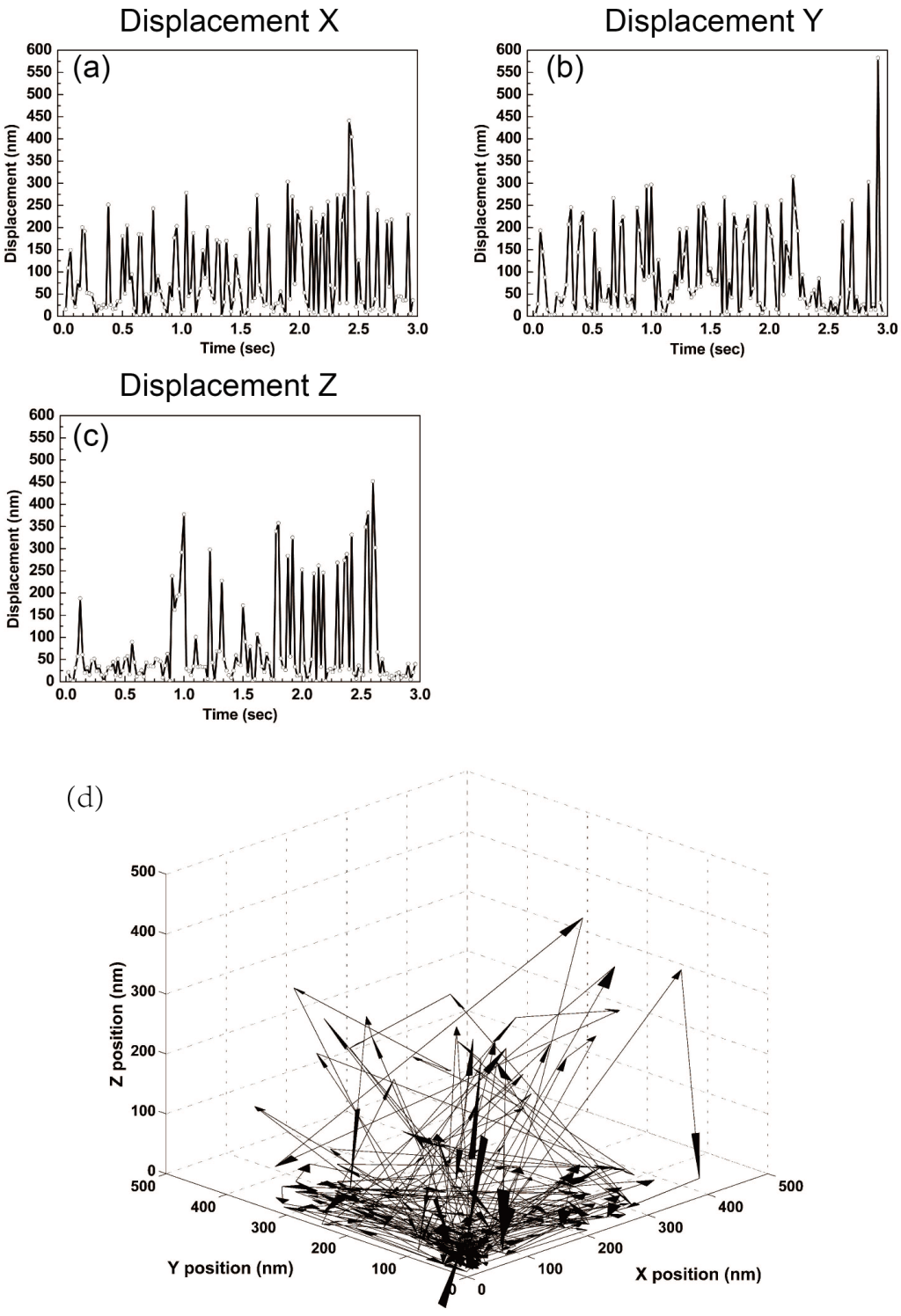

Fig. 2.15 Brownian motion measurement of the left upper bead in Fig 2.14 (a): the displacement of beads in (a) X, (b) Y and (c) Z direction; (d) the trajectory of Brownian motion[12].

2.6 Summary

I increased the axial resolution 1.7 times by 2D-TF as confirmed in section 2.4.2. And the decay speed of out-of-focus excitation is increased from 1/z to $1/z^2$ as confirmed in section 2.3.3. In simulation, I expect to reduce the out-of-focus excitation by 2 orders of magnitude compared with the 1D TF by utilizing an extremely small FSR of the VIPA as calculated in section 2.2.1 and experimentally I verified that at least 1 order of magnitude of out-of-focus excitation is reduced as confirmed in section 2.3.3. The basic idea, which generates a delay for preventing the out-of-focus interference between neighbor intra-pulses, resembles time-multiplexing multifocal multiphoton microscopy. At any out-of-focus spatial point, time-multiplexing multifocal multiphoton microscopy generates a delay so that the pulses from different foci are not interfered temporally. In time-multiplexing multifocal multiphoton microscopy, the spectrum is the same at every spatial point, and thus the pulse width is a fixed parameter. On the other hand, in 2D-TF, the spectrum is narrowing, and the dispersion is increasing out-of-focus, and thus I add spatiotemporal evolution in our analytical approach to find a suitable delay. Finally, in section 2.5.2, we demonstrated that 2D-TF can achieve single shot wide-field TPEF microscopy.

For the future prospect, in addition to the axial confinement ability, TF's widefield illumination is robust to scattering. However, 1D TF mainly smoothes the speckle along the 1D spatial chirping direction. For a 2D-TF, a 2D spatial chirp could extend this effect to 2D to offer isotropic smoothed speckles. In fs-laser processing applications, TF helps suppress nonlinear side effects, e.g., filamentation for low NA or high pulse energy cases. A 2D-TF, which further stretches the out-of-focus pulse, might increase the threshold pulse energy. Such surgical applications as the treatment of the posterior segment of the eye, where a low NA ~ 0.1 is needed, are very promising with a 2D-TF technique.

Although the sectioning ability in 2D-TF is improved compared to TF in the excitation path, the scattered emission background in emission path remains in the image of 2D-TF TPEF microscopy the same as TF. In next chapter, I will find a solution to solve the issue in emission path by introducing the structured illumination microscopy for TF.

References

1. Song, Q. *et al.* Two-dimensional spatiotemporal focusing of femtosecond pulses and its applications in microscopy. *Rev. Sci. Instrum.* **86,** (2015).

2. Xiao, S., Weiner, A. M. & Lin, C. A dispersion law for virtually-imaged phased-array spectral dispersers based on paraxial-wave theory. *Conf. Lasers Electro-Optics/International Quantum Electron. Conf. Photonic Appl. Syst. Technol.* **40,** 420–426 (2004).

3. Supradeepa, V. R., Huang, C.-B., Leaird, D. E. & Weiner, A. M. Femtosecond pulse shaping in two dimensions: Towards higher complexity optical waveforms. *Opt. Express* **16,** 11878 (2008).

4. Diddams, S. A., Hollberg, L. & Mbele, V. Molecular fingerprinting with the resolved modes of a femtosecond laser frequency comb. *Nature* **445,** 627–630 (2007).

5. Wang, S. X., Xiao, S. & Weiner, A. M. Broadband , high spectral resolution 2-D wavelength-parallel polarimeter for Dense WDM systems. **13,** 9374–9380 (2005).

6. Wang, Z. *et al.* Interferometric characterization of pulse front tilt of spatiotemporally focused femtosecond laser pulses. *Opt. Express* **22,** 26328–37 (2014).

7. Shirasaki, M. Large angular dispersion by a virtually imaged phased array and its application to a wavelength demultiplexer. *Opt. Lett.* **21,** 366 (1996).

8. Goda, K., Tsia, K. K. & Jalali, B. Serial time-encoded amplified imaging for real-time observation of fast dynamic phenomena. *Nature* **458,** 1145–9 (2009).

9. Loewen, E., Maystre, D., Popov, E. & Tsonev, L. Echelles: scalar, electromagnetic, and real-groove properties. *Appl. Opt.* **34,** 1707–27 (1995).

10. Song, Q. *et al.* Using two-dimensional spatial and temporal focusing microscopy to increase the imaging depth and decrease the photobleaching probability. in *The 3rd Advanced Lasers and Photon Sources* (2014).

11. Song, Q., Nakamura A., Hirosawa, K., Isobe, K., Midorikawa K., and Kannari, F., Two-dimensional Spatiotemporal Focusing Microscopy. *Review of Laser Engineering*, **43**, 203-207 (2015).

12. Song, Q., Isobe, K., Hirosawa, K., Midorikawa, K. & Kannari, F. 2D simultaneous spatial and temporal focusing multiphoton microscopy for fast volume imaging with improved sectioning ability. in *Progress in Biomedical Optics and Imaging - Proceedings of SPIE* **9329,** (2015).

Chapter 3

Three-dimensional interferometric temporal focusing microscopy

SIM, as a super-resolution technology can achieve comparable spatial resolution to PALM and STED with less acquisition time and less photon damage. As an extension, 3D-SIM has the true optical sectioning by filling the missing cone of the OTF and thus remove the out-of-focus signal. Also 3D-SIM doubles the spatial resolution in 3D through broadening the OTF. However, when the imaging depth increases, the wide-field illumination of 3D-SIM generates the huge amount out-of-focus fluorescent light, this light increases the background of the raw image. Due to the limited dynamic range of the camera, the out-of-focus background sacrifices the in-focus signal. Moreover, the shot noise of the background fluorescence remains in the reconstructed image. Finally, the in-focus signal to noise level will be less enough to reconstruct a decent image.

On the other hand, TF, a wide-field TPEF technique offers a field of view in several hundred micrometers square as well as confines the thickness of the excitation volume to only several micrometers. This boost up the imaging speed of TPEF microscopy. However, due to the use of longer excitation wavelength in TPE, the sectioning ability of TF is still above 1 μm even if we utilize the advanced TF technique in excitation side such as Multifocal TF or 2D-TF.

In this chapter, by combining 3D-SIM with TF, which I call 3D-ITF[1–3], I excite a sheet rather than a volume of the sample and thus can dramatically reduce the out-of-focus background in the raw image of 3D-SIM and the corresponding shot noise in the reconstructed image. Moreover, the longer excitation wavelength can reduce the scattering of the illumination light. Even the scattered excitation itself is reduced by TPE due to the enlarged temporal profile of the scattered light. For the scattering of the emission part, SIM itself can remove it by homodyne detection thus 3D-SIM combined with TF can penetrate inside the thick biology sample.

Most importantly, 3D-ITF has a super-sectioning ability for TPEF microscopy because the missing cone in emission OTF is filled and the axial cut-off frequency in the cone breaks the diffraction limitation. Fig 3.1 shows the schematic of 3D-ITF.

In section 3.1, I describe the basic principle of 3D-ITF and the method to reconstruct the image from several raw images. In section 3.2, I describe the experimental setup, the method to optimize the spectral phase of the light source and the method to produce the sample. In section 3.3, I show the experimental proof of the enhanced sectioning resolution in 3D-ITF. In section 3.4, I show the experimental proof of the super-resolution in 3D-ITF. In section 3.5, I show the ability to reduce scattered background florescence in 3D-ITF when the sample is dense and highly scattering meanwhile I show the super-resolution in 3D-ITF for such sample. In section 3.6, I give the summation of this chapter.

(a)

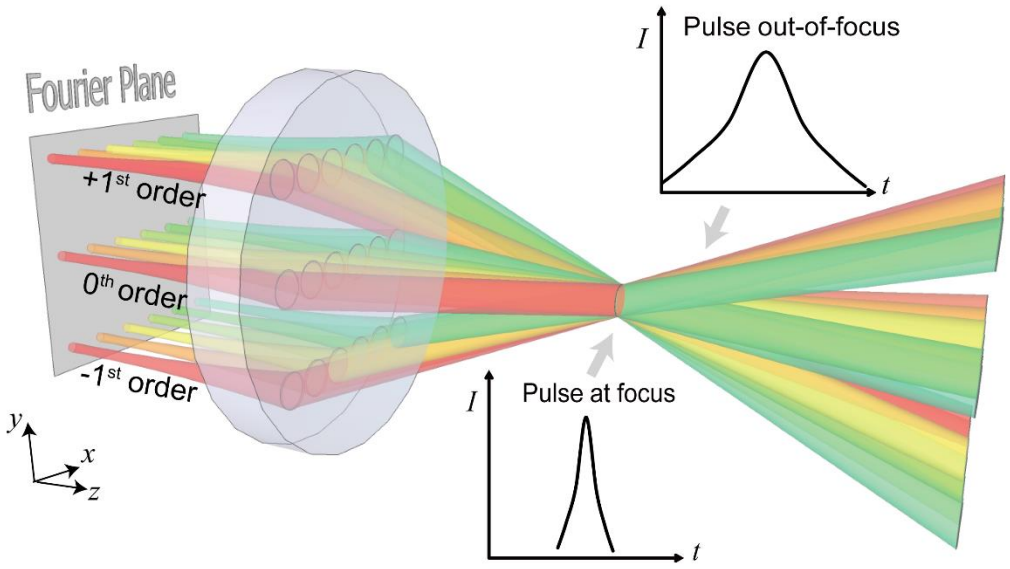

(b)

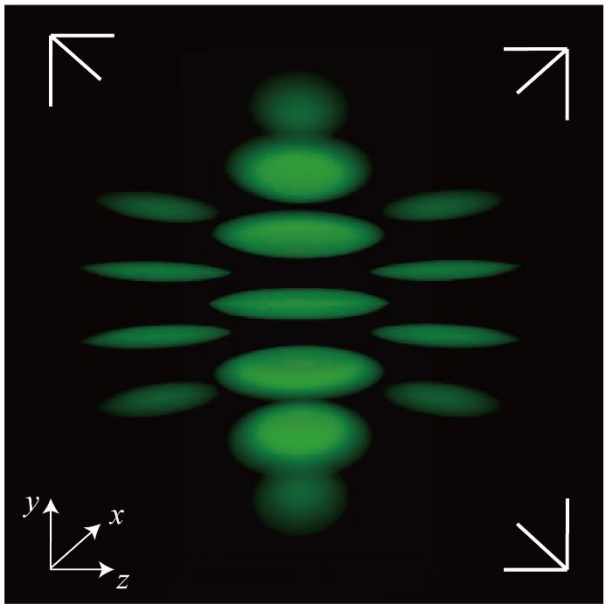

Fig 3.1 (a) Schematic of 3D-ITF, (b) magnified view of 3D-ITF illumination light around focal plane

3.1 Principle

In 3D-ITF, TPE from 3D structured illumination light is axially confined by TF effect. To realize this, I use three spatially chirped beams. As shown in Fig 3.2, a diffractive element, DMD is utilized to generate such beams. DMD consists of an array of tilted mirrors at $\pm 12^{\circ}$ and they function as a phase grating which generate the spatial chirp. In addition, I add a 2D amplitude modulation upon the phase grating by turning on or off for each micromirror. I apply a binary fringe pattern as the amplitude modulation and the fringe is relative sparse compared to the phase grating. So the pattern will further splits the spatial-chirped beam into several diffraction orders and I only select the three spatial-chirped beams in +1, 0 and -1 diffraction order to pass through the objective lens.

I collimate the three spatial-chirped beams and then collect them in an asymmetric 4f system so that the beams form an image of the DMD surface in the focal plane of the objective lens. At the focal plane all the spectrum components overlap and there is no dispersion, so the pulse duration is shortest. However, out-of-focus the spectrum components leave apart and dispersion occurs so the pulse duration is gradually broadened. This is the TF effect. This confines the TPE intensity only efficiently around the focal plane and dramatically reduce the useless out-of-focus excitation. On the other hand, around the focal plane, the central frequency component of each spatial-chirped beam has a diffraction angle of θ, 0 and $-\theta$, corresponding to +1, 0 and -1 diffraction order respectively. The interference of the three beams generate the 3D pattern and the electrical field of the 3D pattern is:

$$E(\mathbf{r}) = \alpha e^{i(\mathbf{k}_{+1}\mathbf{r}+\varphi_0)} + e^{i(\mathbf{k}_0\mathbf{r})} + \alpha e^{i(\mathbf{k}_{-1}\mathbf{r}-\varphi_0)}, \quad (3.1)$$

where the wave vector $\mathbf{k}_{+1}$, $\mathbf{k}_0$ and $\mathbf{k}_{-1}$ corresponds to the central frequency components of the three excitation beams, α is the relative amplitude of the +1 and -1 order diffraction light; φ_0 is the offset phase. I ignore all the proportional constants. Considering the TPE effect, the TPE intensity of the 3D pattern is

$$I_{TPE}(\mathbf{r}) = |E(\mathbf{r})|^4 = \sum_{m=-4}^{+4} I_m(z) J_m(\mathbf{r}_{xy}) . \quad (3.2)$$

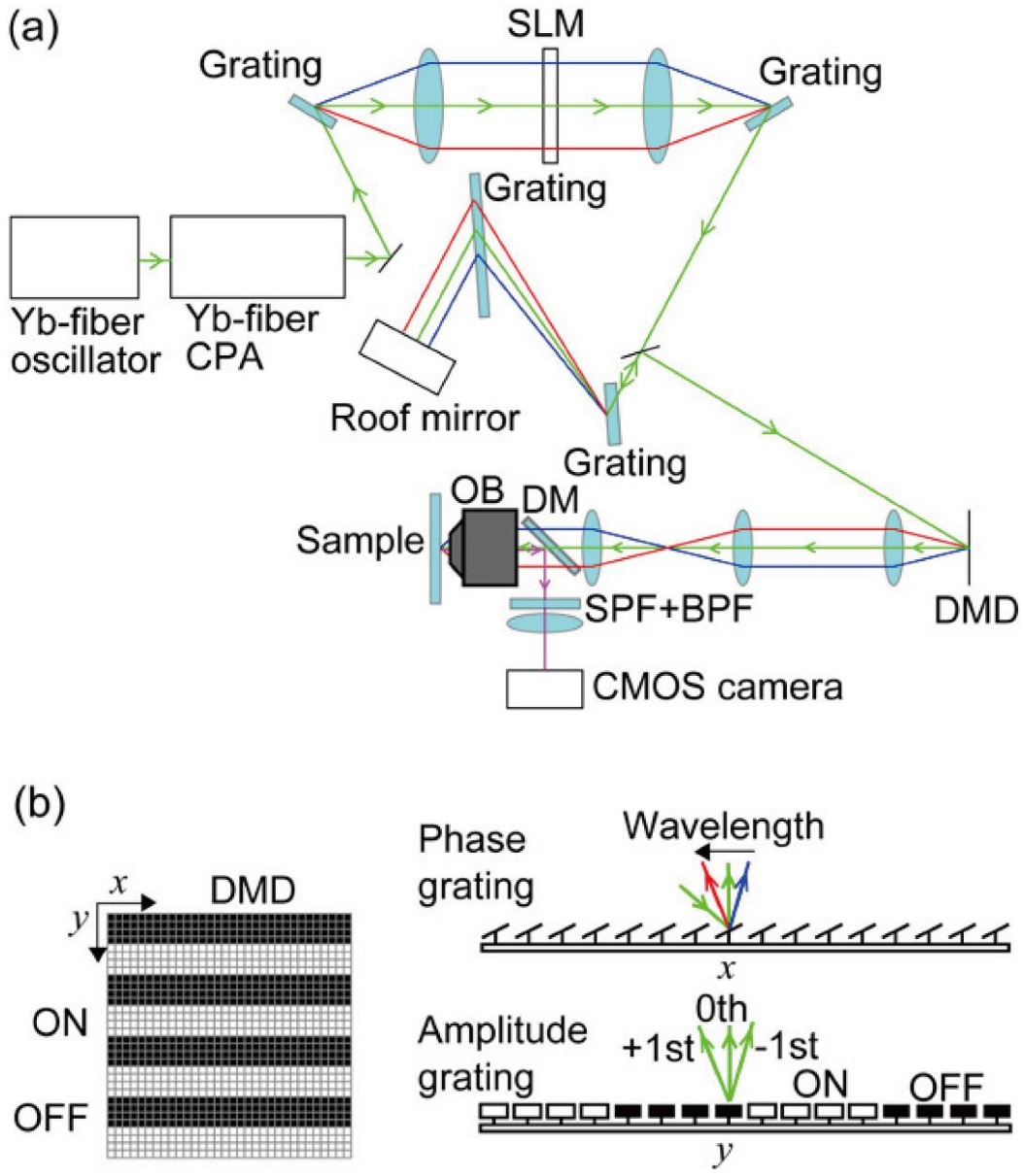

Fig 3.2 Setup of 3D-ITF, (a) setup, (b) magnified view of DMD.

Here we have 9 lateral (xy) harmonic components $J_m(\boldsymbol{r_{xy}})$ and each of them is modulated by $I_m(z)$ in axial direction (z) independently. Each lateral harmonic component is:

$$J_m(\mathbf{r}_{xy}) = e^{i(m\mathbf{p}\mathbf{r}_{xy}+m\varphi_0)}, \quad (3.3\text{-}1)$$

where the fundamental lateral spatial frequency is

$$|\mathbf{p}| = n\sin\theta|\mathbf{k}_0|, \quad (3.3\text{-}2)$$

n is the refractive index of the media. The axial modulation $I_m(z)$ for each lateral harmonic component contains several axial harmonics:

$$I_0(z) = 1 + 8\alpha^2 + 6\alpha^4 + 4\alpha^2 \cos(2qz), \quad (3.4\text{-}1)$$

$$I_{\pm 1}(z) = 4\alpha(1 + 3\alpha^2)\cos(qz), \quad (3.4\text{-}2)$$

$$I_{\pm 2}(z) = 4\alpha^2(1 + \alpha^2) + 2\alpha^2 \cos(2qz), \quad (3.4\text{-}3)$$

$$I_{\pm 3}(z) = 4\alpha^3 \cos(qz), \quad (3.4\text{-}4)$$

$$I_{\pm 4}(z) = \alpha^4, \quad (3.4\text{-}5)$$

where the fundamental axial spatial frequency is

$$q = n(1 - \cos\theta)\left|\mathbf{k}_0\right|. \quad (3.4\text{-}6)$$

For the fluorescent object with the fluorescence density distribution $S(\mathbf{r}')$ in the object coordinate $\mathbf{r}'$, it is excited by the illumination pattern $I_{TPE}(\mathbf{r}')$ and axially confined by TF effect $I_{TF}(z')$. I scan the object in the axial direction to get the image stack. This means a convolution in axial direction between $S(\mathbf{r}')$ and $I_{TPE}(\mathbf{r}')I_{TF}(z')$. At the same time each slice of image is projected from object coordinate $\mathbf{r}'$ to image coordinate $\mathbf{r}$ by the PSF of emission light $H_{em}(\mathbf{r})$. Therefore the observed raw image of a sample is

$$\begin{aligned} D(\mathbf{r}) &= \sum_{m=-4}^{+4} \int S(\mathbf{r}') I_m(z - z') J_m(\mathbf{r}_{xy}') I_{TF}(z - z') H_{em}(\mathbf{r} - \mathbf{r}') d\mathbf{r}' \\ &= \sum_{m=-4}^{+4} [(HI_m) \otimes (SJ_m)](\mathbf{r}) \\ &= \sum_{m=-4}^{+4} D_m(\mathbf{r}) \end{aligned} \quad , (3.5)$$

where $H(\mathbf{r})$ is the PSF of wide-field TF imaging and it is a product of the PSF of emission light $H_{em}(\mathbf{r})$ and TPE intensity distribution due to temporal focusing effect $I_{TF}(z)$,

$$H(\mathbf{r}) = H_{em}(\mathbf{r}) \times I_{TF}(z). \quad (3.6)$$

To illustrate the expansion of the effective OTF in 3D-ITF, I check Eq. (3.5) in the Fourier space:

$$\tilde{D}(\mathbf{k})=\sum_{m=-4}^{+4} D_m(\mathbf{k}) = \sum_{m=-4}^{+4} O_m(\mathbf{k}) e^{im\varphi_0}\, \tilde{S}(\mathbf{k}-m\mathbf{p}) \quad , (3.7\text{-}1)$$

where $O_m(\mathbf{k})=O(\mathbf{k})\otimes \tilde{I}_m(k_z)$, (3.7-2)

$$O(\mathbf{k})= \tilde{H}_{em}(\mathbf{k})\otimes \tilde{I}_{TF}(k_z) , (3.7\text{-}3)$$

$$\tilde{I}_0(k_z) = 2\alpha^2\delta(k_z+2q)+(1+8\alpha^2+6\alpha^4)\delta(k_z)+2\alpha^2\delta(k_z-2q) , (3.7\text{-}4)$$

$$\tilde{I}_{\pm1}(k_z) = 2\alpha(1+3\alpha^2)\delta(k_z+q)+2\alpha(1+3\alpha^2)\delta(k_z-q) , (3.7\text{-}5)$$

$$\tilde{I}_{\pm2}(k_z) = \alpha^2\delta(k_z+2q)+4\alpha^2(1+\alpha^2)\delta(k_z)+\alpha^2\delta(k_z-2q) , (3.7\text{-}6)$$

$$\tilde{I}_{\pm3}(k_z) = 2\alpha^3\delta(k_z+q)+2\alpha^3\delta(k_z-q), (3.7\text{-}7)$$

$$\tilde{I}_{\pm4}(k_z) = \alpha^4\delta(k_z), (3.7\text{-}8)$$

$O(\mathbf{k})$ is the OTF of wide-field TF imaging. We can get $O(\mathbf{k})$ from the Fourier transform of $H(\mathbf{r})$ in Eq. (3.6). For each lateral harmonic component $\widetilde{D}_m(\mathbf{k})$, $O(\mathbf{k})$ is shifted to multiple axial harmonics including DC and weighted by $\tilde{I}_m(k_z)$, a Fourier transform of $I_m(z)$ in Eq. (3.4) so as to form the new OTF $O_m(\mathbf{k})$.The maximum shift is twice the fundamental axial spatial frequency of the 3D illumination pattern due to the TPE effect and thus the cut-off frequency in z direction is increased by $2q$. This supports the super-resolution imaging in axial direction.

Next I shift each lateral harmonics component $\widetilde{D}_m(\mathbf{k})$ back to its original spatial frequency $\widetilde{D}_m(\mathbf{k}+m\mathbf{p})$:

$$\tilde{D}_{3D\,SIM-TF}(\mathbf{k})=\sum_{m=-4}^{+4} a_m e^{-im\varphi_0}\, \tilde{D}_m(\mathbf{k}+m\mathbf{p}) = \tilde{S}(\mathbf{k})\times\left[\sum_{m=-4}^{+4} a_m O_m(\mathbf{k}+m\mathbf{p})\right], (3.8)$$

where a_m are the weighting factors in image reconstruction. $\sum_{m=-4}^{m=+4} a_m O_m(\mathbf{k}+m\mathbf{p})$ is the effective OTF of 3D-ITF. The cut-off frequency in lateral direction is increased by

shifting $O_m(\mathbf{k})$. The maximum shift is forth the fundamental lateral spatial frequency $4\mathbf{p}$ due to the TPE effect. This offers us the super-resolution in lateral direction. Importantly, the bandwidth of the axial cone is increased beyond the diffraction limitation. This in return enhance the sectioning ability beyond diffraction limitation.

The re-constructed image in real space $D_{3D\ SIM-TF}(\mathbf{r})$ should be a Fourier transform of Eq. (3.8):

$$D_{3D\ SIM-TF}(\mathbf{r}) = \sum_{m=-4}^{+4} a_m e^{i(-m\mathbf{p}\mathbf{r}_{xy} - m\varphi_0)} D_m(\mathbf{r}) \text{ . (3.9)}$$

Eq. (3.9) guide us the way to calculate the image through knowing each of the lateral harmonic component $D_m(\mathbf{r})$, $\mathbf{p}$ and φ_0. In order to get $D_m(\mathbf{r})$, we can use the method of discrete Fourier transform at each pixel. Since we have 9 harmonics to solve, 9 sampling points are necessary. So I sample at each pixel by shifting the offset phase 9 times from 0 to $8\Delta\varphi$ with a step of $\Delta\varphi = 2\pi/9$. Each time, I take the raw image $d_n(\mathbf{r})$ which replaces the offset phase φ_0 by $\varphi_0 + n\Delta\varphi$ in $D(\mathbf{r})$. Then each lateral harmonic component can be calculated through a discrete Fourier transform:

$$D_m(\mathbf{r}) = \sum_{n=0}^{8} d_n(\mathbf{r}) e^{-i\omega_m n} \text{ , (3.10-1)}$$

where $\omega_m = \frac{2\pi}{9} m$. (3.10-2)

On the other hand, the fundamental lateral frequency $\mathbf{p}$ is a parameter known in advance and it can be measured in experiment through 2D Fourier transform of fringe image of Rhodamine B solution. The offset phase φ_0 can be calculated through searching the maximum overlap between super-resolution image $\mathrm{Re}\{e^{i(-\mathbf{p}\mathbf{r}_{xy} - \varphi_0)} D_{+1}(\mathbf{r})\}$ and its original image$|D_{+1}(\mathbf{r})|$ at each slice:

$$\arg\max_{\varphi_0 \in [0, 2\pi)} \int \mathrm{Re}\{e^{i(-\mathbf{p}\mathbf{r}_{xy} - \varphi_0)} D_{+1}(\mathbf{r}_{xy})\} \times |D_{+1}(\mathbf{r}_{xy})| \, d\mathbf{r}_{xy} \text{ . (3.11)}$$

Finally by substituting Eq. (3.10) into Eq. (3.9), I get the calculation formula to reconstruct 3D-ITF image $D_{3D\ SIM-TF}(\mathbf{r})$:

$$D_{3D\ SIM-TF}(\mathbf{r}) = \sum_{m=-4}^{+4} \sum_{n=0}^{8} a_m e^{i(-m\mathbf{p}\mathbf{r}_{xy} - m\varphi_0 - \omega_m n)} d_n(\mathbf{r}) \text{ . (3.12)}$$

3.2 Experimental condition

3.2.1 Setup parameters

Fig. 3.2 shows the experimental setup. A chirped-pulse amplified fiber laser was used as the light source. The center wavelength was 1055 nm, the pulse width was 104 fs and the repetition rate was 200 kHz. To compensate the dispersion of the system, I used a pulse shaper. In the excitation part, a DMD (Texas Instrument) offered both the phase modulation and the amplitude modulation to generate the three spatial-chirped beams. The phase modulation period of the DMD was 10.8 μm. I set the input angle as 23 degree and the central axis of the diffraction beams was perpendicular to the DMD surface. The total throughput of the DMD was 28% in including the 50% loss due to the patterning. The following collimating lens was achromatic doublet pairs and had an effective focal length of 395 mm. Then the beams were focused by a water immersion objective lens (OB; Olympus, UPLSAPO60 × W, NA 1.2). The field of view was 25 μm by 25 μm. In the detection part, the dichroic mirror and the filter was used to pass only the emission light and then the emission light was focused by a tube lens on the sCMOS camera. The exposure time was 10 msec for each raw image. I rotate the three spatial-chirped beams for 4 rotations ($0°, 45°, 90°, 135°$) and at each angle, I shift the pattern with 9 different phases. The period to shift the patterns was set at 20 msec. So one frame of 3D-ITF took 720 msec. The laser power before the objective lens was 14 mW. In order to compare the performance to TF microscopy, I set additional optical path to replace the DMD with a reflective grating. The groove density was 830 grooves/mm and the incident angle was adjusted to let the diffraction beams perpendicular to the grating. The numerical aperture of the objective lens was fully used by the TF light. By shifting on and off two mirrors, I could switch between 3D-ITF and TF mode.

3.2.2 Spectral phase optimization

The spectral phase remained in the illumination pulse of TF will degrade the sectioning ability as the spectral phase transfer to spatial phase as a wavefront distortion. In order to compensate the remained spectral phase at focal plane. I use simulated annealing method to search the optimized phase. The compensation phase is added by the spatial light modulator (SLM) in Fig 3.2. I use Rhodamine B solution to evaluate the TPEF signal. The signal is collected by a photomultiplier which replaces the sCMOS in Fig 3.2. Fig 3.3 (a) shows the optimized spectral phase which maximize the TPEF signal. The reference phase is the optimized phase with fiber laser only. Fig 3.3 (b) shows the second order interferometric trace with optimized phase. I extract the intensity autocorrelation from this and the measured pulse width after optimization is 104 fs at TF focal plane which is the same to the case only with fiber laser.

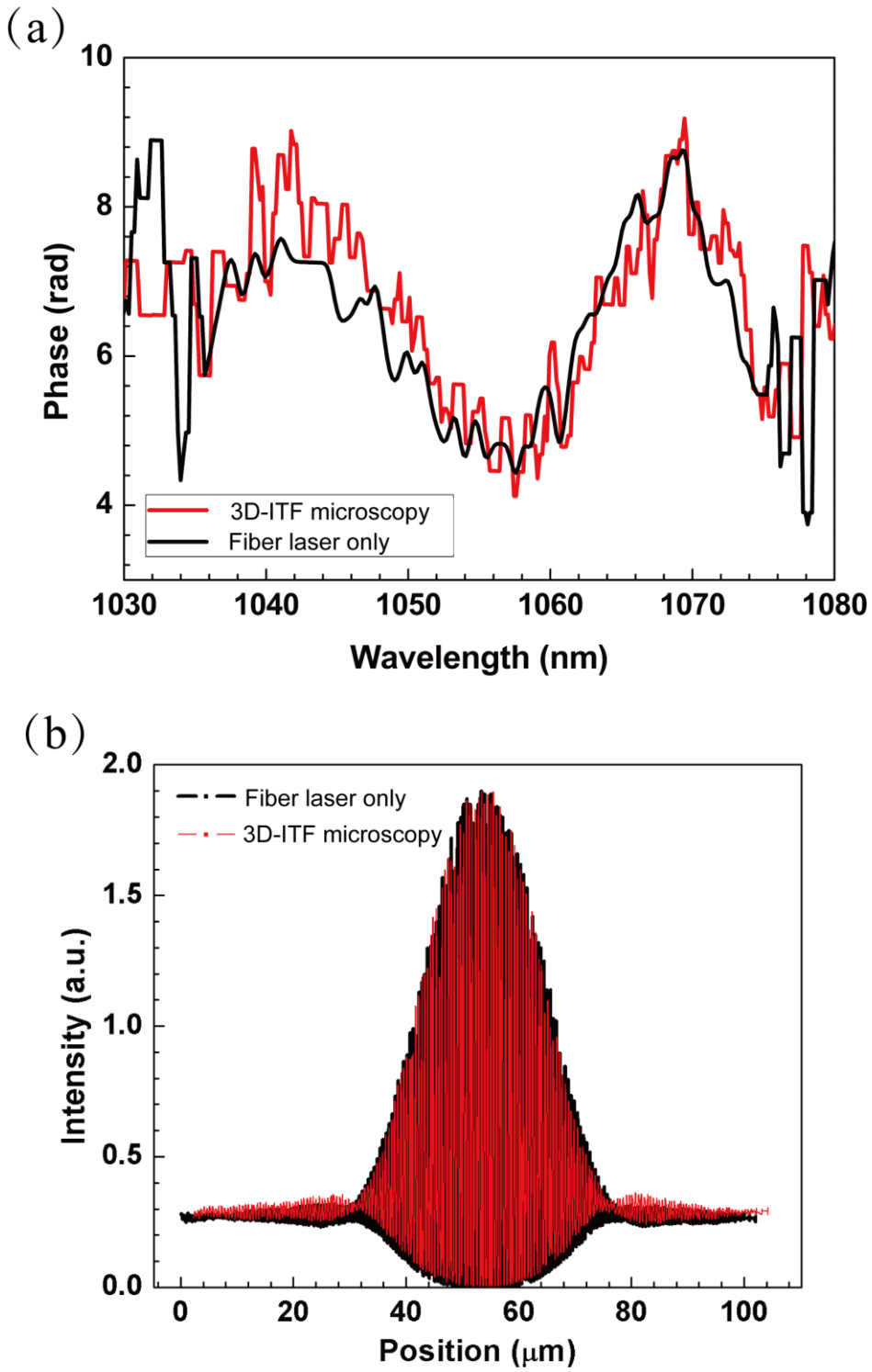

Fig 3.3 Optimized spectral phase (a) and 2nd order interferometric autocorrelation trace (b).

3.2.3 Sample preparation

The bulk solution of Rhodamine B is prepared to measure the optical sectioning ability. Rhodamine B solution was mixed with water and the concentration was 250 μM. For spatial resolution measurement, I prepared tissue-like phantom by fluorescent polystyrene beads (540/560) with a diameter of 200 nm. The beads were sealed by agarose gel and the concentration was 2.25×10^{11} beads/mL. I also prepared tissue-like phantom mixed with 200-nm fluorescent beads (540/560) and 2- μm fluorescent beads (535/575). The concentration was 2.25×10^{11} beads/mL and 9×10^{8} beads/mL respectively.

3.3 Experiment to verify improved sectioning ability

We measured the optical sectioning ability of TF and 3D-ITF separately by scanning around the surface of the Rhodamine B sample. I first extracted the fundamental lateral frequency **p** by Fourier transform of the fringe pattern. And I calculated the image following Eq. (3.12). Then I summed up the intensity of all the pixel at each layer and plot the intensity profile along axial direction. Figure 3.4 shows the results. By fitting the profile and differentiation, I get the intensity curve. The FWHM of TF is 1.7 μm and the FWHM of 3D-SIM TF is 0.65 μm. The best sectioning resolution of wide-field TPEF imaging is 0.85 μm with 800 nm excitation wavelength reported by A. Vaziri[4]. This equals to 1.12 μm sectioning resolution with 1055 nm excitation wavelength. It is the best optical sectioning resolution of wide-field TPEF imaging technique up to now by our knowledge.

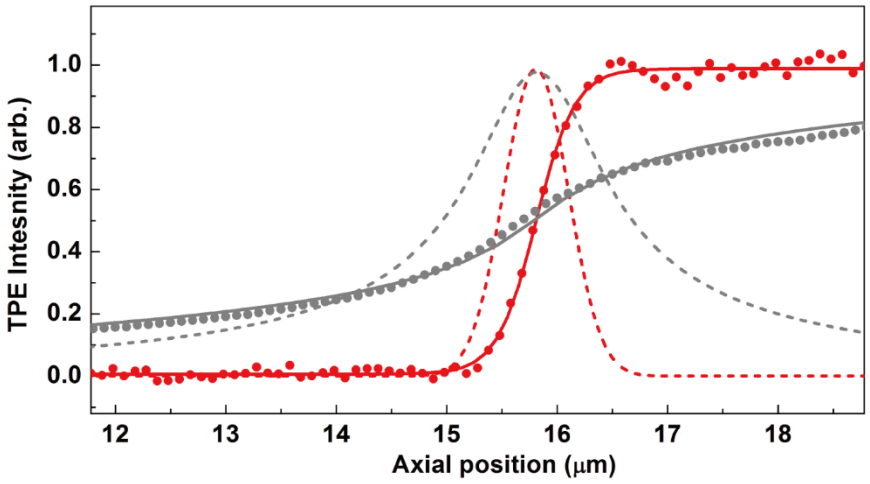

Fig. 3.4 Sectioning ability of 3D-ITF (red line) and TF (gray line)

3.4 Experiment to verify super-resolution

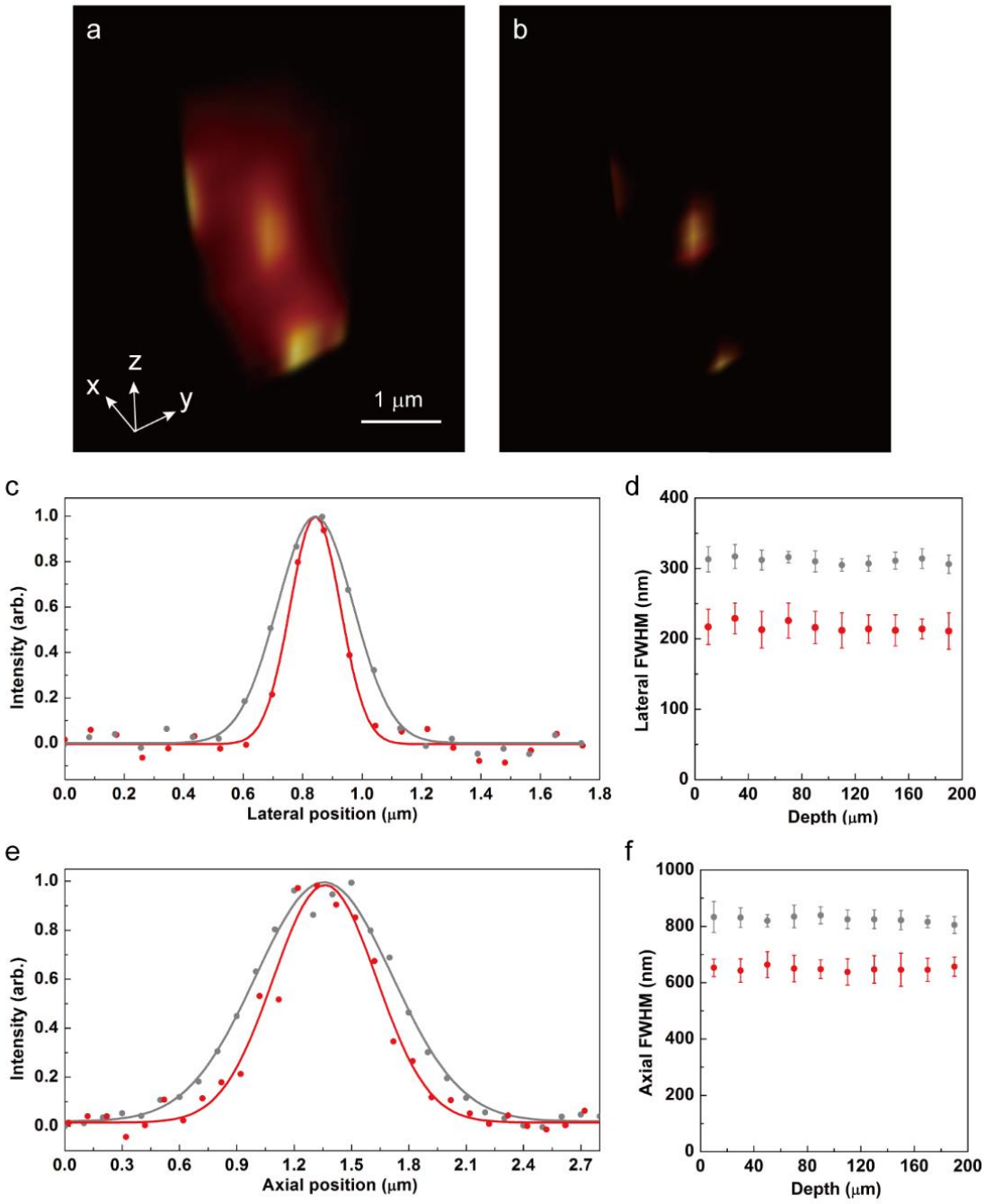

Fig. 3.5 Axial and lateral resolution measured by 200 nm beads. A fluorescent bead image in TF (a) and 3D-ITF (b) respectively. The lateral (c) and axial (e) intensity profile of this bead image in TF (gray line) and 3D-ITF (red line). The mean value and standard deviation

of lateral FWHM (d) and axial FWHM (f) for beads image along imaging depth in TF (gray line) and 3D-ITF (red line).

Next, I evaluated the spatial resolution by using 200-nm fluorescent beads only. I took the image from surface to 200 μm depth by TF and 3D-ITF respectively. Figures 3.5 (a) and (b) shows a representative bead at the depth of 98.3 μm. Figure 3.5 (c) and (e) shows the lateral and axial intensity profile of the representative bead. I fitted the profile to evaluate the FWHM. I repeated this process for at least 10 beads for every 20-μm-depth region. Figures 3.5 (d) and (f) show the statistical results. The lateral and axial FWHM for TF is 311±14 nm and 825±36 nm respectively. For 3D-ITF, the lateral FWHM is 216±24 nm, which improves 1.4 times. And the axial FWHM is 649±44 nm, which improves 1.3 times. The FWHM values of 3D-ITF has little changes from top to the depth of 200 μm. This verify the ability of 3D-ITF to achieve 3D super-resolution inside the sample. Figure 3.6 shows the axial cross section of 3D Fourier transform of the representative bead, it clearly illustrates the broadening of spatial frequency bandwidth in both lateral and axial direction for 3D-ITF.

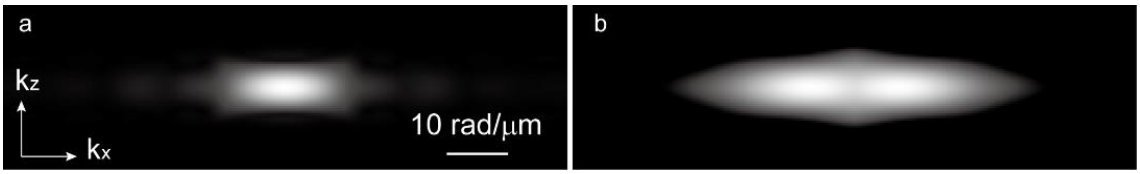

Fig 3.6 Measurement of OTF in TF (a) and 3D-ITF (b).

Figures 3.7 (a) and (g) shows the whole image of the 200-nm beads. Due to the improved sectioning ability, I found less out-of-focus background in 3D-ITF. This is numerically verified by checking the background level in Figs. 3.8 (e) and (f). Figs. 3.7 (b)-(f) and (h)-(l) show the lateral cross section at both surface and deep region. As a zoomed-in figure in Figs. 3.8, neighboring attached beads can be clearly separated at both surface and deep region.

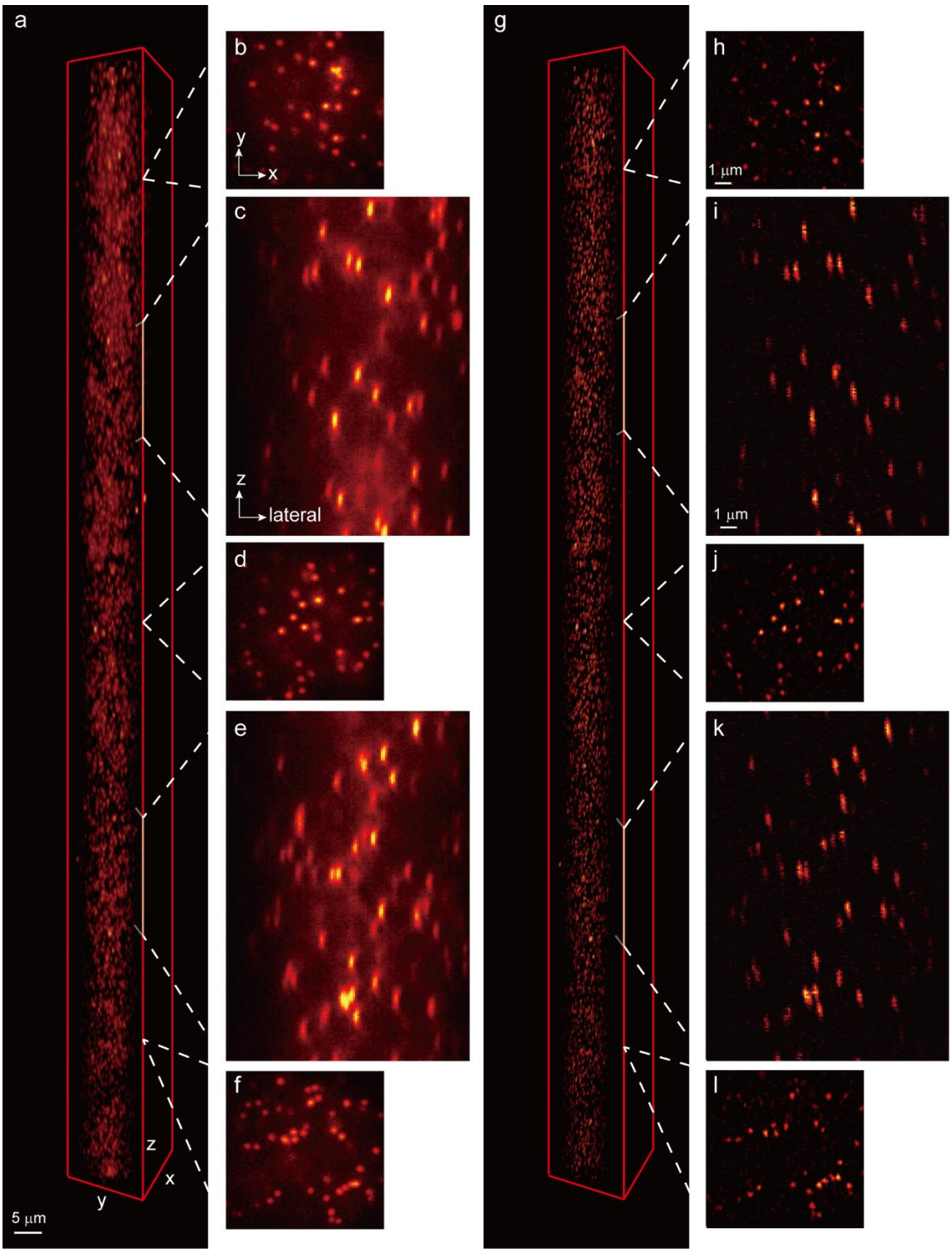

Fig. 3.7 200-nm beads from 0 to 200 um depth in TF (a-f) and 3D-ITF (g-l).

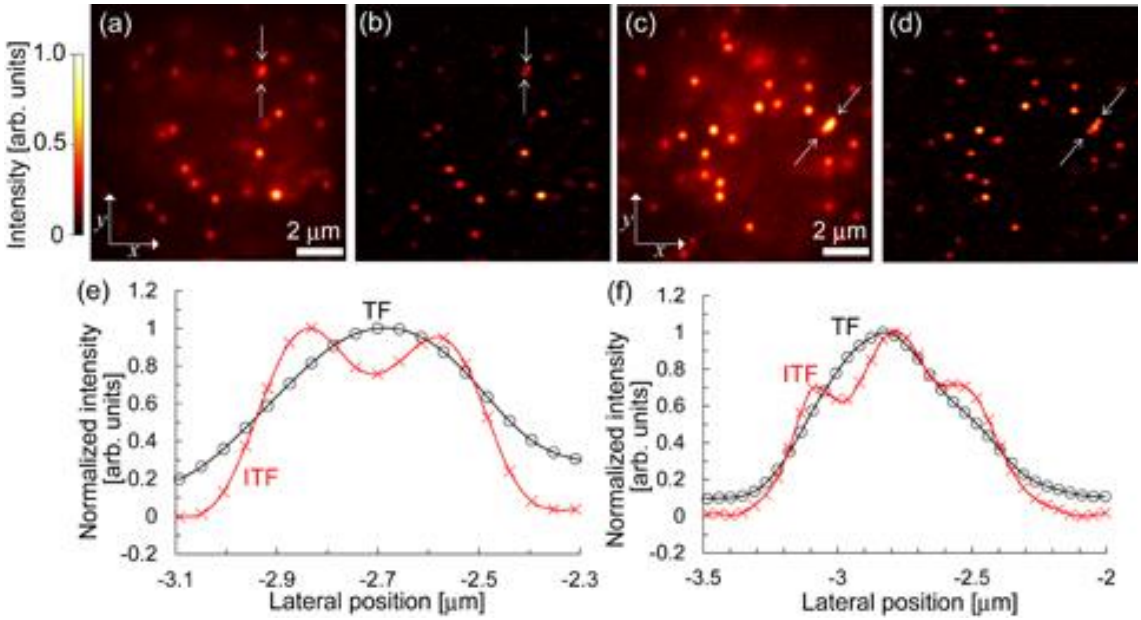

Fig 3.8 Cross-sectional (a, c) TF and (b, d) 3D-ITF images of 200-nm fluorescent beads at penetration depths of (a, b) 45 μm and (c, d) 162 μm. The signal intensities were normalized by the maximum intensity in each image. Normalized signal profiles of TF (O) and ITF (×) microscopies along the lateral direction indicated by arrows in (e) a and b, and (f) c and d.

3.5 Experiment to demonstrate background fluorescence reduction

Thirdly, I took the image of the tissue-like phantom containing both 200-nm fluorescent beads and 2-μm fluorescent beads. Figures 3.9 (a) and (b) shows the image at the depth of 70 μm. The out-of-focus background from 2-μm fluorescent beads buries the 200-nm fluorescent beads around it in TF. However, for 3D-ITF, its supper sectioning ability dramatically reduce the out-of-focus signal and thus I could clearly resolve each 200-nm-fluorescent bead. Figures 3.9 (c) and (d) shows the axial cross section, at the bottom, it is the top surface of the 2-μm fluorescent bead whose out-of-focus signal is suppressed in 3D-ITF. And its neighboring beads which are hard to identify in TF are now well presented. Figures 3.9 (e) and (f) show the lateral cross section, I trace the intensity distribution along the white line and it shows the improvement of the imaging contrast of each bead due to enhanced sectioning ability. The minus value shown in the intensity profile is due to the enhancement of high frequency in image reconstruction and is simply set as zero in image representation. I also investigated the FWHM of the lateral intensity profile of the 200-nm-

fluorescent bead. In Fig. 3.10 (a), I compare the profile of the bright beads in Figs 3.9 (e) and (f) with the representative beads in Figs 3.5 (a) and (b) for both TF and 3D-ITF. I did the same comparison for the 5 beads in Fig 3.9 (e) and (f). As Fig 3.10 (b) shows, the lateral FWHM increases 10% from 311 nm to 346 nm in TF while it is almost the same for 3D-ITF from 216 nm to 221 nm.

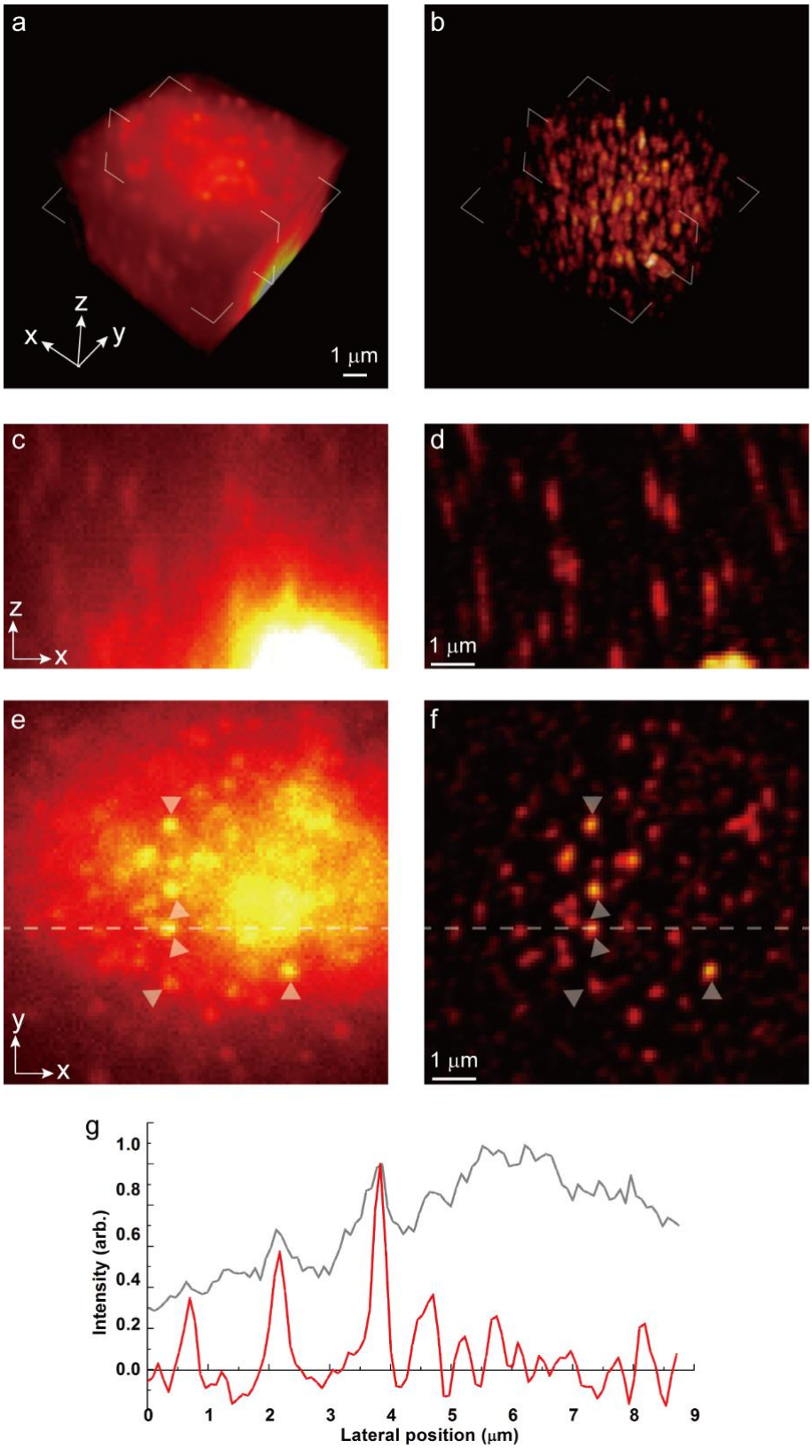
a
z
x
y
1 μm
b
c
z
x
d
1 μm
e
y
x
f
1 μm
g
Intensity (arb.)
1.0
0.8
0.6
0.4
0.2
0.0
0
1
2
3
4
5
6
7
8
9
Lateral position (μm)

Fig. 3.9 Phantom of mixed beads. The 3D view of beads image in TF (a) and 3D-ITF (b). The axial cross section image in TF (c) and 3D-ITF (d). The lateral cross section image in TF (e) and 3D-ITF (f). The intensity profile (g) in the dashed line in TF (gray line) and 3D-ITF (red line).

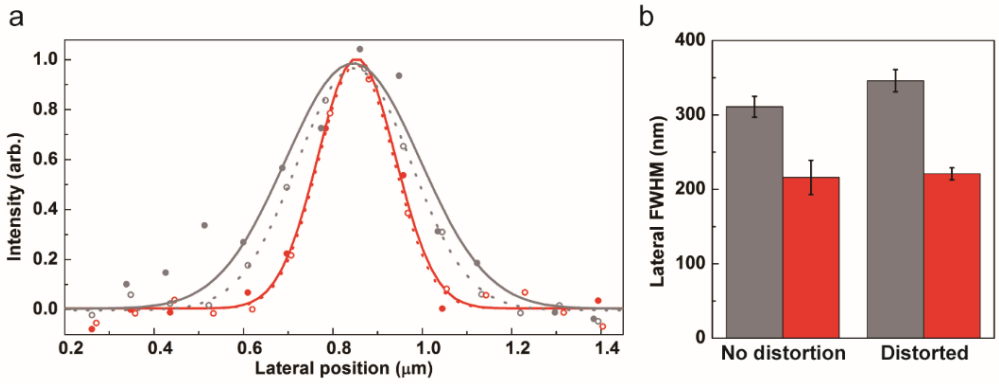

Fig. 3.10 Resistance in spatial resolution in 3D-ITF compared to TF. (a) The intensity profile of a bead image in TF with optical distortion (solid gray line) and without optical distortion (dashed gray line) compared to in 3D-ITF with optical distortion (solid red line) and without optical distortion (dashed red line). (b) The mean value and the standard deviation of lateral FWHM of beads' image in TF (gray) and 3D-ITF (red).

3.6 Summary

I demonstrate a super-sectioning as well as 3D super-resolution wide-field TPEF microscopy. The sectioning ability was 0.65 μm for the excitation wavelength of 1055 nm. The lateral and axial resolution was 216 nm and 649 nm respectively. I verified this in a tissue-like sample. The current imaging speed for one frame is 720 msec. This can be improved by using high frame rate sCMOS and intensifier. On the other hand, the field of view could also be increased if I further amplify the fiber laser power.

More interestingly, 3D-ITF could remain the spatial resolution for a deeper region compared to TF. I think that the degradation of the spatial resolution in TF is due to the emission wavefront distortion. In the case that the original PSF is slightly broadened by the wavefront distortion, 3D-ITF can keep the spatial resolution and be resistant to the wavefront distortion. I will investigate this characteristic in next chapter.

References

1. Toda, K. *et al.* Interferometric temporal focusing microscopy using three-photon excitation fluorescence. *Biomed. Opt. Express* **9,** 1510 (2018).

2. Choi, H. *et al.* Improvement of axial resolution and contrast in temporally focused widefield two-photon microscopy with structured light illumination. *Biomed. Opt. Express* **4,** 995–1005 (2013).

3. Isobe, K. *et al.* Temporal focusing microscopy with structured illumination for super-resolution deep imaging. in *Optics InfoBase Conference Papers* (2014).

4. Vaziri, A. & Shank, C. V. Ultrafast widefield optical sectioning microscopy by multifocal temporal focusing. *Opt. Express* **18,** 19645 (2010).

Chapter 4

Resistance to optical distortions in 3D-ITF microscopy

In this chapter, I analyze how optical distortions in deep imaging or dense scattering media including absorbing-scattering, forward scattering and wavefront distortion influence on 3D-ITF imaging and derive the distorted PSF and OTF. Upon this, I find that 3D-ITF microscopy is less affected by the optical distortions in terms of spatial resolution, sectioning ability and artifacts. TF illumination support a robust spatial modulation in 3D-ITF microscopy in distorted optics. As the modulation spatial frequencies are unique, they offer a redundancy in 3D-ITF microscopy. The redundancy in the spatial frequency of 3D-ITF imaging compensates the loss of spatial frequency due to the optical distortion in emission OTF. It recovers the high spatial frequencies to prevent the degradation of spatial resolution. Moreover, the redundancy recovers the hollow spatial frequency which cause disturbed shape in PSF such as side lobes and double peak. As a result, there is a more uniform OTF spectrum distribution in 3D-ITF and this leads better trade-off between remaining noise artifacts and spatial resolution after Wiener filter correction. In simulation I verify the findings.

ITF is classified as a nonlinear SIM because harmonics of the modulation frequency of the interferometric pattern is generated through multi-photon excitation as shown in Fig. 4.1 (a) and (g). But ITF doesn't offer better resolution than regular SIM. There are two reasons. First, as an example of TPEF imaging, the excitation wavelength is around two times the emission wavelength thus the possible maximum spatial modulation frequency is around the cut-off spatial frequency of the emission OTF, which is the same in regular SIM. Secondly, as shown in Fig. 4.1 (a) the higher the spatial modulation frequency, p, q, lateral and axial respectively is the lower the axial spatial frequency support in TF, k_{TF} is. Thus there is a trade-off between enhanced spatial resolution and TF sectioning ability. This makes the maximum spatial modulation frequency even lower than the cut-off spatial frequency of emission OTF. On the other words, the spatial frequency bandwidth of each

sub image of different modulation frequency is not fully utilized to enhance spatial resolution since there are many useless overlapping in the spatial spectrum as shown in Fig. 4.1 (f) and (g). As N modulation frequencies (excluding DC) requires 2N+1 raw images to separate them, the waste in spatial frequency bandwidth is the waste in acquisition time. This is the drawback of ITF in perfect optics. However, the overlap in spatial spectrum of sub images in fact gives ITF redundancy in spatial frequency domain. And 3D-ITF has more redundancy compared to 2D-ITF as there are more overlap of spatial frequency among sub images. The redundancy can make up the loss of spatial frequency in emission OTF due to optical distortions so that the 3D-ITF has the resistance to optical distortions.

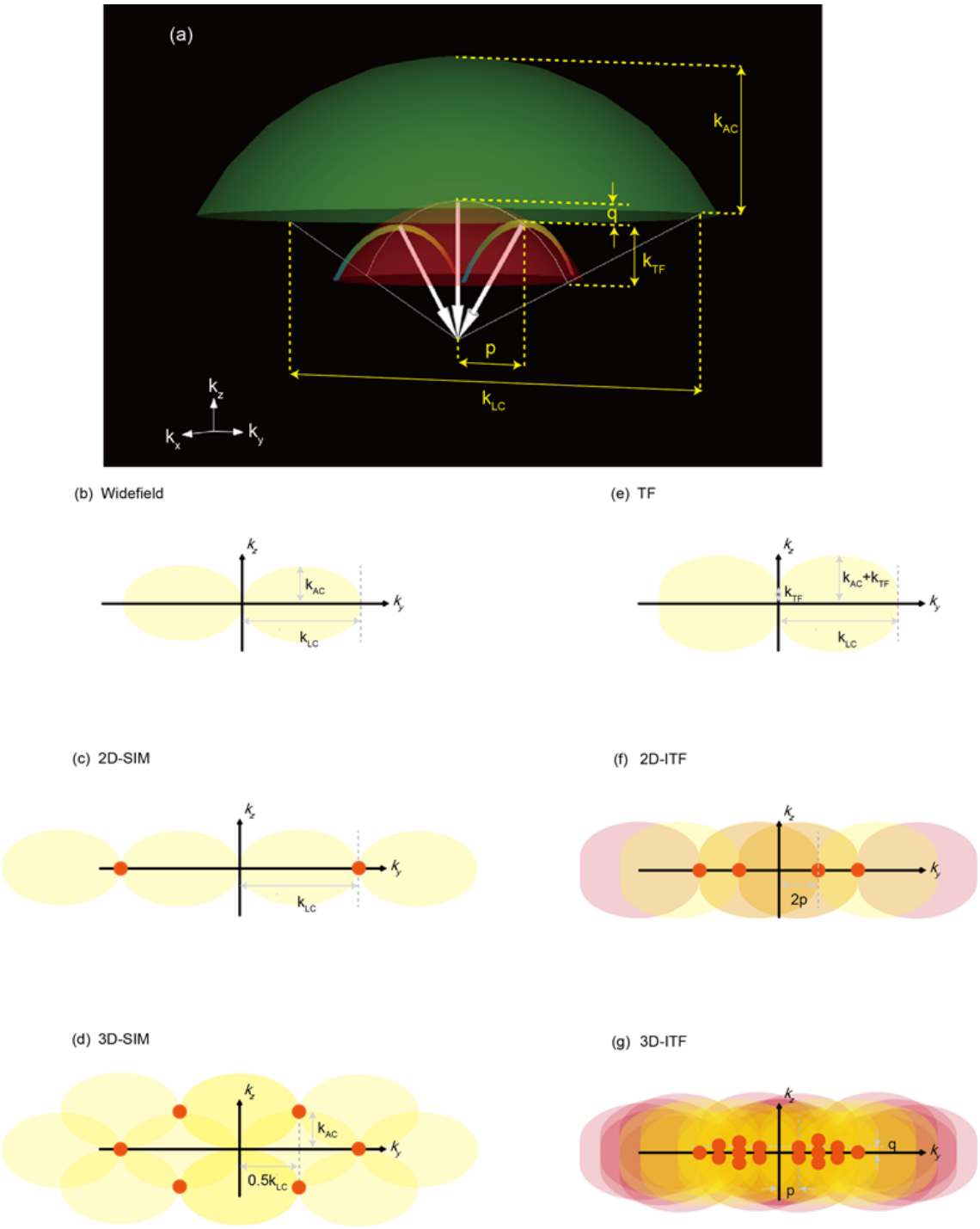

Fig. 4.1 The redundancy in 3D-ITF OTF. (a) The wave vectors (white vectors) of three diffraction orders in 3D-ITF illumination. Red sphere corresponds to possible illumination wave vectors in 3D-ITF illumination while green sphere corresponds to possible TPEF emission wave vectors in 3D-ITF. Two rainbows corresponds to +1 and -1 order TF illumination wave vectors and there is a trade-off between the axial frequency support in TF, k_{TF} and the fundamental spatial modulation frequency in 3D-ITF, p, q, lateral and axial respectively. (b, e) The OTF in widefield microscopy (b) and TF microscopy (e). The OTF

in widefield microscopy is also the emission OTF. The OTF in TF microscopy is an axial convolution of the emission OTF and the TF sectioning ability. (c, d) The OTF in 2D-SIM (c) and 3D-SIM (d). The red dots indicates the modulation frequencies and the yellow double ellipses indicate the shifted sub OTFs which are the same as (b). DC sub OTF is excluded in order to remove the background fluorescence. There is little frequency overlap in SIM and most of them occur in low spatial frequency or the boundary region between the sub-OTFs. (f, g) The OTF in 2D-ITF (f) and 3D-ITF (g). The red double ellipses indicate the shifted sub OTFs due to TPE. Both the red and yellow double ellipses are the same as (e). In contrary to SIM, large amount of frequency overlaps in 3D-ITF. And multiple sub bands overlap. This supports the redundancy in 3D-ITF.

In order to prove the resistance of 3D-ITF to optical distortions strictly, I have to consider not only the distorted emission but also the distorted illumination in 3D-ITF since I don't know whether the present algorithm generate additional errors with distorted spatial modulation in 3D-ITF. How distorted optics influence on SIM and TF illumination has been separately studied but not yet on ITF microscopy. I extend this study on 3D-ITF microscopy. 3D-ITF illumination mixes chromatic and monochromatic distortions. Longer wavelength is used in deep imaging or dense scattering media. These differ from the distortions in SIM illumination. How optical distortions affect 3D-ITF illumination and how these affections transfer through image reconstruction is analyzed in section 4.1. Then, considering emission distortion, I derive the distorted PSF of 3D-ITF microscopy. By this, I verify the redundancy in distorted 3D-ITF and confirm that there are no additional image artifacts due to distorted illumination. The optical distortion in general reduces the image SNR and effectively reduces the cut-off frequency in TF OTF. In section 4.2, I use simulation to first investigate the resistance of resolution to the reduction of effective cut-off frequency in 3D-ITF. Then in section 4.3, I consider the influence of emission wavefront distortion, which is the main optical distortion in 3D-ITF and TF, and study the resolution and noise artifacts at different levels of background fluorescence via simulation.

4.1 Redundancy in image spectrum

In this section, I derive the distorted PSF and OTF of 3D-ITF microscopy based upon the principle of SIM and wide-field TF's performance in distorted optics as well as considering the distorted emission light. I first review the PSF of 3D-ITF microscopy in perfect optics.

4.1.1 PSF of 3D-ITF in perfect optics

The reconstructed 3D-ITF image is rewritten from Eq. (3.8) as

$$\tilde{D}_{3D\text{-}ITF}(\mathbf{k}) = \tilde{S}(k) \times \left[\sum_{m=-4}^{+4} a_m \tilde{I}_{TF}(k_z) \otimes \tilde{I}_m^{(2)}(k_z) \otimes \tilde{H}_{em}(\mathbf{k} + m\mathbf{p}) \right], \quad (4.1)$$

where a_m is the weighting factor, which can be adjusted to enhance high-frequency support or improve signal-to-noise ratio (SNR). Here, a_0 is set as 0 to exclude the DC sub-band for background fluorescence subtraction. Note that instead of simple weighting in Eq. (4.1), I can use the Weiner filter to achieve flat synthesized bandwidth. From Eq. (4.1), I know that the effective OTF of 3D-ITF microscopy is

$$\tilde{H}_{3D\text{-}ITF}(\mathbf{k}) = \sum_{m=-4}^{+4} a_m \tilde{I}_{TF}(k_z) \otimes \tilde{I}_m(k_z) \otimes \tilde{H}_{em}(\mathbf{k} + m\mathbf{p}) \, . \quad (4.2)$$

By inverse Fourier transform, it is the effective 3D-ITF PSF,

$$H_{3D\text{-}ITF}(\mathbf{r}) = \left[\sum_{m=-4}^{+4} a_m \exp(-m\mathbf{pr}) I_m(z) \right] \times H(\mathbf{r}) \, , \quad (4.3)$$

The left part of Eq. (4.3) contains the super composition of harmonics in lateral and axial directions, which is almost a replica of the TPE pattern of the 3D interferometric pattern but reorganizes the weighting. This part offers us the super-resolution imaging. The right part of Eq. (4.3), $H(\mathbf{r})$, is the PSF of TF microscopy, and is the product of TF sectioning ability and emission PSF as shown in Eq. (3.6). In TF PSF, TF sectioning ability only affects the axial direction to narrow the shape of emission PSF. Numerically, the FWHM of the TF sectioning ability is much larger than the axial FWHM of the emission PSF, so the TF PSF is dominated by the emission PSF.

4.1.2 PSF and OTF with distorted optics

Now, I consider the effects of optical distortions[1–8]. In imaging practice, the sample and environment differ from the ideal conditions. Substantial distortions arise from the mismatch of the refractive index among sample, immersion media, mounting media and

objective lens, and the inhomogeneous refractive index distribution of the sample itself. These distort the wavefront so that the phase of the spatial frequency is modulated in pupil function. Another type of distortion arises from absorption and small-scale particle-induced scattering, such as Rayleigh scattering, and it mainly attenuates the ballistic photons. Since the high spatial frequency components have more loss due to a longer journey inside absorption and scattering media, effectively they reduce the spatial frequency bandwidth. The third type of distortion is large-scale particle-induced scattering, such as Mie scattering or forward scattering, which usually happens in tissue with longer wavelength. In addition to the previous effects, it diffuses the spatial frequency. High spatial frequency has more chance to shift to low spatial frequency than vice versa due to a longer pathway in the scattering media.

For distorted illumination light, analysis becomes complicated as multiple colors are involved. To handle this, I will transfer the chromatic effects as temporal effects. Statistically, I first classify the illumination light as ballistic light and scattered light. Ballistic light is only wavefront-distorted and attenuated. For ballistic light, each dispersed colorful dot at the back aperture of the objective lens is coupled to a spatial frequency as shown in Fig. 4.1(a). The common phase alteration of the dispersed dots inside each diffracted line is effectively viewed as a result of monochromatic wavefront distortion. In fact, in 3D-ITF, we have three diffraction orders as illumination light so that the monochromatic wavefront distortion contains only three phase variations corresponding to +1, 0 and -1 diffraction orders. As with SIM, these change the offset phases of the interferometric pattern, which leads to a spatial shift. Variation in offset phase is not a problem if we regard the offset phase as an unknown parameter. We can search the offset phase by maximizing the cross correlation of the real part and absolute part of the corresponding sub-band image or by other computational algorithms[9,10].

The remaining phase alterations of the dispersed dots inside each diffracted line are effectively viewed as chromatic wavefront distortion, which is a spectrum phase modulation. This chromatic characteristic does not only originate from the difference of refractive index but mainly from the difference of pathway. Different dots of color have different pathways and thus face different manners of scattering, refraction and absorption. The effective chromatic distortions stretch and distort the temporal profile of the 3D

interferometric pattern so as to degrade the TF sectioning ability. I use distorted TF sectioning ability, $I_d(\mathrm{z})$, to describe it.

For 3D-ITF illumination, scattered light, as non-ballistic light, is mainly a result of forward scattering, which dominates the scattering process in tissue imaging and for longer wavelength. Forward scattering, or small-angle scattering, detunes the spatial frequency of illumination light. Statistically, the phases of detuned light of different colors, especially from different diffraction orders, are mostly uncorrelated. Thus, in the time domain, the scattered light barely forms a short pulse compared to ballistic light, and its contributions are further suppressed by TPE. Thus, the modulation frequency of the interferometric pattern is not altered by forward scattering. This characteristic of locking spatial frequency was reported in a previous TF work. On the contrary, statistically the phases of detuned light of neighboring colors inside the same diffraction order are mostly correlated. The scattered light contributes to the DC component of the interferometric pattern and diffuses the DC component in the spatial spectrum. The light as speckles transfers to the 0^{th} order image, the sub-image with $m = 0$ in Eq. (4.1). By homodyne detection, I can successfully separate the altered 0^{th} order image from other orders' images. To eliminate the error, I simply don't use the 0^{th} order image in image reconstruction. Indeed, the scattered and out-of-focus emission light is hidden in the 0^{th} order image, and is also removed by excluding the 0^{th} order image. Thus, with distorted illumination, the image reconstruction algorithm is still valid. Through image reconstruction, the super-composition of harmonics will be retained in Eq. (4.3) with optical distortions.

Then, I consider the distorted emission light, which is the same in other wide-field microscopy. In perfect optics, as an incoherent imaging, the emission OTF, $\widetilde{H}_{em}(\mathbf{k})$ is the autocorrelation of the pupil function of the objective lens. With distorted optics, I model a distorted emission OTF, $\widetilde{H}_{dem}(\mathbf{k})$. The loss of amplitude due to Rayleigh scattering, imperfect optics and misalignment could be modeled as a non-uniform pupil function or simply as lower effective NA. The wavefront distortion could be modeled as adding the phase with corresponding Zernike polynomials to the pupil function. Both result in narrower bandwidth for the emission OTF and thus the distorted emission PSF, $H_{dem}(\mathbf{r})$ is broadened. In addition, the OTF spectrum is wavefront-distorted so that there are distorted emission PSF shapes such as side lobes or double peaks.

The magnitude of optical distortions is usually depth-dependent and thus the distorted TF sectioning ability, $I_{dTF}(\mathrm{z})$, and the distorted emission, PSF, $H_{dem}(\mathbf{r})$, are depth-dependent functions as $I_{dTF}(\mathrm{z},\mathrm{z}')$ and $H_{dem}(\mathbf{r},\mathrm{z}')$ respectively where z' is the depth argument. Here, I don't consider the lateral dependency of distortion because the path-length difference in the sample is negligible within the ~100-μm field of view. As a summation of previous analysis, with distorted optics, the distorted j^{th} raw image should be revised from Eq. (3.5) as

$$D_j(\mathbf{r}) = \sum_{m=-4}^{+4} \int S(\mathbf{r}') \exp\left[i(m\mathbf{p}\mathbf{r}' + \varphi_{m,j}) \right] I_{dTF}(z-z', z) I_m(z-z') H_{dem}(\mathbf{r}-\mathbf{r}', z') d\mathbf{r}' . \quad (4.4)$$

In the z' domain, the integration is approximately non-zero around only the TF-sectioned image plane at depth z. Thus, the integration is affected by only the in-focus distorted emission PSF around depth z, so the distorted emission PSF in Eq. (4.4) can be replaced by $H_{dem}(\mathbf{r}-\mathbf{r}', \mathrm{z})$, which replaces its depth argument z' with z. For the targeted details such as cells or synapses located at depth z_0, only the sectioned images at depth $\mathrm{z} \approx \mathrm{z}_0$ are required to build up their 3D image. Thus, the depth argument z in the distorted TF sectioning ability, $I_{dTF}(\mathrm{z}-\mathrm{z}', \mathrm{z})$, and the distorted emission PSF, $H_{dem}(\mathbf{r}-\mathbf{r}', \mathrm{z})$, could be replaced by z_0 in order to evaluate the effective PSF of the targeted details. With these replacements, Eq. (4.4) can still be written as a form of convolution as

$$\begin{aligned} D_j(\mathbf{r}) &= \sum_{m=-4}^{+4} \int S(\mathbf{r}') \exp\left[i(m\mathbf{p}\mathbf{r}' + \varphi_{m,j}) \right] I_{dTF}(z-z', z_0) I_m(z-z') H_{dem}(\mathbf{r}-\mathbf{r}', z_0) d\mathbf{r}' \\ &= \sum_{m=-4}^{+4} S(\mathbf{r}) \exp\left[i(m\mathbf{p}\mathbf{r} + \varphi_{m,j}) \right] \otimes \left[I_{dTF}(z, z_0) I_m(z) H_{dem}(\mathbf{r}, z_0) \right] \end{aligned} .$$

(4.5)

Through the same analysis from Eq. (3.5) to Eq. (4.3), I derive the distorted 3D-ITF PSF from Eq. (4.5) as

$$H_{d3D\text{-}ITF}(\mathbf{r}, z_0) = \left[\sum_{m=-4}^{+4} a_m \exp(-im\mathbf{p}\mathbf{r}) I_m(z) \right] \times H_d(\mathbf{r}, z_0) , \quad (4.6)$$

where the distorted TF PSF is

$$H_d(\mathbf{r}, z_0) = I_{dTF}(z, z_0) H_{dem}(\mathbf{r}, z_0) . \quad (4.7)$$

Here, the distorted 3D-ITF PSF and the distorted TF PSF are both depth-dependent functions. I will drop the depth argument as it doesn't affect further analysis. This can be picked up at any further equation. Compared to Eq. (4.3) and Eq. (3.6), the distorted optics only influence the TF PSF. For spectrum view, the distorted 3D-ITF OTF is a Fourier transform of Eq. (4.6) as

$$\tilde{H}_{d\,3D\text{-}ITF}(\mathbf{k}) = \left[\sum_{m=-4}^{+4} a_m \tilde{I}_m(k_z) \otimes \delta(\mathbf{k}+m\mathbf{p}) \right] \otimes \tilde{H}_d(\mathbf{k}), \quad (4.8)$$

where the distorted TF OTF is

$$\tilde{H}_d(\mathbf{k}) = \tilde{I}_d(k_z) \otimes \tilde{H}_{dem}(\mathbf{k}). \quad (4.9)$$

Equation (4.8) means that the distorted 3D-ITF OTF is a summation of shifted distorted TF OTFs. The left part of Eq. (4.8) refers to the spatial frequencies where the distorted TF OTFs are shifted. These positions are labeled as red points in Fig. 4.1 (g). As Fig. 4.1 (a) shows, in 3D-ITF, because of the limitation of the circular shape of the objective lens, a larger fundamental modulation frequency, **p**, leads to lower axial frequency support in TF, $\boldsymbol{k_{TF}}$. Correspondingly, a better 3D-ITF resolution leads to worse sectioning ability in TF. For a trade-off between them, I set the fundamental modulation frequency, **p**, as around 1/6 the cut-off frequency of the TF OTF, $\boldsymbol{k_{LC}}$ in the previous experiment. Note that a decrease of around 50% originates from the difference between the excitation and emission wavelength, while another 50% decrease comes from using a 3D-SIM scheme instead of 2D-SIM. Also, a 2/3 decrease originates from the trade-off in geometrical design. In the axial direction, the fundamental modulation frequency, **q**, is around 1/10 the cut-off frequency of the TF OTF. The relatively small value of the fundamental modulation frequency compared to SIM and the multiple harmonics offers many overlapping areas in the OTF spectrum among sub-TF OTFs. With this unique characteristic, once the distorted TF OTF loses part of its spectrum, the surrounding shifted TF OTFs can utilize the copies of the lost spectrum, which are taken from different spectrum regions of distorted TF OTF to recover the spectrum loss. There is less possibility of losing all the spectrum in distorted TF OTF, such that there is always at least one sub-TF OTF to be able to recover the spectrum loss. This is the redundancy in 3D-ITF. Next, I will investigate how the optical

distortions affect image resolution and remaining noise artifacts in TF and 3D-ITF by simulation.

4.2 Resistance to reduction of cut-off frequency

In this simulation, a point object is used to evaluate both the spatial resolution and noise artifacts. The excitation wavelength is 1,060 nm and the emission wavelength is 560 nm. The objective lens has a numerical aperture of 1.2 with water immersion (n=1.33). The cut-off frequency of the emission OTF is 26.9 rad/μm and 8.5 rad/μm in the lateral and axial directions respectively. The FWHM of the sectioning ability in TF is 2.7 μm, which corresponds to a bandwidth of 2.3 rad/μm. The fundamental modulation frequency is 4.1 rad/μm and 1.2 rad/μm in the lateral and axial directions respectively. The weighting of the modulation frequencies is set by maximizing the total AC weighting inside the TPE interferometric pattern. In 3D-ITF, the interferometric pattern with three directions at 0 °, 120 ° and 240 ° is used. In each direction, nine raw images are simulated. The spatial averaged and temporal integrated TPE energy in each 3D-ITF raw image is 1/27 times that in TF microscopy. It guarantees the summation of the 27 raw images' TPE energy is the same as that of the TF image. Thus, the SNR (shot noise) of the summation image of 3D-ITF raw images is the same as the SNR in the TF image. In post processing, a 3D Wiener filter and apodization filter, which was introduced in 3D-SIM, are used in both 3D-ITF and TF images. The 3D Wiener filter is constructed by the distorted 3D emission OTF. It corrects the distorted emission OTF in both cases and smooths the synthesized spectrum in 3D-ITF OTF. The apodization filter is constructed by a 3D triangular function with cut-off frequency of the maximum spatial frequency support in TF microscopy and 0.77 times the maximum spatial frequency support in 3D-ITF to ensure an isotropic spectrum distribution.

In deep and dense sample imaging, optical distortions increase background fluorescence, which decreases the image SNR. On the other hand, the intensity of the high spatial frequency in TF OTF is relatively low. Thus, the measurable cut-off frequency is reduced by the noise even if the TF OTF is not distorted by the optical distortion. Once the TF OTF bandwidth is reduced by the optical distortion, I expect even lower effective cut-off

frequency for an acceptable SNR. Here, I investigate how the spatial resolution reacts to the reduction of the effective cut-off frequency. Figure 4.2 shows that the lateral and axial resolutions in 3D-ITF degrade much more slowly than those in TF. This simulation roughly shows the resistance of spatial resolution to optical distortions in 3D-ITF.

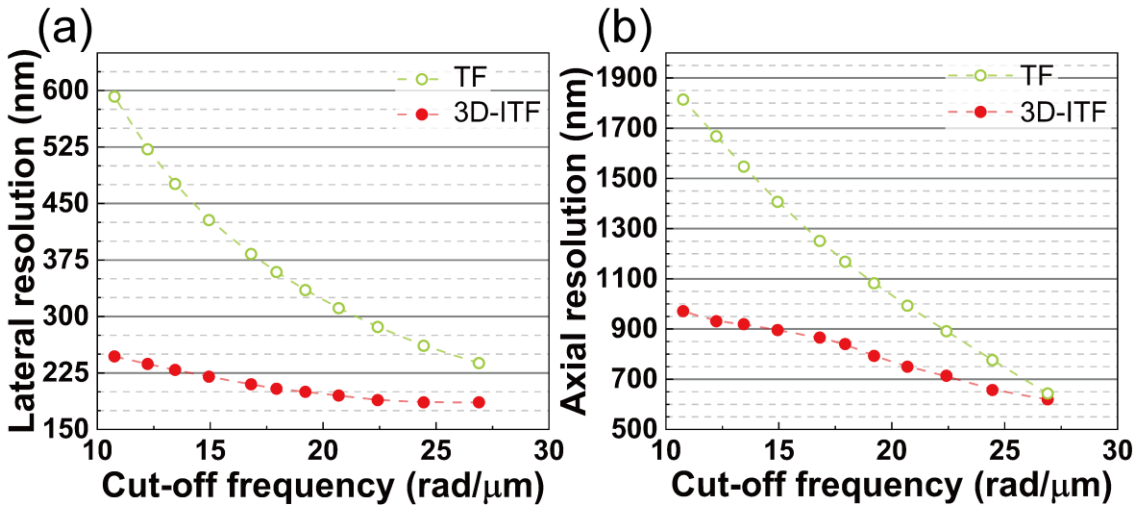

Fig. 4.2 Spatial resolution degradation with cut-off frequency reduction. (a) Lateral resolution of TF and 3D-ITF; (b) axial resolution of TF and 3D-ITF.

4.3 Resistance to wavefront distortion

Next, I consider the effect of the wavefront distortion, which is regarded as the main optical distortion. For wide-field TF, it has been reported that the wavefront distortion has little effect on TF sectioning ability, $I_{TF}(z)$. The degradation occurs for only specified Zernike mode aberration, and the degradation is less than 1.2 times for 1-rad (RMS) Zernike mode amplitude. On the other hand, the wavefront distortion in emission light dramatically degrades and distorts the emission PSF. For 2-rad (RMS) emission Zernike mode amplitude, which equals around 1 rad in illumination, the resolution could degrade several times. Thus, in TF OTF, the main effect comes from the distorted emission OTF. Therefore, I focus on the emission wavefront distortion in the simulation.

4.3.1 Lossless image spectrum

Emission wavefront distortion has two effects on TF OTF. Figure 4.3 shows an example with astigmatism (Zernike mode 5). The first effect is to narrow the OTF bandwidth. With reduced bandwidth, the spatial resolution degrades in TF as Figs. 4.3 (c) and (d) show. The second effect is to distort the OTF spectrum. As Fig. 4.3 (a) shows, the astigmatism has an OTF in a cross shape, which is anisotropic. This distortion in the OTF spectrum leads to an axial double peak in PSF as Fig. 4.3 (d) shows. In contrast, in 3D-ITF, thanks to the redundancy, the lost spectrum caused by the wavefront distortions is recovered by the redundancy. Thus, the whole spectrum is relative uniform and isotropic as Figs. 4.3 (e) and (f) show. Therefore, I know that the 3D-ITF's OTF spectrum is relatively lossless with distorted optics compared to that in TF.

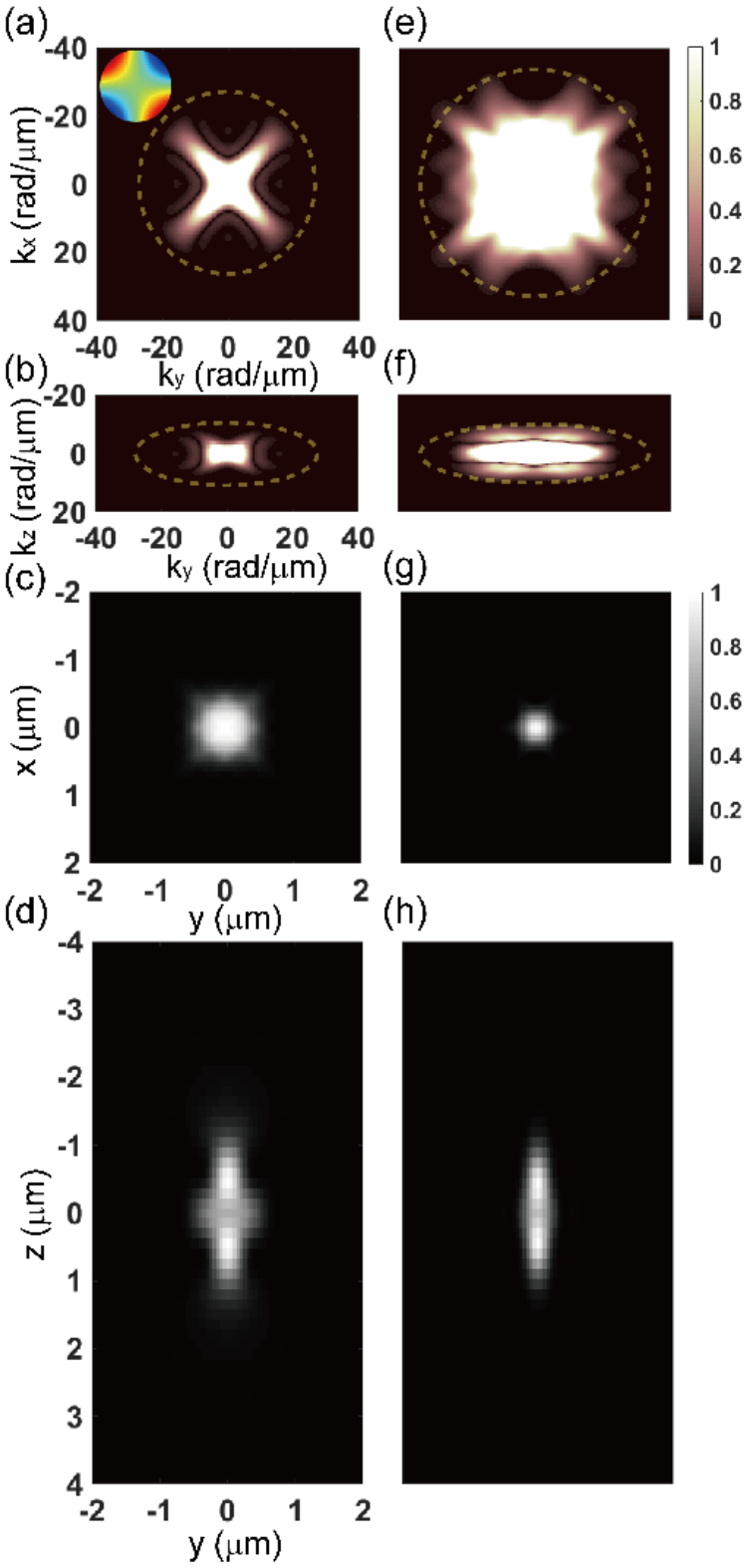

Fig. 4.3 OTF and PSF with wavefront distortion before using Weiner filter and apodization filter and without considering background fluorescence and shot noise. (a) OTF_{xy} and (b)

OTF_{zy} in TF with Zernike mode magnitude of 2 rad (RMS), (c) corresponding PSF_{xy} and (d) PSF_{zy}. (e) OTF_{xy} and (f) OTF_{zy} in 3D-ITF with Zernike mode magnitude of 2 rad (RMS), (g) corresponding PSF_{xy} and (h) PSF_{zy}. In (a, b, e, f) OTF is normalized by the maximum magnitude and the plot is saturated at 0.05; the dashed yellow circle shows the cut-off frequency of the apodization filter. The wavefront distortion is astigmatism (Zernike mode 5). The insert in (a) is the phase modulation of Zernike mode 5.

4.3.2 Resistance of spatial resolution and sectioning ability in deep imaging

Next, for the practical image, we should consider the shot noise. Secondly, we must consider the background fluorescence in deep and dense sample imaging, as well as their shot noise. The bias of the noise (mean value) can be removed, but the variance of the noise such as shot noise will remain, such that the noise artifacts will occur in the processed image. The peak photon number in the TF image without distortion is 27,000. In each 3D-ITF raw image without distortion, the average peak photon number is 1,000. With emission wavefront distortion, the TPE energy doesn't change, but the peak photon number in the raw image decreases. The background fluorescence contains the out-of-focus and scattered emission. In simulation, a background fluorescence of one magnitude means that the background fluorescence is simulated by additive white Gaussian noise with a mean of 27,000 photons and variance of 2,700 photons in the TF image. The same amount of noise is equally distributed in 27 raw images in 3D ITF microscopy. For any other background magnitude, it scales the background photon number with corresponding magnitude. By adjusting the magnitude of background, I simulate the condition at different imaging depths.

In each simulation condition, I set a threshold SNR value, and I search for the spatial resolution that satisfies the request by adjusting the noise suppression parameter in the Wiener filter. Signal value is the peak intensity of the point object after image processing and noise-bias reduction. Noise value is estimated by the square root of the variance in the spatial region far away from the point object. The acceptable SNR is set as 10 for the TF image and 100 for the 3D-ITF image. The choice of acceptable SNR depends on the requirement of imaging quality and thus it can be tuned. Lower acceptable SNR results in better spatial resolution in the Wiener filter. For TF, if I choose an acceptable SNR the same as 3D-ITF, the spatial resolution of TF will further degrade. As a trade-off, I choose

an acceptable SNR of TF lower than 3D-ITF here. Figure 4.4 shows the results with either astigmatism or spherical aberration at different imaging depths for TF and 3D-ITF. The spatial resolution is almost the same in 3D-ITF but degrades in TF with wavefront distortion. Moreover, with increasing imaging depth where the background fluorescence increases, 3D-ITF still maintains the spatial resolution while the TF image further degrades. Note that 3D-ITF retains a spatial resolution beyond diffraction limitation with distorted optics in deep and dense sample imaging. This shows the resistance of 3D-ITF in practical imaging.

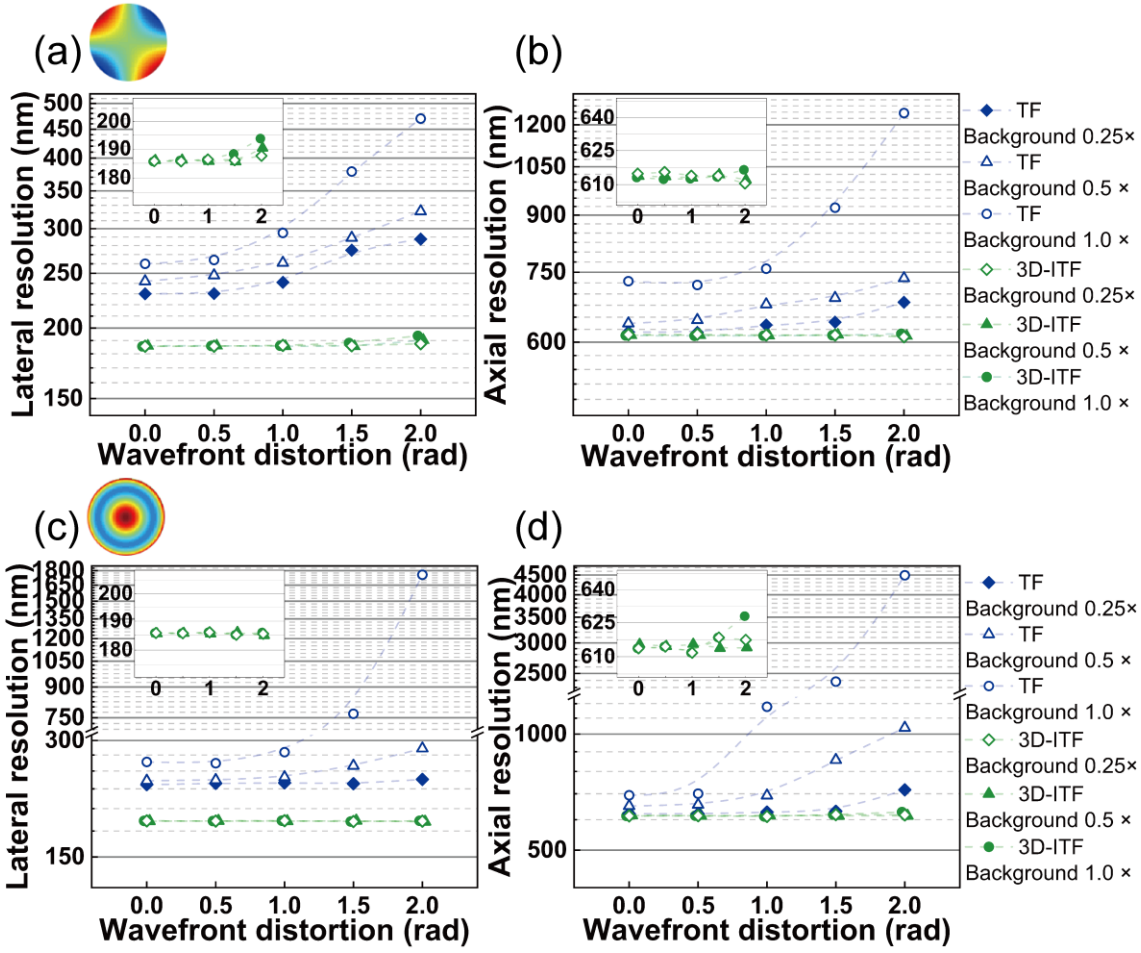

Fig. 4.4 Spatial resolution degradation with wavefront distortion and background fluorescence. (a) Lateral resolution change and (b) axial resolution change for astigmatism (Zernike mode 5). (c) Lateral resolution change and (d) axial resolution change for spherical aberration (Zernike mode 11). The insert is enlarged view for resolution change in 3D-ITF. The top left corner in (a, c) shows the phase modulation of corresponding Zernike mode.

In a Wiener filter, the noise artifacts can be suppressed at the cost of losing weak spatial spectrum. As a general rule, since the weak spatial spectrum region has relatively low SNR, I can improve the whole-image SNR by reducing its weighting in the whole-image spectrum. In the TF image, the weak spectrum region plays the short board role in the Barrel principle[11]. Compare Figs. 4.5 (a) and (b) to Figs. 4.3 (a) and (b); this shows that when I increase the weighting of weak spectrum components (the black part in Figs. 4.3 (a) and (b)) to recover the degraded resolution as well as the distorted PSF shape, the strong spectrum component of the point object (the white part in Figs. 4.3 (a) and (b)) becomes relatively weak (the inner black part in Figs. 4.5 (a) and (b)) in the corrected image spectrum, including the corrected object spectrum and noise spectrum. This means the noise mixed in the weak spectrum component of the point object is relatively amplified. To satisfy the SNR request, I have to reduce the weighting of weak spectrum to suppress the amplified noise as Figs. 4.5 (e) and (f) show. However, this degrades the spatial resolution. On the other hand, the redundancy fixes the short board for 3D-ITF, thus supporting better trade-off between spatial resolution and noise artifacts after the Weiner filter. As Figs. 4.5 (i) and (j) show, the amplified noise in 3D-ITF is much less than that in TF and is mainly located around the cut-off frequency. Part of the amplified noise is automatically removed by the apodization filter.

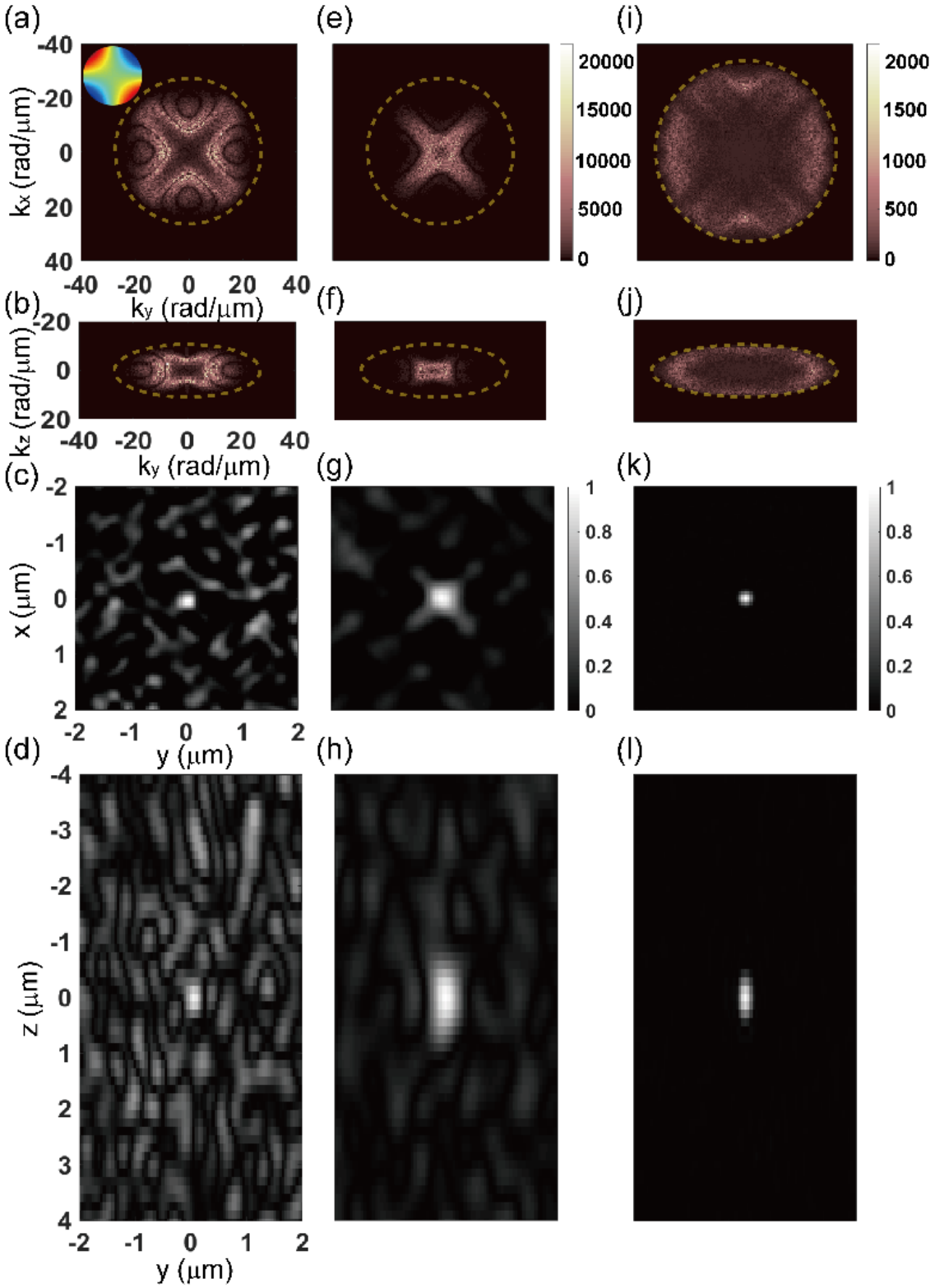

Fig. 4.5 Trade-off between amplified noise and spatial resolution with Zernike mode amplitude of 2 rad (RMS) and background fluorescence level of 1. (a) OTF_{xy} and (b) OTF_{zy} in TF when SNR=10, (c) corresponding PSF_{xy} and (d) PSF_{zy}; (e) OTF_{xy} and (f) OTF_{zy} in

TF when SNR=5, (g) corresponding PSF_{xy} and (h) PSF_{zy}; (i) OTF_{xy} and (j) OTF_{zy} in 3D-ITF when SNR=100, (k) corresponding PSF_{xy} and (l) PSF_{zy}. In (a, b, e, f, i, j) the dashed yellow circle shows the cut-off frequency of the apodization filter. The wavefront distortion is astigmatism (Zernike mode 5). The insert in (a) is the phase modulation of Zernike mode 5.

In addition to the resistance of spatial resolution, Fig. 4.6 shows that 3D-ITF also has the resistance of sectioning ability. The sectioning ability is determined by the axial frequency support along the k_z axis, which is called the missing cone in wide-field microscopy as Fig. 4.1 (b) shows. In 3D-ITF, it is the shifted TF OTF's axial frequency support along the k_z axis that offers the improved sectioning ability. When there is loss in the TF OTF spectrum, it can reduce the sectioning ability, which is the case in 3D-SIM. Again, the redundancy in 3D-ITF recovers the loss of frequency in TF OTF and maintains the frequency support along the k_z axis in 3D-ITF as Fig. 4.3 (f) shows, such that the sectioning ability in 3D-ITF is resistant to wavefront distortion and background fluorescence. Importantly, this sectioning ability in distorted 3D-ITF is maintained far beyond that with the TF focusing effect only. On the contrary, the TF image loses the sectioning ability due to a large amount of noise artifacts in deep and dense sample imaging.

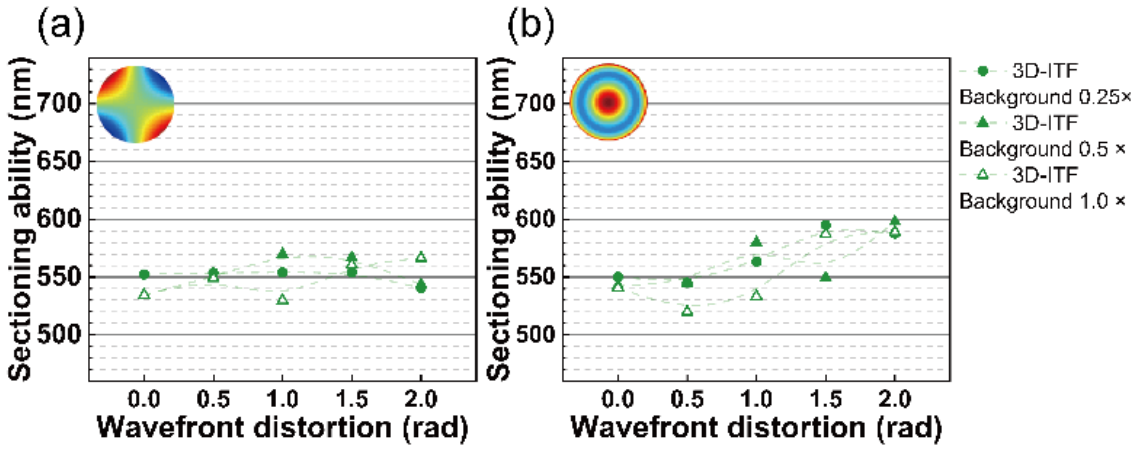

Fig. 4.6 Sectioning ability with wavefront distortion and background fluorescence in 3D-ITF (a) with astigmatism (Zernike mode 5) and (b) spherical aberration (Zernike mode 11). The insert shows the phase modulation of corresponding Zernike mode.

4.4 Summary

In conclusion, the optical distortions in illumination and emission were analyzed for 3D-ITF microscopy to derive its distorted PSF and OTF. With distorted optics, TF illumination locks the spatial modulation frequencies and other illumination distortions, mainly the offset shift of the interferometric pattern, retaining the image reconstruction algorithm valid. The potential illumination artifacts are removed by eliminating the 0^{th} order image in 3D-ITF. In the distorted 3D-ITF OTF spectrum, the dense sub-TF OTF copies support the redundancy. I show that although the TF OTF spectrum is narrowed and distorted due to optical distortions, the synthesized 3D-ITF OTF spectrum is less affected as the redundancy recovers the loss of spectrum. Thus, 3D-ITF microscopy shows resistance in spatial resolution and sectioning ability with fewer remaining noise artifacts in deep and dense sample imaging, while TF microscopy loses resolution and sectioning ability and retains more noise artifacts.

In practice, in order to increase the usage efficiency of laser power, adaptive optics (AO)[12–14] can be combined with 3D-ITF. Indeed, AO can correct wavefront distortion in both illumination and emission independently so as to correct the TF PSF; meanwhile it increases the SBR in the raw image. A combination of AO and 3D-ITF microscopy can significantly reduce the time to use AO. As the 3D-ITF image is robust, frequent AO correction during axial scanning is not necessary. This is the scheme to achieve deep and fast volumetric images with robust resolution around or beyond diffraction limitation. In addition, 3D-ITF microscopy can remove the remaining background in microscopy with AO, such as the surface emission in deep imaging, and further suppress the distorted PSF shape due to the remaining high order wavefront distortion. For the same reason, 3D-ITF microscopy can also benefit tissue-clearing techniques[15–17], which directly corrects the mismatch of the refractive index inside the sample.

The resistance of 3D-ITF microscopy prompts us to consider that SIM could be redesigned to increase the robustness of the image in addition to improving the spatial resolution. For example, introducing more modulation frequencies with lower fundamental modulation frequency by using more diffraction orders is a way to increase the redundancy so as to enhance the resistance to distorted optics. Recently, three-photon excitation

fluorescence 3D-ITF microscopy was invented to suppress background fluorescence[18]. This scheme is another way to increase the redundancy by increasing the order of modulation harmonics. Importantly, although the increased redundancy requires more raw images to reconstruct the image, the total acquisition time and nonlinear excitation energy are the same. The usage of TF can also be regarded as a method to increase the robustness of the illumination light, which locks the spatial modulation frequencies and increases the SBR of the raw images. These characteristics are all beyond the original motivation of SIM and TF; future work could include more advanced microscopy such as how to code in order to increase the efficiency of creating redundancy, and how to design in order to increase the ratio of the image SNR to the excitation energy.

References

1. Chaigneau, E., Wright, A. J., Poland, S. P., Girkin, J. M. & Silver, R. A. Impact of wavefront distortion and scattering on 2-photon microscopy in mammalian brain tissue. *Opt. Express* **19,** 22755 (2011).

2. Schwertner, M., Booth, M. J. & Wilson, T. Characterizing specimen induced aberrations for high NA adaptive optical microscopy. *Opt. Express* **12,** 6540 (2004).

3. Hell, S. W., Reiner, G., Cremer, C. & Stelzer, E. H. K. Aberrations in Confocal Fluorescence Microscopy Induced by Mistakes in Refractive Index. *J Microsc* **169,** 391–405 (1993).

4. Gibson, S. F. & Lanni, F. Experimental test of an analytical model of aberration in an oil-immersion objective lens used in three-dimensional light microscopy. *J. Opt. Soc. Am. A* **9,** 154 (1992).

5. Sun, B., Salter, P. S. & Booth, M. J. Effects of aberrations in spatiotemporal focusing of ultrashort laser pulses. *J. Opt. Soc. Am. A* **31,** 765 (2014).

6. Thomas, B., Wolstenholme, A., Chaudhari, S. N., Kipreos, E. T. & Kner, P. Enhanced resolution through thick tissue with structured illumination and adaptive optics. *J. Biomed. Opt.* **20,** 026006 (2015).

7. Arigovindan, M., Sedat, J. W. & Agard, D. A. Effect of depth dependent spherical aberrations in 3D structured illumination microscopy. *Opt. Express* **20,** 6527 (2012).

8. D ébarre, D., Botcherby, E. J., Booth, M. J. & Wilson, T. Adaptive optics for structured illumination microscopy. *Opt. Express* **16,** 9290 (2008).

9. Shroff, S. a., Fienup, J. R. & Williams, D. R. Phase-shift estimation in sinusoidally illuminated images for lateral superresolution. *J. Opt. Soc. Am. A* **26,** 413 (2009).

10. Wicker, K., Mandula, O., Best, G., Fiolka, R. & Heintzmann, R. Phase optimisation for structured illumination microscopy Abstract : **21,** 1642–1645

(2013).

11. A.R, Whitson, H.L, Walster, Soils and soil fertility, third ed., Webb, St. Paul MN, 1912, pp. 71-73.

12. Booth, M. J., Neil, M. A. A. & Wilson, T. Aberration correction for confocal imaging in refractive-index-mismatched media. *J. Microsc.* **192,** 90–98 (1998).

13. Ji, N. Adaptive optical fluorescence microscopy. *Nat. Methods* **14,** 374–380 (2017).

14. Li, Q. *et al.* Woofer–tweeter adaptive optical structured illumination microscopy. *Photonics Res.* **5,** 329 (2017).

15. Chung, K. *et al.* Structural and molecular interrogation of intact biological systems. *Nature* **497,** 332–337 (2013).

16. Hama, H. *et al.* ScaleS: an optical clearing palette for biological imaging. *Nat. Neurosci.* **18,** 1518–1529 (2015).

17. Ke, M.-T. *et al.* Super-Resolution Mapping of Neuronal Circuitry With an Index-Optimized Clearing Agent. *Cell Rep.* **14,** 2718–32 (2016).

18. Toda, K. *et al.* Interferometric temporal focusing microscopy using three-photon excitation fluorescence. *Biomed. Opt. Express* **9,** 1510 (2018).

Chapter 5

Conclusion and prospect

The purpose of this research is to make up the limitations in TF as well as to retain the wide-field optical sectioning feature of TF TPEF microscopy.

5.1 Summary of each chapters

In chapter 2, we achieve 2-D spatiotemporal coupling so as to improve the sectioning ability in the excitation path as well as retain the wide-field feature in TF. This technique use VIPA whose FSR is small enough to prevent out-of-focus interference up to several hundred micrometers. The sectioning width we achieved is 1.3 μm with the excitation wavelength of 803 nm and objective lens' NA of 1.2. At the same time, we verify that the out-of-focus TPE intensity follows a decay speed of $1/z^2$. This performance is comparable to a point scanning TPEF microscopy. By using this technique we demonstrate 3D volumetric imaging for 3D Brownie motion of 1-μm bead at an imaging speed of 50 volumes per second.

In chapter 3, we combined TF with SIM to remove background fluorescence in the emission path and to achieve super-resolution and super sectioning resolution via image processing. The lateral resolution we achieved in 3D-ITF is 1.4 times better than diffraction limited resolution. The sectioning ability we achieved in 3D-ITF is 0.65 μm, 2.6 times better than TF microcopy. By removing background fluoresce, we can achieve this performance at more than 200 μm imaging depth. Moreover, we verified the ability to remove background fluorescence in a scattering and dense biology phantom by comparing the image of TF and 3D-ITF microscopy.

In chapter 4, we investigate the performance of 3D-ITF in distorted optics. Considering wavefront distortion and background fluorescence in practical imaging in deep and dense sample imaging, we found that the both the spatial resolution and sectioning resolution of

3D-ITF is retained in distorted optics with wavefront distortion magnitude up to 2 rad (RMS) and a peak signal to background fluoresce intensity ratio up to 1. This origins from the lossless OTF spectrum in 3D-ITF due to redundancy. This lossless OTF gives better trade-off performance between the resolution and the noise artifacts in Wiener filter correction.

5.2 Conclusion

As a conclusion of the whole thesis, I solve following four issues in TF TPEF microscopy.

1. Worse sectioning ability in the excitation path compared to point scanning TPEF microscopy
2. Scattered emission fluorescence in the emission path as the background
3. Diffraction limited spatial resolution in TF image
4. Degraded of image quality with optical distortions

Through the experimental proof and numerical calculation, I conclude following four results.

1. 2D-TF can achieve the sectioning ability the same as a point scanning TPEF microscopy in the excitation path and retains the wide-field feature.
2. 3D-ITF can reduce the scattered emission fluorescence in the emission path by homodyne detection in the reconstructed image.
3. 3D-ITF increase the cut-off frequency in its OTF and thus break down the diffraction limitation in spatial resolution and sectioning resolution in the reconstructed image.
4. The reconstructed image in 3D-ITF is robust to optical distortions

5.3 Prospect

The general goal of TPEF microscopy including four aspects, to improve imaging depth, to improve imaging speed, to improve spatial resolution and to avoid sample damaging. And in general, there are two types of methods to realize these goals. First type is to improve by pure physical methods such as improvement from TF to 2D-TF. The second type is to utilize digital image processing algorithm such as SIM. This method do not

directly improve the imaging performance but do improve the performance of post-processed image. In my point of view, the first type of method is to increase the possible maximum imaging efficiency and the second type of method is to maximize the utilization under the physical limitation.

By this point of view, 2D-TF improves sectioning ability by a pure physical illumination improvement. But without combining any second type of method, 2D-TF is not fully utilized to maximize its potential. We could combine algorithm similar to 3D-SIM like the way how 3D-ITF improves sectioning ability and remove background florescence in post-processed image. Algorithm such as HiLo technique[1,2] is promising to remove background fluorescence by only two shots. Also HiLo can improve the sectioning ability of post-processed image compare to the image of 2D-TF only.

Then the next issue is which algorithm is the best method. This topic has not been discussed as there is no consensus on how to evaluate and compare different algorithms. In my point of view, the evaluation can focus on the post-processed SNR (noise mainly comes from the remained shot noise of background fluorescence) per excitation intensity per imaging size. And due to the photon damaging, mechanism and threshold value is different for different imaging target. This evaluation should be more specified to the same imaging target.

Recently compressed sensing[3] and optical image compression[4] techniques become powerful as the mathematical algorithm regarding sparsity has been developed successfully for many applications such as fast magnetic resonance imaging and fast STORM. These techniques can be also applied to TF TPEF microscopy for following advances. The first advances is also to remove background fluorescence. The same property compared to SIM or HiLo is that compressed sensing or optical image compression uses structured illumination. The difference is that compressed sensing or optical image compression use single pixel imaging method. They solve inverse problem to reconstruct the image. This difference results the second advances, as scattering emission contains the information of the imaging target, to solve inverse problem is to re-use this information to reconstruct the image. Therefore, it effectively re-assign the scattered emission photons back to its corrected pixels so as to increase the SNR and SBR compared to SIM or HiLo method. The third advance is that the emission wavefront, which is the main optics distortion in TF

is not a problem anymore by using single pixel imaging method. However, the imaging speed of compressed sensing currently has not been reported to be faster than SIM or HiLo technique for TF. Also this algorithm has not been reported to achieve super-resolution or super-sectioning ability. How to increase the imaging efficiency of compressed sensing and whether it can achieve super-resolution and super-sectioning ability is an interesting problem.

Recently, by successfully developing high power fiber laser above 1 μm, three-photon excitation fluorescence TF microscopy is developed[5]. Similar to 2D-TF, it enhances the sectioning ability by physical methods. However, due to TF only utilize 1D spatiotemporal coupling, the sectioning ability of this method is limited to a point-scanning microscopy. And the sectioning resolution is 1.6 μm by fully utilization of the objective lens with NA of 1.2, which is even worse than 2D-TF TPEF microscopy because they use longer excitation wavelength. If we use this fiber laser to build up 2D-TF microscopy, we can achieve three-photon excitation 2D-TF microscopy and the sectioning ability could be improved same as point scanning three photon excitation fluorescence microscopy.

For super-resolution imaging, although there are many methods, the core idea to improve the resolution depends on the nonlinearity or ON-OFF switching characteristic. Nonlinear optics in excitation such as TPE do not further enhance the resolution as the excitation wavelength is also increased. So the novel ON-OFF optical switching material is very important to further enhance the resolution below several ten nanometers. For damaging issue, usually there is not much freedom to reduce the threshold intensity of input laser for a given method. The effective method rely on adjusting the repetition rate to optimize the threshold or chemical modifications.

Anyway, all this prospect rely on our current knowledge. We expect break-through new technologies in optics, physics, mathematics, chemistry and biology to offer us more toolboxes in order to innovate 3D volumetric biomedical imaging methods. We hope our technology can benefit future biological discoveries and medical applications.

References

1. Lim, D., Ford, T. N., Chu, K. K. & Mertz, J. Optically sectioned in vivo imaging with speckle illumination HiLo microscopy. *J. Biomed. Opt.* **16,** 016014 (2011).
2. Ford, T. N., Lim, D. & Mertz, J. Fast optically sectioned fluorescence HiLo endomicroscopy. *J. Biomed. Opt.* **17,** 021105 (2012).
3. Stroud, J. R., Alemohammad, M., Shin, J. & Foster, M. A. Compressive temporal focusing microscopy (Conference Presentation). in *High-Speed Biomedical Imaging and Spectroscopy III: Toward Big Data Instrumentation and Management* 4 (SPIE, 2018).
4. Alemohammad, M., Stroud, J. R., Bosworth, B. T. & Foster, M. A. High-speed all-optical Haar wavelet transform for real-time image compression. *Opt. Express* **25,** 9802 (2017).
5. Toda, K. *et al.* Interferometric temporal focusing microscopy using three-photon excitation fluorescence. *Biomed. Opt. Express* **9,** 1510 (2018).

Acknowledgement

First of all, I would like to extend my sincere gratitude to my supervisor, Porf. Fumihiko Kannari. As the motto from Fukuzawa Yukichi Sensei, '独立自尊', Prof. Kannari provided me the maximum freedom to independently conduct the research with lab mates and at the same time he encouraged me to try the new idea. Moreover, Prof. Kannari showed me the maximum tolerance to accept failures and mistakes. Otherwise, I would not be able to finish my doctor course study.

Then I would like to express my thanks to Dr. Isobe in Riken. He taught me all the knowledge and skills which I want to learn. From him, I got the chance to know how to conduct the experiment to achieve perfect performance. Also he showed me the patience, passion and determination for research. He let me believe something I thought not possible is possible. The most important thing I learnt from him is the idea that research doesn't rely on lucky at all but on solid step by solid step.

I also would like to thank Mr. Yosuke Kojima, labmate in Kannari lab, who first had the idea to use VIPA to realize 2D-TF. Meanwhile I would like to thank Mr. Kazunori Seno and Dr. Kenya Suzuki in NTT research lab to teach me the knowledge of 2D spatial disperser. Following Mr. Kojima's suggestion and to use the knowledge I learnt in NTT research lab, I was able to build up the principle of 2D-TF.

Then I would like to thank Prof. Rainer Heintzmann. Although we only met half day, which would be one of the most beautiful half day in my life. He showed me all his research one by one himself. He explained me his experience in SIM research and introduced me the idea of photon re-assignment microscopy. This talk inspired me a lot.

I would also thank Dr. Hod Dana in Howard Hughes Medical Institute and Dr. Heejin Choi in Massachusetts Institute Technology for the very helpful discussions about TF and HiLo technology.

At last I would like to thank my parents. From their pure love, I got to understand the ultimate meaning of my life is to create happiness for my closest people rather than my personal success or personal feeling. All other things are nothing. This make me feel calm and be able to walk step by step.

For sure, the support from Dr. Midorikawa in Riken and my labmates is indispensable.

List of variables used

Variable name		Definition
c	=	speed of light
λ_c	=	central wavelength
$f_{Grating}$	=	focal length of collimating lens for grating
f_{Obj}	=	focal length of objective lens
$\gamma_{grating}$	=	$\frac{\lambda_c^2 grooves}{2\pi c \cos(\theta_{GratingIn})} \frac{f_{Grating}}{f_{Obj}}$, spatial chirping rate of grating, where $\theta_{GratingIn}$ is the incident angle of grating, *grooves* is the groove number of grating.
ω_c	=	$2\pi c/\lambda_c$, annular frequency of central wavelength
k	=	$2\pi/\lambda_c$, magnitude of wave vector of central wavelength
$\sqrt{2In2}\Omega$	=	FWHM spectral bandwidth in a Gaussian distribution
$\sqrt{2In2}\tau_0$	=	Fourier transform limited FWHM pulse width in a Gaussian distribution
θ_0	=	grating's spatial chirping angle in 1D-TF
w_0	=	transient beam waist in 1D-TF
Z_R	=	Raleigh length of transient beam in 1D-TF
Δx	=	beam waist of illumination light in 2D-TF, *x* direction
Δy	=	beam waist of illumination light in 2D-TF, *y* direction
γ_x	=	$\gamma_{grating}$, spatial chirping rate of grating in 2D-TF
f_{VIPA}	=	focal length of collimating lens for VIPA
γ_y	=	$\frac{n_r^2}{\omega_c \theta_{airinput}} \frac{f_{VIPA}}{f_{Obj}}$, spatial chirping rate of VIPA in 2D-TF, where n_r is the refractive index of VIPA, $\theta_{airinput}$ is the incident angle of VIPA.
$\sqrt{2In2}\Omega_s$	=	FWHM of angular diffraction profile of VIPA

ω_n	=	central frequency of each diffraction order in VIPA, ω_{n+1}-ω_n=2πFSR
θ_{mx}	=	beam divergence of monochromatic beam of 2D-TF, *x* direction
θ_{my}	=	beam divergence of monochromatic beam of 2D-TF, *y* direction
Z_{mx}	=	Raleigh length of monochromatic beam of 2D-TF, *x* direction
Z_{my}	=	Raleigh length of monochromatic beam of 2D-TF, *y* direction
$\sqrt{2In2}\Omega'$	=	out-of-focus local FWHM spectral bandwidth
$\sqrt{2In2}\Omega_s'$	=	out-of-focus local FWHM of angular diffraction profile of VIPA
θ_x	=	grating's spatial chirping angle in 2D-TF, *x* direction
θ_y	=	VIPA's spatial chirping angle in 2D-TF, y direction
v_x	=	transient beam scanning speed in 2D-TF, *x* direction
v_y	=	averaged transient beam scanning speed in 2D-TF, *y* direction
w_x	=	transient beam waist in 2D-TF, *x* direction
w_y	=	transient beam waist in 2D-TF, y direction
z_{Rx}	=	effective Raleigh length in 2D-TF, *x* direction
z_{Ry}	=	effective Raleigh length in 2D-TF, *y* direction
$\sqrt{2In2}\tau'$	=	out-of-focus FWHM pulse width in 2D-TF
$\sqrt{2In2}\tau_s'$	=	out-of-focus FWHM train pulse width in 2D-TF
$\mathbf{k_0}$	=	wave vector of central wavelength
p	=	fundamental lateral spatial modulation frequency in 3D-ITF
q	=	fundamental axial spatial modulation frequency in 3D-ITF
θ	=	diffraction angle of spatial-chirped beam in 3D-ITF

List of abbreviations used

1D	One-Dimensional
2D	Two-Dimensional
3D	Three-Dimensional
CCD	Charge-Coupled Device
CMOS	Complementary Metal–Oxide–Semiconductor
PSF	Point Spread Function
FWHM	Full-Width at Half-Maximum
OTF	Optical Transfer Function
TPEF	Two-Photon Excitation Fluorescence
TMX	Time-Multiplexing
SLM	Structured Illumination Microscopy
TF	Temporal Focusing
SSTF	Simultaneous Spatial and Temporal Focusing
STF	Spatiotemporal Focusing
TPE	Two-Photon Excitation
NA	Numerical Aperture
PALM	Photoactivated Localization Microscopy
STORM	Stochastic Optical Reconstruction Microscopy
SHG	Second Harmonic Generation
VIPA	Virtually Imaged Phased Array
ITF	Interferometric Temporal Focusing
DMD	Digital Micromirror Device
FSR	Free Spectral Range
FTL	Fourier Transform Limited
CPA	Chirped Pulse Amplification
sCMOS	scientific CMOS

RMS	Root Mean Square
SLM	Spatial Light Modulator
AO	Adaptive Optics
SNR	Signal-to-Noise Ratio
SBR	Signal-to-Background Ratio

List of Publications

Journal papers (related to this thesis)

1. Song, Q., Nakamura, A., Hirosawa, K., Isobe, K., Midorikawa, K. and Kannari F. Two-dimensional Spatiotemporal Focusing of Femtosecond Pulses and its Applications in Microscopy. *Review of Scientific Instruments*, **86**, 083701-1-9 (2015).
2. Isobe, K., Toda, K., Song, Q., Kannari, F., Kawano, H., Miyawaki, A. and Midorikawa, K. Temporal Focusing Microscopy Combined with Three-dimensional Structured Illumination. *Japanese Journal of Applied Physics*, **56**, 05250-1-6, (2017).
3. Song, Q., Isobe, K., Midorikawa, K. and Kannari, F. Resistance to Optical Distortions in Three-dimensional Interferometric Temporal Focusing Microscopy. *Optics Communications*, (2018). [In press].

Other journal papers

1. Isobe, K., Takeda, T., Mochizuki, K., Song, Q., Suda, A., Kannari, F., Kawano, H., Kumagai, A., Miyawaki, A. and Midorikawa, K. Enhancement of Lateral Resolution and Optical Sectioning Capability of Two-photon Fluorescence microscopy by Combining Temporal-focusing with Structured Illumination. *Biomedical Optics Express*, **4**, 2396–2410, (2013).
2. 宋 啓原，神成 文彦, 二次元時空間レンズを用いた多光子励起顕微鏡による高速深部観察. 光学, **44**, 23-29, (2015).
3. Song, Q., Nakamura A., Hirosawa, K., Isobe, K., Midorikawa K., and Kannari, F. Two-dimensional Spatiotemporal Focusing Microscopy. *Review of Laser Engineering*, **43**, 203-207 (2015).

Proceedings

1. Song, Q., Isobe, K., Hirosawa, H., Midorikawa, K. and Kannari, F. 2D Simultaneous

Spatial and Temporal Focusing Multiphoton Microscopy for Fast Volume Imaging with Improved Sectioning Ability. Multiphoton Microscopy in the Biomedical Sciences XV (SPIE 2015, San Francisco, California, United States), 93292N-1-5 (2015).

International conferences

1. Song, Q., Nakamura, A., Hirosawa K. and Kannari, F., "Two-dimensional Simultaneous Spatial and Temporal Focusing of Femtosecond Pulses", Novel Techniques in Microscopy, (OSA 2013, Hawaii, United States), p. NT3B.5, (2013).
2. Nakamura, A., Song, Q., Hirosawa, K. and Kannari, K., "2D Simultaneous Spatial and Temporal Focusing as a Fast-Scanning Two-Photon Excited Fluorescence Microscopy", Conference on Laser and Electro-Optics/Pacific Rim, (OSA 2013, Kyoto, Japan), p. WPJ_4, (2013).
3. Song, Q., Nakamura, A., Isouchi, A., Hirosawa, K., Isobe, K., Midorikawa K. and Kannari, F. "Using two-dimensional spatial and temporal focusing microscopy to increase the imaging depth and decrease the photobleaching probability", The 3rd Advanced Lasers and Photon Sources, (ALPS 2014, Yokohama, Japan), p. p-38, (2014).
4. Song, Q., Nakamura, A., Isouchi, A., Hirosawa, K., Isobe, K., Midorikawa K. and Kannari, F., "Using two-dimensional spatial and temporal focusing microscopy to increase the imaging depth and decrease the photobleaching probability", Biomedical Optics, (OSA 2014, Miami, United States), p. BT3A.25, (2014).
5. Isobe, K., Mochizuki, K., Song, Q., Suda, A., Kannari, F., Kawano, H., Kumagai, A., Miyawaki, A. and Midorikawa K., "Temporal focusing microscopy with structured illumination for super-resolution deep imaging", Conference on Laser and Electro-Optics, (OSA 2014, San Jose, United States), p. AW3L.5, (2014).
6. Song, Q., Isobe, K., Kannari, F., Kawano, H., Kumagai, A., Miyawaki, A. and Midorikawa, K., "Temporal Focusing Microscopy with 3D Structured Illumination for Enhanced Axial Resolution in Deep Imaging", 2015 European Conference on Lasers and Electro-Optics - European Quantum Electronics Conference, (OSA 2015, Munich, German), p. CL-4.6, (2015).
7. Song, Q., Isobe, K., Kannari, F., Kawano, H., Miyawaki, A. and Midorikawa, K.

"Multiphoton 3D Structured Illumination Microscopy for Enhanced Axial Resolution in Deep Imaging", Conference on Laser and Electro-Optics/Pacific Rim, (OSA 2015, Busan, South Korea), p. 27H2_2, (2015).

Domestic conferences

1. Song, Q., Isobe, K., Mochizuki, K., Suda, A., Kannari, F., Kawano, H., Kumagai, A., Miyawaki, A. and Midorikawa, K., "Enhancement of Lateral Resolution and Optical Sectioning Capability by Combining Temporal-focusing with Structured Illumination", The 34th Annual Meeting of Laser Society of Japan, (Laser Society of Japan, Kitakyushu, 2014), p. I220PV11.
2. Song, Q., Nakamura, A., Isouchi, A., Hirosawa, K., Isobe, K., Midorikawa, K. and Kannari, F., "Two-dimensional simultaneous spatial and temporal focusing for two-photon excited fluorescence microscopy", The 61st Spring Meeting of the Japan Society of Applied Physics, (Japan Society of Applied Physics, Kanagawa, 2014), p. 17p-E6-8.